

Utah State University

DigitalCommons@USU

All Graduate Theses and Dissertations

Graduate Studies

12-2012

In Situ Measurements of Electron-Beam-Induced Surface Voltage of Highly Resistive Materials

Joshua Hodges
Utah State University

Follow this and additional works at: <https://digitalcommons.usu.edu/etd>

 Part of the [Materials Chemistry Commons](#), [Physics Commons](#), and the [Polymer Chemistry Commons](#)

Recommended Citation

Hodges, Joshua, "In Situ Measurements of Electron-Beam-Induced Surface Voltage of Highly Resistive Materials" (2012). *All Graduate Theses and Dissertations*. 1416.

<https://digitalcommons.usu.edu/etd/1416>

This Thesis is brought to you for free and open access by the Graduate Studies at DigitalCommons@USU. It has been accepted for inclusion in All Graduate Theses and Dissertations by an authorized administrator of DigitalCommons@USU. For more information, please contact digitalcommons@usu.edu.



IN SITU MEASUREMENTS OF ELECTRON-BEAM-INDUCED SURFACE
VOLTAGE OF HIGHLY RESISTIVE MATERIALS

by

Joshua Hodges

A thesis submitted in partial fulfillment
of the requirements for the degree

of

MASTER OF SCIENCE

in

Physics

Approved:

Dr. JR Dennison
Major Professor

Dr. Shane Larson
Committee Member

Dr. Jan J. Sojka
Committee Member

Dr. Mark R. McLellan
Vice President for Research and
Dean of the School of Graduate Studies

UTAH STATE UNIVERSITY
Logan, Utah

2012

Copyright © Joshua Hodges 2012

All Rights Reserved

ABSTRACT

In Situ Measurements of Electron-Beam-Induced Surface Voltage
of Highly Resistive Materials

by

Joshua Hodges, Master of Science

Utah State University, 2012

Major Professor: Dr. JR Dennison
Department: Physics

This study presents the development, calibration, characterization, and use of new instrumentation for *in situ* measurements of electron-beam-induced surface voltage. The instrument capabilities allow for measurements of a full range of insulating materials that are of concern to NASA spacecraft charging experts. These measurements are made using moveable capacitive sensor electrodes that can be swept across the sample using an *in vacu* stepper motor. Testing has shown a voltage range of more than ± 30 kV with a low-voltage resolution of 0.2 V. The movable sensors allow for a radial measurement of surface voltage with spatial resolution as low as 1.5 mm. The instrumentation has response time of ~ 7 s from the time the beam is shut off until the probe is in position to take data and uses computer automation to stabilize the system and acquire data over the period of several days or longer.

Three types of measurements have been made on two prototypical polymeric spacecraft materials, Low-density Polyethylene (LDPE) and polyimide (KaptonTM HN), to illustrate the research capabilities of the new system. Surface voltage measurements were made periodically during the charging process using a pulsed electron beam and subsequently as the surface voltage discharged to a grounded substrate; these were used to obtain information about the material's

electron yields and bulk resistivity. The spatial profile of the voltage across the sample surface was also measured by sweeping the electrode across the surface. Subsequent measurements monitored the time evolution of the magnitude and spatial charge distribution as charge dispersed radially across the sample surface. The results of these measurements are present and compared to literature values validating the instrument's effectiveness.

(157 pages)

PUBLIC ABSTRACT

In Situ Measurements of Electron-Beam-Induced Surface Voltage
of Highly Resistive Materials

Joshua Hodges, Master of Science

Utah State University, 2012

Surface charging and subsequent electrostatic discharge due to interactions with the space environment is one of the primary concerns of spacecraft charging studies. Laboratory measurements of the evolution of surface voltages and dissipation currents under simulated space conditions are the primary method used to determine the response of key spacecraft materials to diverse incident fluxes. Increasing the database of information for the electronic properties of insulating materials can assist spacecraft designers in mitigating the harsh effects of the space environment.

The Utah State Materials Physics Group, with the funding of the NASA James Webb Space Telescope project and personnel support from the United States Air Force PALACE Acquire program, has developed new instrumentation capable of noncontact measurements of the electron-beam-induced surface voltage as a function of time and position for nonconductive spacecraft materials. This new instrumentation used in conjunction with the capabilities of an existing ultrahigh vacuum electron emission test chamber facilitates measurements of charge accumulation, bulk resistivity, effects of charge accumulation and depletion on yield measurements, electron-induced electrostatic breakdown potentials, radiation-induced conductivity effects, and the radial dispersion of surface voltage.

Modeling and understanding the complex relationships between the spacecraft and its surroundings are fundamentally based on detailed knowledge of how individual materials store and transport charge. The ability to better understand how these affect spacecraft materials will

help make the complex spacecraft are exploring the edges of the universe more stable, reliable, and economic.

ACKNOWLEDGMENTS

First and foremost, I would like to acknowledge Dr. JR Dennison. His ideas and drive to push for more and more made this instrument what it is. Without his support, knowledge, motivation, and patience, I would not be where I am today. His generosity and willingness to share his knowledge will leave a lasting impression. Secondly, I would like to thank Ryan Hoffmann and his family. Without their support, both professionally and personally, I would not have been able to get through this trying time. They are wonderful friends that I am lucky to have. I would also like to mention the members in my committee, Jan Sojka and Shane Larsen. Without your flexible schedules and understanding of the stresses I was under, I would not have been able to finish under my accelerated time frame. Thank you for your support.

All members of the USU Materials Physics Group, Alec Sim, Justin Dekany, Amberly Evans, Charlie Sim, Doug Ball, and Greg Wilson, thanks for putting up with me through my tenure. Your collaboration and efforts were very much appreciated. All of you are very talented and have very bright futures.

Special thanks to the United States Air Force PALACE Acquire program and the 558th Aging Aircraft Analysis Group. My bank account greatly appreciates the funding given to me throughout my graduate degree.

I would also like to acknowledge my family, including: my niece Zoe, who is a great stress reliever and always has a magical way to make me smile and forget about all the stresses in life; Jesse and Amy, who are always looking out for my best interest; and my mother and father, who are always there when I need them and who are interested in what I am doing regardless if they have an idea of what it is.

Joshua Hodges

CONTENTS

	Page
ABSTRACT.....	iii
PUBLIC ABSTRACT	v
ACKNOWLEDGMENTS	vii
LIST OF TABLES	xi
LIST OF FIGURES	xii
LIST OF SYMBOLS	xv
LIST OF ABBREVIATIONS	xviii
CHAPTER	
1. INTRODUCTION	1
1.1. Current Configuration of Chamber and Its Limitations	2
1.2. Overview of Thesis and Proposed Experiments	3
2. INSTRUMENTATION AND AUTOMATION	6
2.1. Theory of Operation.....	7
2.2. Electron Emission Chamber	8
2.2.1. Hemispherical Grid Retarding Field Analyzer	11
2.2.2. Sample Carousel	13
2.3. Probe Design.....	15
2.3.1. Electrical	18
2.3.1.1. Effective Resistance and Capacitance.....	18
2.3.1.2. Electrostatic Voltmeter Probe	22
2.3.1.3. Air Side Connection to Probe	25
2.3.2. Mechanical.....	27
2.3.2.1. Solid Model.....	27
2.3.2.2. Motor/Motion.....	29
2.3.3. Assembly.....	31
2.3.4. Extended Analysis Features	41

	ix
2.4. Automation	42
2.4.1. LABView™ Interface.....	42
2.4.2. Control Box.....	44
3. INSTRUMENTATION VALIDATION AND CHARACTERIZATION	49
3.1. <i>Ex Situ</i> Testing	51
3.2. Ground Drift.....	53
3.3. Linear Calibration	58
3.4. Voltage Drifts.....	62
3.5. Voltage Resolution.....	63
3.6. Radial Resolution.....	66
4. APPLICATIONS OF INSTRUMENT	70
4.1. Collection and Processing of Data	75
4.1.1. Methods of Collecting Data	75
4.1.2. Data Processing.....	77
4.2. Charge Accumulation and Electron-Induced Electrostatic Discharge.....	78
4.2.1. Basic Model and Assumptions.....	79
4.2.2. Models Including Emission	87
4.2.3. Models Including Dissipation	89
4.2.4. Surface Voltage Probe Charging and Discharge Models with Dissipation	95
4.2.5. Charge Decay Models.....	99
4.3. Fits to Charge Accumulation and Charge Dissipation Data	100
4.3.1. Charge Accumulation	101
4.3.2. Charge Diffusion.....	106
4.3.3. Fits to Electrostatic Discharge Observations	108
4.4. Fits to Radial Charge Diffusion Data.....	109
5. CONCLUSIONS AND FUTURE WORK	117
5.1. Conclusions.....	117
5.2. Future Work.....	123
5.2.1. Instrumentation Upgrades	123
5.2.2. Future Applications.....	127
5.2.2.1. Proposed Experiments with the Surface Voltage Probe.....	128
5.2.2.2. Proposed Experiments with the SVP and HGRFA	131

REFERENCES	x 134
------------------	----------

LIST OF TABLES

Table	Page
2.1. Legend of SVP components.....	6
2.2. Idealized sources of resistance and capacitance in the SVP system.	20
3.1. Definitions of values in the sample voltage equation.	50
4.1. Common material properties for tested materials.*	70
4.2. Fitting parameters for charging and discharging fits.	100
4.3. Timing scenarios of beam charging runs on Kapton HN™ accumulation.	104
4.4. Comparison of decay measurements for peak radial decay and voltage decay curves on Kapton HN™.....	110

LIST OF FIGURES

Figure	Page
1.1. Schematic representation for two different resistivity measurements.	2
2.1. Schematic of charge distribution for the EFTP assembly.	7
2.2. USU Materials Physics Group's electron emission chamber.	9
2.3. HGRFA with Attocube ANR50 UHV stepper motor.	12
2.4. Drawing of original HGRFA configuration prior to implementation of SVP.	13
2.5. Sample stage with cooling reservoir.	14
2.6. Relationship of resistivity and charge decay times for common spacecraft materials.	17
2.7. Electrical schematic of SVP showing all resistors and capacitors.	19
2.8. Monroe probe electrical schematic as adapted from Monroe Inc. (1994).	23
2.9. Dry air purge pump and desiccant filter.	24
2.10. Witness plate MHV connector assembly.	26
2.11. Air side of SVP.	27
2.12. View of the clearance of the inner grid and large sample.	28
2.13. View showing the sample blanked with the Au SEE standard and the Faraday cup.	29
2.14. Overall dimensions of SVP with center of gravity indicated.	29
2.15. Front panel of LABView™ VI control program.	30
2.16. Exploded view of SVP internal parts.	31
2.17. Isolating sapphire spheres (0.5mm diameter).	32
2.18. Photograph of the assembly of the SVP.	33
2.19. Exploded view of SVP motor assembly.	34
2.20. Photograph of Au SEE standard and Aquadag surface of the SVP.	34
2.21. Photographs of SVP motor and control wire routing: front and rear views.	35
2.22. Photograph of positioning using a template.	36

	xiii
2.23. Full-scale alignment template for LABView automatic positioning sequences.	37
2.24. Control box schematic.	45
2.25. Feedthrough cable layout.	46
2.26. Front and back panels of SVP control box.	47
2.27. Block diagram of SVP system.	48
3.1. Visual progression of <i>ex situ</i> testing.	49
3.2. Preliminary <i>ex situ</i> drift measurements, showing a large linear drift effect.	51
3.3. Hokey pokey effect.	52
3.4. Faraday cage to help reduce the noise of the <i>ex situ</i> tests.	53
3.5. Three calibration setups and their corresponding electrical diagram to measure different drifts of the system.	54
3.6. Long-term drift of a grounded witness plate detailing Monroe probe controller drift.	55
3.7. Long-term <i>ex situ</i> drift test shows extreme changes of slope in short time periods.	55
3.8. Graph of <i>in situ</i> measurements and exponential fits of the drift of the SVP over ground.	56
3.9. Uncertainty in the linear approximation to the drift of a grounded sample.	57
3.10. Large probe calibration curve data (uncorrected).	59
3.11. Repeated 10 voltage ramp runs of 1000 V sample voltage with corrections.	60
3.12. Three superimposed calibration curves of the large electrode.	61
3.13. Single small probe calibration curve $CF\ 14890 \pm 125\ V_{\text{sample}}/V_{\text{probe}}$	61
3.14. Sample voltage (blue) and ground (red) measurements drift approach an equilibrium value V_{drift0} (dashed line).	62
3.15. Repeated measurements of slope of voltage drift versus probe voltage for the large electrode with a linear fit.	63
3.16. Graph of relative error as a function of surface voltage.	67
3.17. Minimum radial resolution based on sample voltage.	68
3.18. Comparison of expected profile measurements (red) and data (blue).	69
4.1. Composite total yield curve of Kapton HN™.	71

	xiv
4.2. Experimental yield curve of LDPE.....	72
4.3. Penetration Range of Kapton HN™ (dashed) and LDPE (solid).....	73
4.4. Timing of a standard charge accumulation/dissipation run.	76
4.5. Basic slab geometry of charge transport for an incident electron beam.	80
4.6. Models of charge layer.....	82
4.7. Charging and discharge data of LDPE with fits to include emission and nonohmic conductivity.	101
4.8. Charging and discharge data for Kapton HN™ with fits to include emission and nonohmic conductivity.	102
4.9. Fits of charge accumulation data for Kapton HN™ plotted versus beam on time.	103
4.10. Fits of charge accumulation data for LDPE	104
4.11. Fits of charge accumulation data (Eq. 4.33) vs. elapsed time for Kapton HN™	105
4.12. Fit of charge decay data for Kapton HN™ with nonohmic conductivity (Eq. 4.35).	107
4.13. Fit of charge decay data for LDPE with nonohmic conductivity (Eq. 4.35).....	108
4.14. Charge accumulation and subsequent breakdown of an LDPE sample.	109
4.15. Decay of the peak voltage during radial profile measurements on LDPE (red) with nonohmic dissipation fit (black).....	110
4.16. Radial profile vs. position at several times during decay measurements of LDPE.	112
4.17. Estimated change in conductivity during radial profile measurements.	114
4.18. Radial profile of LDPE at several times.	116
5.1. Typical noise vs. speed of response for the Monroe mV probe (Monroe Inc., 1994).	125
5.2. Decay curve of Kapton HN™ shows the total yield does not approach unity.	130

LIST OF SYMBOLS

A	= area of electrode
c	= speed of light in a vacuum
C_{eff}	= effective capacitance
C_{FT}	= capacitance of the feedthrough to ground
C_{SG}	= capacitance of the sample to ground
C_E	= capacitance of the electrode to the SVP through medium
C_s	= capacitance of the electrode to the sample through medium
C_v	= capacitance of the witness plate to the EFP through medium
C_p	= capacitance of the electrode to witness plate connecting wire
CF	= sample voltage calibration factor
D	= sample thickness
E_1	= total electron yield at first crossover energy
E_2	= total electron yield at second crossover energy
E_{max}	= incident energy at maximum total yield
F	= electric field
h	= Planck's constant
J_{in}	= injected current
k_b	= Boltzmann constant
k_{ric}	= material dependant RIC fitting parameter
N_t	= total density of traps
n_t	= total density of carriers
Q_o	= total incident charge
q_e	= charge on an electron
R_{eff}	= effective resistance

R_{SG}	= resistance of the sample to ground
R_{FT}	= resistance of the feedthrough to ground
R_E	= resistance of the electrode to the SVP through medium
R_p	= resistance of the electrode to the SVP through sapphire spheres
R_s	= resistance of the electrode to the sample through medium
R_v	= resistance of the witness plate to the EFP through medium
R	= penetration depth
s	= capture cross section
T	= temperature
t_{on}	= time beam is on
t_{off}	= time beam is off
t_d	= time at the point the SVP was ungrounded
t_v	= time at the point the SVP was moved onto the sample
V_{sample}	= sample voltage
V_{probe}	= probe voltage
V_{offset}	= offset voltage of the probe to ground
V_{elec}	= electronics voltage
V_{esd}	= voltage of electrostatic static breakdown
V_s	= surface voltage
V_{elec_o}	= voltage of EFP controller drift
V_{drift_o}	= ground voltage drift slope
V_o	= initial surface voltage
β	= sample voltage drift slope
Δ_{RIC}	= material dependant RIC fitting parameter

ΔV_{sample}	= uncertainty in sample voltage
ΔV_{offset}	= uncertainty in voltage offset
ΔV_{probe}	= uncertainty in probe voltage
ΔV_{probe}	= uncertainty in probe voltage
$\Delta \frac{V_{\text{drift}}}{\tau}$	= uncertainty in linear voltage drift
ΔA	= change in electrode area
ϵ_r	= relative dielectric constant
ϵ_o	= permittivity of free space
ϵ_r	=relative dielectric constant
ρ_m	=material density
μ	= mobility
ν_t	= trapping rate
ν_r	= release rate
σ	= electrical conductivity
σ_{DC}	= dark current conductivity
σ_{max}	= maximum electron yield
τ_d	= time constant of ground drift rate
τ_v	= time constant of sample voltage drift slope

LIST OF ABBREVIATIONS

BSE	Backscatter Electrons
CF	Calibration Factor
DAQ	Data Acquisition
DDLm	Dual Dynamic Layer Model
EFP	Electrostatic Field Probe
EFTP	Electrostatic Field Transfer Probe
FWHM	Full Width at Half Maximum
HGRFA	Hemispherical Retarding Grid Field Analyzer
LDPE	Low-density Polyethylene
MPG	Materials Physics Group
PEEK	Polyetheretherketone
RIC	Radiation-induced Conductivity
RSR	Relative Speed of Response
SE	Secondary Electrons
SEE	Secondary Electron Emission
SVP	Surface Voltage Probe
UHV	Ultra-high Vacuum
USU	Utah State University

CHAPTER 1

INTRODUCTION

The space environment includes a dynamic mix of particle species, charged and neutral plasmas, electric and magnetic fields, radiation, and physical debris (Hastings and Garrett, 1996). The effects of spacecraft interaction with this environment can include a range of problems from damage to the craft's structure, degradation of the electronic components, to unwanted electrical behavior and, in extreme cases, loss of spacecraft (Leach and Alexander, 1995).

Spacecraft charging is a deceptively simple issue of being able to predict and control the effects within materials as the spacecraft interacts with the space environment. Modeling and understanding the complex relationships between the spacecraft and its surroundings is fundamentally based on a detailed knowledge of how individual materials store and transport charge. The ability to better understand how this charge will move through and across the sample becomes invaluable in understanding how the charge will build up. Increasing the versatility and reliability of spacecraft charging models and expanding the database of information for the electronic properties of insulating materials can assist spacecraft designers in accommodating and mitigating these harmful effects (Hastings and Garrett, 1996; Fredrickson *et al.*, 2001; Dennison *et al.*, 2003a).

The conductivity of the material is a key transport parameter in determining how deposited charge will distribute across the spacecraft, how rapidly charge imbalances will dissipate, and what equilibrium potential will be established under given environmental conditions (Fredrickson *et al.*, 2003; Dennison *et al.*, 2005). The low charge mobility of insulators causes charge to accumulate where deposited, preventing even redistribution of charge and creating inhomogeneous local electric fields and potentials across the material. Hence, it is critical for reliable spacecraft charging models to use appropriate values of conductivity for thin

film insulators to determine the correct charge distributions and charge storage decay times for the materials.

The bulk conductivity values of commonly used insulators have most often been found using standard ASTM prescribed methods (ASTM D 257-99), utilizing a parallel plate capacitor geometry and an applied voltage. Similar tests have been done under vacuum conditions and more realistic space environments (Brunson, 2010), but these methods, in some cases are not strictly applicable to situations encountered in spacecraft charging (Coelho *et al.*, 1989; Fredrickson *et al.*, 2003). Charge decay methods expose one side of the insulator in vacuum to sequences of incident charged particles, light or plasma, with a conductive electrode attached to the other side of the insulator. Data are obtained by capacitive coupling to measure both the resulting voltage on the open surface and emission of electrons from the exposed surface, as well, monitoring both conductive and displacement currents to the electrode (FIG. 1.1). This thesis work implements a method for measuring surface voltage decay in an existing electron emission chamber.

1.1. Current Configuration of Chamber and Its Limitations

The original configuration of the electron emission chamber, as detailed by Hoffmann (2010), was a state-of-the-art analysis system. The chamber in its entirety can do electron

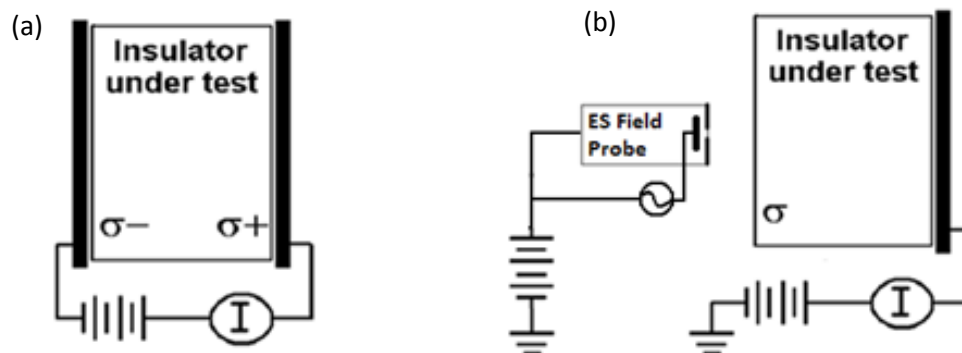


FIG. 1.1. Schematic representation for two different resistivity measurements. (a) classical method (b) charge storage method.

emission and transport measurements not reproducible anywhere else in the country. The chamber, however, lacked an effective way to measure surface voltage, let alone how voltage decays over time. The chamber can be used to infer surface voltage through three laborious methods based on the effects of the surface voltage on incident or emitted electron beams (mirror method, discontinuities in secondary and backscattered yields, and the spectral shift method) (Davies, 1996; Nickles, 2002; Hoffmann, 2010), but limitations to these indirect methods make physical interpretation difficult. Such interpretation could be determined far better with coincident direct measurements of surface voltage (Hoffmann, 2010).

The development of a surface voltage probe significantly improves our understanding of spacecraft charging by providing direct measurements of net charge accumulation and dissipation via surface voltage measurement that is predicted or inferred in a wide array of tests conducted by the Utah State University Materials Physics Group (USU MPG). In particular, the ability to compare the data for a given material from the multiple experimental test methods implemented at USU (Dennison *et al.*, 2009) will allow for the cross checking of physical parameters such as the density of states, trapping time, trap release rate, and segregation time (Monroe, 1987). The ability to confirm measurements and assumptions, such as those presented for the dual dynamic layer model (DDLDM) of the charge distribution in insulators irradiated with charged particle beams (Thomson, 2004; Hoffmann, 2010), for measuring amounts of electrostatic breakdown potentials from application of an electric field (Thomas *et al.*, 2006; Arnfield and Dennison, 2008) or induced by electron beam (Roth, 2009), or for bulk resistivity values with the charged storage method (Swaminathan, 2004) or for standard capacitive methods (Brunson, 2010), makes for a extremely versatile instrument.

1.2. Overview of Thesis and Proposed Experiments

This thesis presents all aspects of the development of the surface voltage probe. The thesis material is presented in the order the surface voltage probe (SVP) was built. Chapter 2

presents the basic design objectives of the SVP and the review of relevant information about the electron emission chamber in which the SVP has been installed. Discussion of the methods for construction, design and assembly of the SVP are detailed, as well as thorough information regarding the electronics and DAQ interface conclude the chapter. Chapter 3 provides information about the calibration and testing of the SVP that was completed to ensure the results from the probe were well understood, were quantifiable, and had physical meaning. Once measurements were made to characterize the drifts and the calibration factors, three types of measurements on Low-density Polyethylene (LDPE) and Kapton HN™ were used as a final confirmation of validity. Chapter 4 reports on how these materials charge up with bombardment of incident electrons, and how these charged samples decay over time. A third proposed measurement will show an extension of the capability of the probe by measuring surface resistivity as a function of radius.

The first of the proposed measurements will determine how charge builds up over time. A short ~10 s pulse of electrons will irradiate the sample; the surface voltage will be measured and the sample will be pulsed again. This will be repeated until the sample charges to equilibrium potential where electrons from the incident pulse are exactly matched by emitted electrons plus electron dissipation currents through the sample. The results will be modeled by a basic theoretical model for charge accumulation and dissipation. The charge accumulation information will also be used to validate predictions of the charge distribution made by the dual dynamic layer model (DDLDM) proposed by Cazaux (Cazaux, 1999) and used by Hoffmann (Hoffmann, 2010) to predict its influence on the dependence on charge of electron emission and details of features observed in electron yield and charge decay curves as a function of sample charging.

The second set of measurements will investigate how a charged sample will decay over time. Charge deposited in the previous test does not migrate much during the deposition process resulting in a very inhomogeneous charged distribution with most of the charge for the decay

experiments residing in a fairly narrow region from the surface to the range of the incident electrons. At the higher initial surface potentials the injected charge from the charge accumulation process drifts under its self-induced field to the back of the grounded insulator by means of a field-dependent transport process. As the charge distribution becomes more uniform throughout the sample and charge begins to dissipate through the grounded surface, the self-induced field lessens with a concomitant decrease in the rate of charge dissipation. The decay rate of the surface charge is determined by the bulk insulator conductivity, which has been studied extensively by researchers in the USU MPG (Swaminathan, 2004; Dennison, 2007).

The third and final measurement will investigate how charge flows across the surface of the sample. A small charge from a focused, well-characterized beam will inject a charge distribution at the center of the sample. Measurements of the spatial voltage distribution across the radius of the sample will be made and the evolution of voltage distribution over time will be monitored. This will provide a measure of how the charge dissipates over time, not only through the sample, but across the surface of the sample. Information about the surface resistivity and bulk resistivity, and perhaps about the radiation induced conductivity, can be extracted from these data.

The results from these measurements will not only act to validate the effectiveness of the new instrumentation, but will also lend credence to the data acquired from numerous USU MPG instruments and will allow the study of the consistency of results from the various methods. Chapter 5 summarizes the design of the new instrumentation, its use and effectiveness, and its application. It also provides suggestions for additional useful experiments for future investigators, as well as potential instrument upgrades.

CHAPTER 2

INSTRUMENTATION AND AUTOMATION

The purpose of this chapter is to outline the instrumentation detail. This chapter presents details of the electron emission chamber, the hemispherical grid retarding field analyzer (HGRFA), and the sample carousel, as well as intimate detail into the design, assembly and electrical and mechanical properties of the SVP. Table 2.1 represents a list of critical components and for reference to the figures in which the component appears.

TABLE 2.1. Legend of SVP components.

Chamber Element		Figures Element is Found In
HGRFA Hinged Mount	A	FIG. 2.3; FIG. 2.21
Sample Carousel/HGRFA Rotation Shaft	B	FIG. 2.5; FIG. 2.21
Attocube UHV Stepper Motor	C	FIG. 2.3; FIG. 2.21
Sample (10 mm Diameter)	E	FIG. 2.1; FIG. 2.3; FIG. 2.5; FIG. 2.4; FIG. 2.7; FIG. 2.12; FIG. 2.14
Sample Block	F	FIG. 2.3; FIG. 2.5; FIG. 2.4; FIG. 2.21
Cryogenic Reservoir	G	FIG. 2.3; FIG. 2.5
HGRFA Face Plate	H	FIG. 2.3; FIG. 2.4; FIG. 2.12; FIG. 2.21
HGRFA Hemispherical Shield	I	FIG. 2.3; FIG. 2.4; FIG. 2.21
HGRFA Collector	J	FIG. 2.4
HGRFA Bias Grid	K	FIG. 2.4
HGRFA Inner Grid	L	FIG. 2.4; FIG. 2.12
HGRFA Drift Tube	M	FIG. 2.4; FIG. 2.21
Motor Control Wires	N	FIG. 2.21; FIG. 2.22
SVP Wires	O	FIG. 2.21; FIG. 2.22
Surface Voltage Probe (SVP)	P	FIG. 2.12; FIG. 2.14; FIG. 2.13; FIG. 2.15; FIG. 2.18; FIG. 2.19; FIG. 2.21; FIG. 2.22
Au SEE Standard	Q	FIG. 2.12; FIG. 2.14; FIG. 2.19
Sample Current Lead	R	FIG. 2.1; FIG. 2.4; FIG. 2.7
SVP Faraday Cup	S	FIG. 2.14; FIG. 2.19
SVP Effective 7 mm Electrode	T	FIG. 2.1; FIG. 2.7; FIG. 2.13; FIG. 2.15; FIG. 2.18; FIG. 2.22
SVP Effective 3 mm Electrode	U	FIG. 2.1; FIG. 2.7; FIG. 2.13; FIG. 2.15; FIG. 2.18; FIG. 2.22
Motor Clamp	V	FIG. 2.21
EFTP Vacuum Feedthrough	W	FIG. 2.1; FIG. 2.7; FIG. 2.11
EFTP Witness Plate	X	FIG. 2.1; FIG. 2.7; FIG. 2.10; FIG. 2.11
Electrostatic Field Transfer Probe (EFTP)	Y	FIG. 2.1; FIG. 2.7; FIG. 2.8; FIG. 2.11
EFTP 6-axis Translator	Z	FIG. 2.11

2.1. Theory of Operation

The SVP utilizes Fredrickson's idea that a floating transfer probe can induce a surface voltage on an external witness plate that is proportional to the sample's surface voltage, and can be easily measured with standard noncontact electrostatic field probes outside of the vacuum chamber (Fredrickson, 1979). The USU MPG has developed an instrument that has a gold-plated neutral electrode, which can be moved in front of a charged sample. This internal electrode is electrically connected via a thin wire to a witness plate externally mounted to the vacuum chamber. As the internal electrode is moved in front of a charged sample, charge will polarize within the isolated plates and connecting wire (FIG. 2.1). The charge will migrate through the probe to the internal electrode and equalize the electric field caused by the sample charge by developing an equal magnitude charge density on the internal electrode. Assuming the probe is perfectly isolated from ground, an opposite polarity charge with equal magnitude net charge of the internal electrode, will develop on the external plate. Thus the charge density on the external witness plate is directly proportional to that of the internal plate and the sample. This external

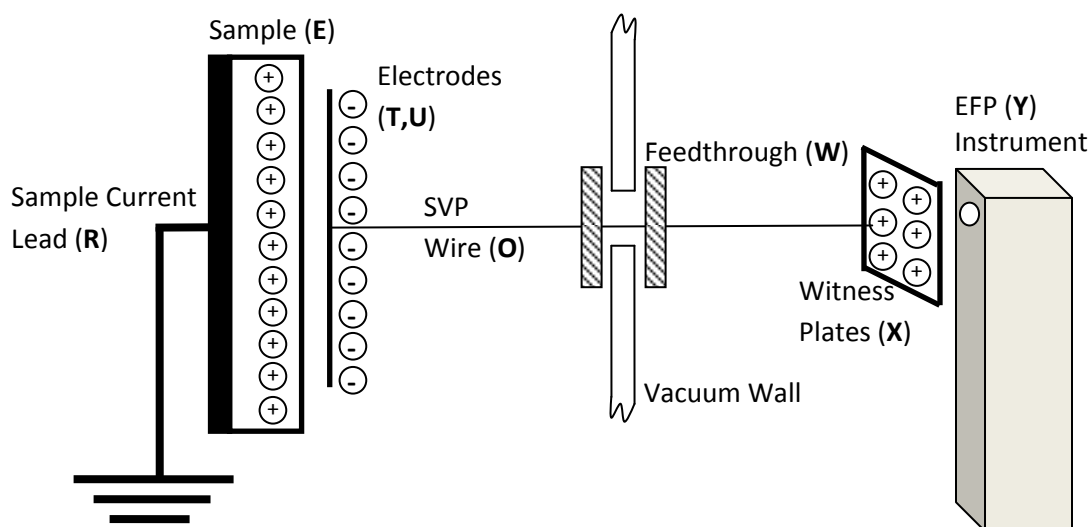


FIG. 2.1. Schematic of charge distribution for the EFTP assembly. Shown are the sample (left), charge transfer probe (center), and EFP (right).

witness plate is then measured with an electrostatic field transfer probe (EFTP) to determine the sample's charge density.

The USU MPG probe can measure a wide range of surface voltages, is very compact, and can be swept across the sample using an *in vacu* stepper motor to measure surface charge distributions on samples *in situ*. This design greatly extends groups measurement capabilities by allowing the surface voltage probe to fit within an existing HGRFA so surface voltages can be measured on samples tested using the extensive flux sources and emission detection capabilities of the electron emission vacuum test chamber.

2.2. Electron Emission Chamber

This section is a brief discussion of the electron emission chamber and its capabilities relevant to the SVP. It discusses the most relevant apparatus and equipment with detail given to the HGRFA and the sample carousel to which the SVP is added as an extension. A complete description of the DC-system and pulsed-system setups, along with additional insulator yield and charging data, can be found in theses and articles by Hoffmann, Nickles, and Thomson and Dennison (Nickles *et al.*, 2001; Thomson *et al.*, 2003; Thomson, 2004).

The primary apparatus used by the USU MPG to study electron emission from conductors and insulators is a versatile ultra-high vacuum (UHV) chamber (FIG. 2.2). This chamber has surface analysis and sample characterization capabilities that can simulate diverse space environments. These include controllable vacuum ($<10^{-10}$ to 10^{-3} Torr) and ambient neutral gas conditions, temperature ($150\text{ K} < T < 400\text{ K}$), and sources for a broad range of electron, ion and photon fluxes and energies. A variety of detectors are available for measurements of single or simultaneous electron-, ion-, and photon-induced emission (Nickles, 2002; Thomson *et al.*, 2003; Thomson, 2004), including a standard Faraday cup detector, hemispherical analyzer, cylindrical mirror analyzer, and time of flight micro-channel plate detector. Specifically, they allow for measurements of total emitted electron or ion yields, backscattered/secondary electron

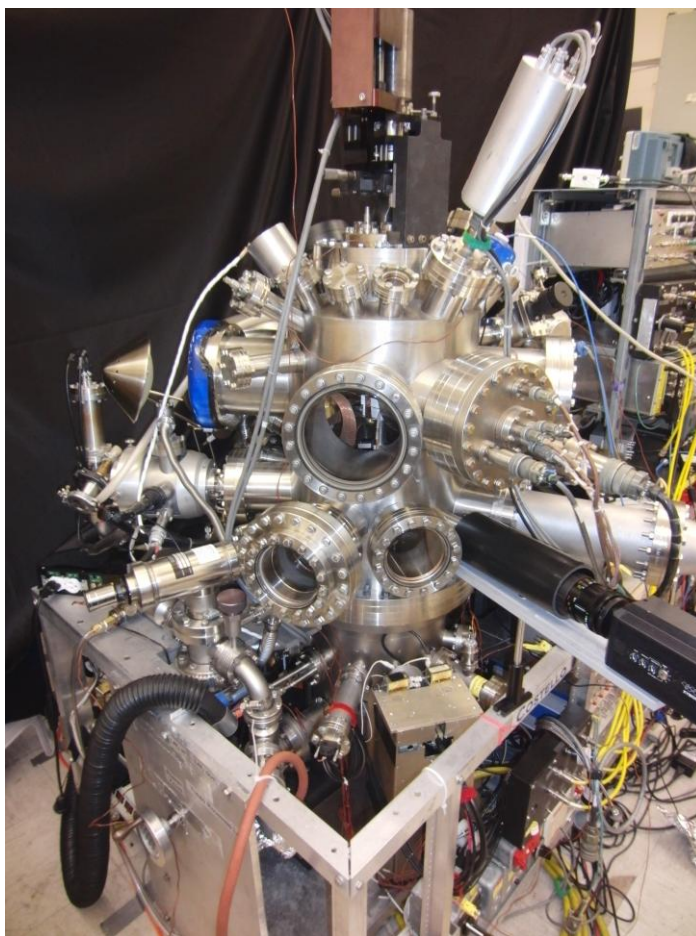


FIG. 2.2. USU Materials Physics Group's electron emission chamber.

yield, yield decay curves, charge decay curve, and emitted electron energy spectra (Dennison *et al.*, 2003b).

The chamber is equipped with two primary electron sources, a low-energy electron gun (Staib, Model NEK-050-SP) and a high-energy electron gun (Kimball, Model EGPS-21B). The low-energy electron gun is operated at incident electron energies of 20 eV to 5000 eV with a typical beam currents of 0.1-10 nA and a minimum beam spot diameter of <0.1 mm full width at half max. The high-energy electron gun is operated at incident electron energies of 3 keV to 30 keV with a typical beam current of 0.05 -1 μ A and a minimum beam spot diameter of <500 μ m. The two electron sources provide monoenergetic electron beams ($\Delta E/E < 2 \times 10^{-4}$) with electron

energy ranges from 20 eV to 25 keV and incident electron currents ranging from 0.05 nA to 20 nA, beam spot diameters ranging from 50 μm to $>10\text{ mm}$ (depending on beam energy), and pulsing capabilities ranging from 10 ns to continuous emission. Stable, uniform, well-characterized beam fluxes of $0.05\text{ nA}\cdot\text{cm}^{-2}$ to $150\text{ nA}\cdot\text{cm}^{-2}$ or higher are possible from these electron guns.

The chamber is also equipped with three ion guns with capabilities of producing monoenergetic sources of <0.1 to 5 keV for inert and reactive gases (Nickles, 2002; Thomson *et al.*, 2003; Thomson, 2004). One of the guns (PHI, Model I11-065) has rastering and pulsed deflection capabilities. The beam profiles of the ion can be characterized using a Faraday cup residing on the sample stage in conjunction with an automated LABView™ program, more discussion of this process can be found in Hoffmann (Hoffmann, 2010). The NIR-VIS-UV solar irradiance spectrum is simulated using a pair of pulsed, monochromatic lamp sources: (i) a tungsten/halogen lamp system with a *Suprasil* envelope produces focused ($\sim 0.5\text{ cm}$ diameter) radiation from 0.4 eV to 7.2 eV (200 nm to 2000 nm) and (ii) a deuterium RF powered continuum source with a MgF_2 window produces focused ($\sim 0.5\text{ cm}$ diameter) radiation from 3.1 eV to 11.1 eV (150 nm to 400 nm). Additional light sources include a helium resonance lamp (21.2 eV and 40.8 eV), broadband Hg discharge and W-filament sources, and a variety of quasi-monochromatic NIR/VIS/UVA LED sources, as well as a solar simulate source (Dennison *et al.*, 2003a).

For conducting samples, the electron guns are operated using a continuous, low-current beam of electrons, and DC currents are measured with custom ammeters sensitive to $\pm 50.00 \pm 0.01\text{ nA}$ (Nickles, 2002; Thomson, 2004; Hoffmann, 2010). In contrast, measurements of electron emission from insulating materials use a combination of methods to control the deposition and neutralization of charge (Nickles, 2002; Thomson, 2004; Hoffmann, 2010). Typically, charge deposition is minimized by using a low-current beam ($\sim 1\text{ nA}$ - 30 nA) focused

on a sample area of $\sim 7 \text{ mm}^2$ that is delivered in short pulses of $\sim 5 \text{ }\mu\text{sec}$. Each pulse contains $\sim 150 \text{ fC}$ or $\sim 10^5 \text{ electrons-mm}^{-2}$. The pulsed system uses custom detection electronics developed at USU with fast ($1 \text{ }\mu\text{s}$ to $2 \text{ }\mu\text{s}$ rise time) sensitive/low noise (10^7 V/A / 100 pA noise level) ammeters for determining insulator emission with minimal charging effects (Nickles, 2002; Thomson *et al.*, 2003; Thomson, 2004). Charge dissipation techniques include a custom low energy ($\sim 1 \text{ eV}$ - 10 eV) electron flood gun for direct neutralization of positively charged surfaces between incident pulses (Nickles, 2002; Thomson *et al.*, 2003; Thomson, 2004). A variety of visible and UV light sources are used for neutralization of negatively charged surfaces through the photoelectric effect. Increasing the sample temperature up to $100 \text{ }^\circ\text{C}$ has also been used for dissipation of buried charge by thermally increasing the sample conductivity. Often, samples will be heated to $\sim 50 \text{ }^\circ\text{C}$ overnight to increase conductivity and dissipate charge after a day of electron emission measurements. Both DC, pulsed measurements, and data retrieval are fully computer automated, using GPIB interfacing and a data acquisition (DAQ) card (National Instruments, Model BNC2110) under LABViewTM control.

2.2.1. Hemispherical Grid Retarding Field Analyzer

The primary detector for USU MPG emission studies is a custom hemispherical grid retarding field analyzer (HGRFA) (FIG. 2.3). Full detail of the instrument can be found in Hoffmann, Thomson and Nickles (Nickles *et al.*, 2001; Nickles, 2002; Thomson *et al.*, 2003; Thomson, 2004; Hoffmann, 2010). The HGRFA system provides emitted-electron energy discrimination between backscattered electrons (energies $>50 \text{ eV}$) and secondary electrons (energies $<50 \text{ eV}$). By ramping the grid (refer to labels **K** and **L**) bias, energy spectra of the emitted electrons can also be measured using this detector. The HGRFA features an aperture and drift tube (**M**) for incident electron/ion admission and a fully encasing hemispherical collector (**J**) for full capture of emitted electrons, that is particularly well suited and calibrated for absolute yield measurements (Chang *et al.*, 1998; Nickles, 2002; Thomson, 2004). The hemispherical grid

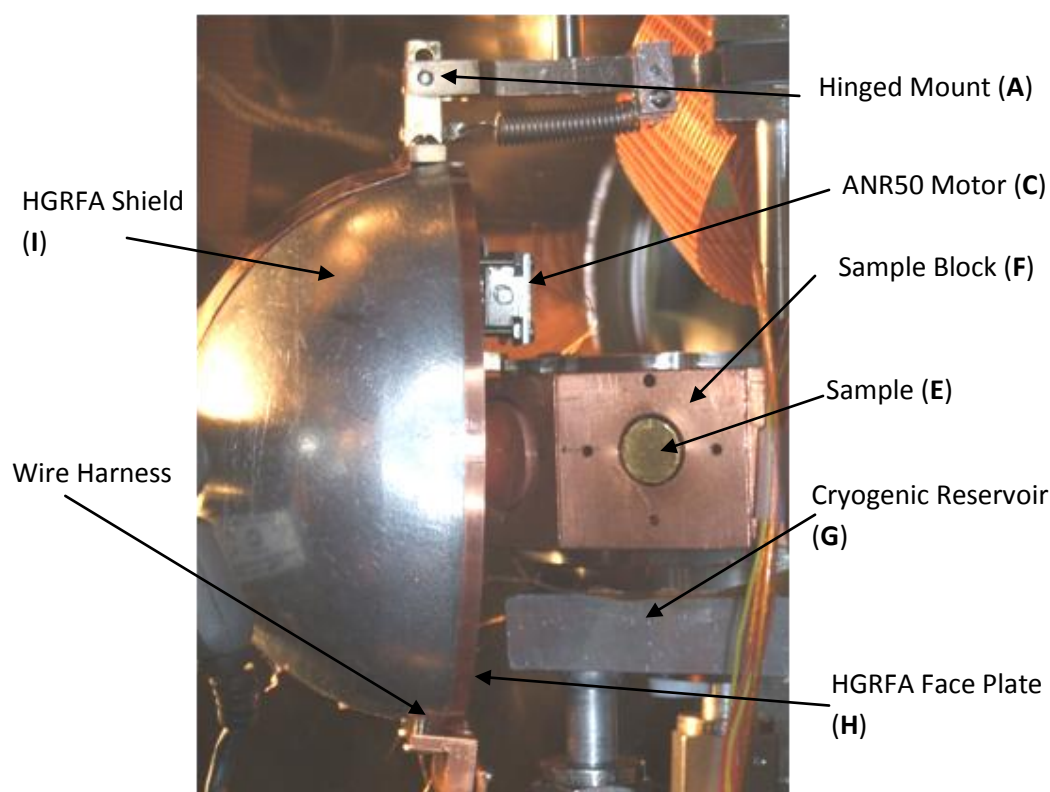


FIG. 2.3. HGRFA with Attocube ANR50 UHV stepper motor.

detection system has been carefully calibrated (both through calculation and measurement) to account for detector losses, allowing yield accuracies of better than 2% for conductor yields and better than 5% for insulator yields (Nickles, 2002; Dennison *et al.*, 2004). The HGRFA can be independently positioned in front of any sample on the sample stage (FIG. 2.3 and FIG. 2.4). A low-energy flood gun and a variety of visible and UV LED light sources are mounted on the HGFRA housing at near-normal incidence to provide neutralization of surface charging between pulses. A collimating lens mounted on the HRFA and attached to a fiber optic cable and vacuum feedthrough allows external light sources to be used or a photospectrometer to analyze emitted light from the sample. The flood gun (N) also acts as a low-energy (~ 1 eV to 100 eV), focused electron source.

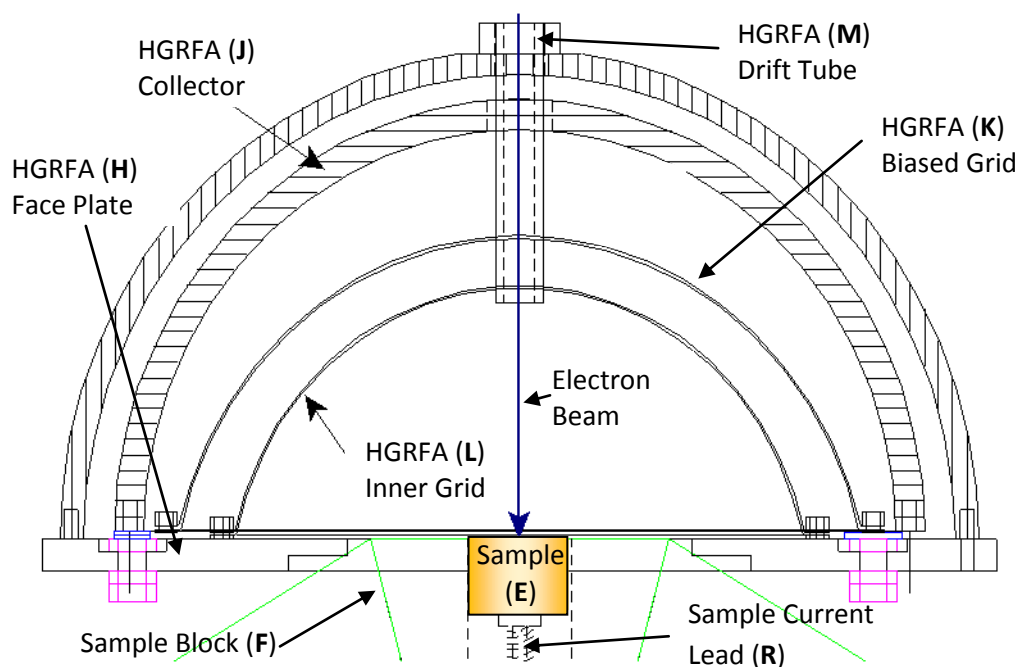


FIG. 2.4. Drawing of original HGRFA configuration prior to implementation of SVP.

The HGRFA face plate (**H**) was modified and used as a mounting plate for the SVP motor. The original configuration of the face plate (FIG. 2.5) allowed for measurements of current to be made from the face plate, as well as separately measuring the inner grid biased grid and the collector, to account for all electrons in the system. With the addition of the SVP to the system, the flipper needs to be isolated from the face plate so the currents of both the SVP and the face plate can be measured to separately account for total electrons in the system. Isolation of the flipper is discussed in more detail in Section 2.3.3.

2.2.2. Sample Carousel

Samples (**E**) are mounted on 10.0 mm diameter OFHC Cu cylinders, usually using a Cu tape with conductive UHV-compatible adhesive routinely used for scanning electron microscope studies (3M, Type 1182 tape). The Cu cylinders are mounted in sample blocks (**F**) on the sample carousel, using ceramic pins to provide electrical isolation. Electrical connection to the sample is

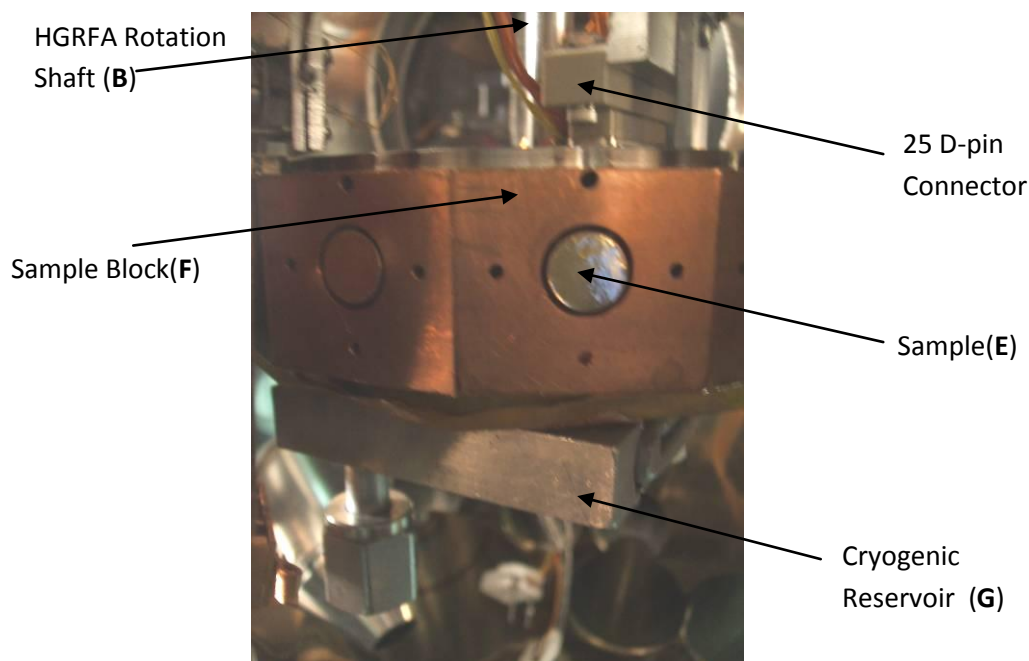


FIG. 2.5. Sample stage with cooling reservoir.

made via a spring-loaded pin (**R**) from the rear, allowing the current to the sample to be monitored. The sample carousel is a right dodecagon that has eleven sample blocks, which can be rotated in front of the various flux sources (FIG. 2.3 and FIG. 2.4). Typically, one sample block contains a photodiode, another contains a Faraday cup, and a third has a Au sample as an electron emission standard. The stage has been designed so it can be easily removed from the chamber. One module in the carousel is sacrificed to make way for a slot, from the center to the edge that allows the sample stage to slip away from the circular base on which it rests. The center region of the sample stage is hollow to allow for the various wires from the back side of each module to be accumulated and passed through the top plate via a 25-pin, UHV-compatible, D-type subminiature connector (Insulator Seals Part # 0981901). The 25-pin connector allows for quick removal of the sample stage and clean, hassle free, wiring of all samples. A 25-lead Kapton coated ribbon cable connects the internal D-pin connector to a UHV feedthrough (MDC Vacuum Part #D25-450-ISI 913208).

The samples can be thermally controlled from -150 °C to 100 °C. Heating of the samples is achieved via a resistive heating element (Omega CSS-01115/120V) that are controlled (Omega CN9000A PID controller) to within ± 1 °C. The samples are cooled with a liquid nitrogen cooling reservoir (FIG. 2.4); the cooling reservoir allows for samples to achieve temperatures of -150 °C within four hours of cooling. The temperature of the samples is controlled via an Omega temperature controller (Omega Part #CNi16D33-EI) connected to a liquid nitrogen solenoid. This system is capable of holding the temperature of the sample within ± 5 °C of the set temperature.

The samples are positioned mechanically via a grooved plate that locates the HGRFA face plate with remarkable accuracy of ± 0.5 mm from the sample. *Ex situ* tests have shown there is no degradation in the calibration factors for changes in probe to sample distances < 5 mm.

2.3. Probe Design

When designing an experiment, the physical parameters of the measurements being made drive the design of the apparatus. Experimental properties, such as range, resolution, response speed, and stability, must be considered. For this experiment, the constraints on these parameters are based on the electrical properties of the materials to be measured. These materials range from conductors such as gold, all the way to highly resistive materials such as Kapton HN™ and LDPE.

The range of voltages that could be seen in typical operation of the SVP can be as low as 1 V to higher than 10 kV. These values are based on breakdown potentials for common materials measured in the electron emission chamber. The low end of this result can occur in common spacecraft semiconductor coatings like germanium or silicon with bandgaps in the 1 eV range (Lide, 1993), or dielectric coatings like anodizing and irradiating layers or oxide layers (Thomson, 2001; Dennison *et al.*, 2004). These layers typically have breakdown potentials ranging from 1 V to 100 V, with electrostatic field strengths of 10^7 V/m to 10^8 V/m and typical thicknesses ranging from 10^{-6} m to 10^{-5} m. Past instrumentation similar to the SVP have been able

to measure down to as low as 30 V, in essence missing important information on items that could be critical in spacecraft applications (Dennison *et al.*, 2006). A goal was set to measure breakdown potentials lower than 10 V, accounting for the breakdown potential of the thin semiconductor coatings. Typical spacecraft bulk insulators, such as standoffs, PC boards, and thermal blankets, have much higher breakdown potentials. Electrostatic breakdown measurements have shown breakdown on thin 30 μm insulating materials are typically 5 kV to 10 kV. This does not set a maximum range that might be encountered in studies of typical spacecraft materials, but sets a value the instrument should be reasonably expected to measure. The resolution of the instrument is set by the low end of the range requirement. A reasonable expectation of the resolution would be $\sim 10\%$ of the low-end range. Resolutions of 0.1 V to 1.0 V would be sufficient for the resolution of the SVP.

The probe's response rate and stability are two other critical elements that must be considered when designing the instrument. The response speed and stability of this instrument must be sufficient to match the material response time in measurements, such as the surface voltage decay on insulators. Figure 2.6 shows the relationship between decay time and resistivity. NASA technical document 4003 (NASA-STD-4003, 2003) sets $10^{12} \Omega\text{-cm}$ as the maximum acceptable resistivity that meets all bulk and surface charging concerns. This level is determined to have decay times < 1 s in typical insulators. Such decay times are less than the minimum times for orbital or environmental changes, due to such things as satellite rotation or coming in and out of eclipse. Spacecraft materials, such as warm ceramics (*e.g.* Al_2O_3 , SiO_2 or BK7 borosilicate glass), large bandgap semiconductors (*e.g.* SiC) (Dennison *et al.*, 2009), or doped insulators or conductors (*e.g.* carbon bearing polymeric composites) have resistivities in the range of $10^{12} \Omega\text{-cm}$ to $10^{14} \Omega\text{-cm}$ with corresponding decay times of 10^{-1} s to 10^2 s. A reasonable target response time for the probe would be 1 s to 10 s. In order to take data on something that decays this rapidly, the instrument needs to be able to quickly move over the sample and take data. A fast

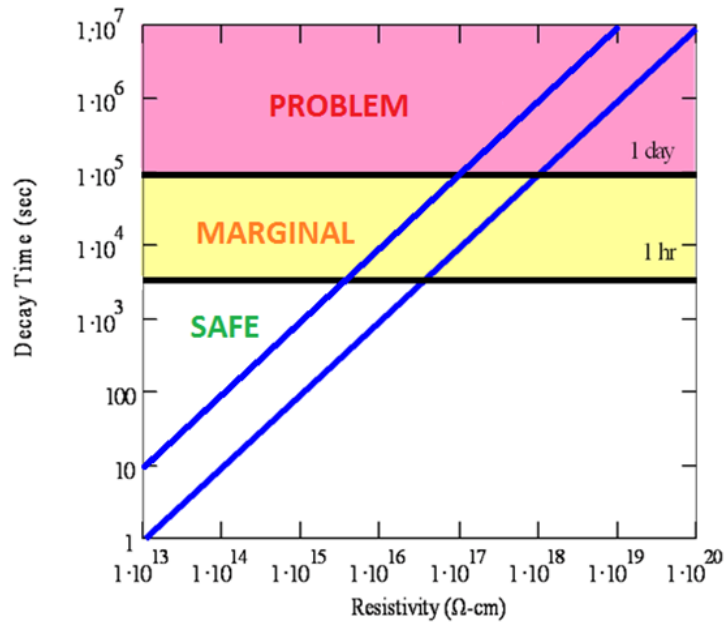


FIG. 2.6. Relationship of resistivity and charge decay times for common spacecraft materials. Blue lines represent the dielectric constants of ($\epsilon_r=1$ and $\epsilon_r=10$) typical spacecraft insulators.

moving motor, rapid electrostatic field probe response time, and short-term stability is needed to catch the decay of voltage over the course of 10 seconds.

Figure 2.6 shows for the most highly insulating materials, such as polymers (e.g. Kapton™ or Teflon) (Dennison *et al.*, 2009; Brunson, 2010) or low-temperature ceramics (e.g. Al_2O_3 , SiO_2 or BK7 borosilicate glass) (Dennison *et al.*, 2009), decay times can reach days, months, or even years. This end of the resistivity scale determines the necessary stability of the instrument. To measure decay times on the order of 10^6 to 10^7 seconds, or materials that have resistivities greater than 10^{20} Ω-cm, such as Teflon (PTFE) or Mylar (PET), the probe, instrumentation and vacuum chamber need to be stable over the course of several days while taking the surface voltage measurements. The ability to perform multiple experiments simultaneously, switching between samples and collecting data on several samples over several days, would be of benefit, but not necessary.

2.3.1. Electrical

This section discusses the electrical components of the probe, from selection of parts and materials to the building and installation of the probe. Thorough discussion of how each material affects the decay and drifts of the system is outlined in the upcoming section.

2.3.1.1. Effective Resistance and Capacitance

Key aspects of the construction of the probe include: materials, voltage sensor plates (**T** and **U**), connecting wires, and a feedthrough (**W**). In addition, the coupling of the voltage sensor plate (**T** and **U**) to the sample (**E**) and the witness plate(**X**) to the electrostatic field transfer probe (**Y**) need to be considered. In an ideal system, the probe would have an infinite resistance and zero capacitance coupling to ground, FIG. 2.1. This is, however, not true, as any system has some inherent resistance and capacitance. Figure 2.7 shows the known inherited resistance and capacitance leakage paths to ground during a standard measurement. This idealized circuit can be estimated to have one effective resistance and capacitance calculated from the system's leakage paths.

The value R_{eff} is important as it dictates how long valid measurements can be taken. In good experimental design, great care is taken in reducing the value of R_{eff} . The three largest sources of a resistance come from the leakage through air of the witness plate to the EFTP, the electrical isolation of the electrodes to the probe body through the sapphire spheres, and the vacuum feed through. TABLE 2.2 shows the resistance of each component of FIG. 2.7, the equations to find each resistance, and their calculated values. Depending on certain situations, some of the values of resistance can be ignored, for example during the conductor test, the resistance of the sample to ground, R_{SG} , is 0Ω , as there the sample is connected to ground. Throughout this thesis the equation for effective resistance is calculated by Eq (2.1); for each situation the values of R can take on different values or even be removed.

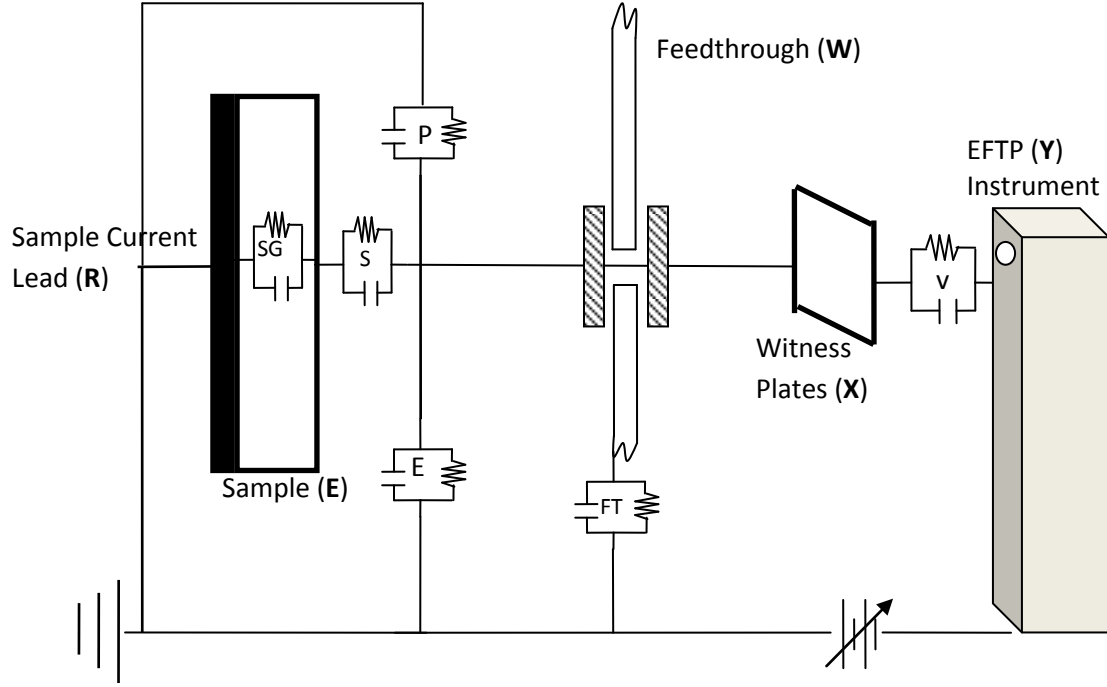


FIG. 2.7. Electrical schematic of SVP showing all resistors and capacitors. This system is an idealized system showing electrical leakage paths through the system. Some of these electrical connections are due to leakage paths through air, while others are leakage paths through the isolating elements of the system.

$$R_{eff} = \frac{1}{\frac{1}{R_s + R_{SG}} + \frac{1}{R_e} + \frac{1}{R_p} + \frac{1}{R_{FT}} + \frac{1}{R_v}}. \quad (2.1)$$

The value of C_{eff} is important as it dictates the range and resolution of the probe. In most cases, good experimental design will have C_{eff} be on the order of 10 pF and good experimental design keeps this as low as possible. Table 2.2 lists all the sources of capacitance that are accounted for from FIG. 2.7. The highest source of capacitance of the probe comes from the capacitance of the wire, and the capacitance of the feedthrough. This was easily seen in testing when calibration factors of $886 V_{sample}/V_{probe}$ (see Section 3.3 for detailed explanation of calibration factors) were measured when the connecting wire was 1.37 m long. When 0.3 m of wire was removed in final assembly, the calibration factor was increased by 18% to $1084 V_{sample}/V_{probe}$. For this modification, the calculated effective capacitance was decreased by 8% from 23.4 pF to 21.8 pF. The equation of effective capacitance used throughout this thesis is given in Eq. (2.2).

TABLE 2.2. Idealized sources of resistance and capacitance in the SVP system.

Sources of Resistance and Capacitance	Equation	Value
Feedthrough to Ground R_{FT} C_{FT} $\rho=8 \times 10^{15} \Omega\text{-cm}$ $r_o=6.35 \text{ mm}$ $r_i=1.2 \text{ mm}$ $l=40.5 \text{ mm}$	$R_{FT} = \frac{\rho l}{\pi(r_o + r_i)(r_o - r_i)}$ $C_{FT} = \frac{2\pi\epsilon_o\epsilon_r l}{\ln \frac{r_o}{r_i}}$	$R_{FT}=1.3 \times 10^{14} \Omega$ $C_{FT}=12 \text{ pF}$
Sample to Ground R_{SG} C_{SG} $\rho=4 \times 10^{17} \Omega\text{-cm}$ $d=0.025 \text{ mm}$ $r=5 \text{ mm}$	$R_{SG} = \frac{\rho d}{\pi r^2}$ $C_{SG} = \frac{\pi\epsilon_o\epsilon_r r^2}{d}$	$R_{SG}=3.2 \times 10^{15} \Omega$ $C_{SG}=83 \text{ pF}$
Electrode to SVP Body through Air R_E C_E $\rho_v=\infty \Omega\text{-cm}$ $\rho_a(\sim 50\% RH)$ $= \sim 4 \times 10^{15} \Omega\text{-cm}$ $r_e=3.5 \text{ mm}$ $d=0.4 \text{ mm}$	$R_E = \frac{\rho d}{\pi r_e^2}$ $C_E = \frac{\pi\epsilon_o\epsilon_r r^2}{d}$	$R_E=\infty \Omega$ vacuum $R_E=4.2 \times 10^{14} \Omega$ air $C_E=0.85 \text{ pF}$
Resistance of electrode to probe body through sapphire, and capacitance of wire R_p C_p $\rho=4 \times 10^{17} \Omega\text{-cm}$ $r_e=3.5 \text{ mm}$ $d=0.4 \text{ mm}$ $l=900 \text{ mm}$ $a=0.06 \text{ mm}$	$R_p = \frac{\rho d}{\pi r_e^2}$ $C_p = \frac{2\pi\epsilon_o\epsilon_r}{\ln \frac{l}{a}} \left(1 + \frac{1}{\ln \frac{l}{a}} (1 - \ln 2) \dots \right)$	$R_p=3.4 \times 10^{14} \Omega$ $C_p=6.3 \text{ pF}$
Electrodes to Sample R_s C_s $\rho_v=\infty \Omega\text{-cm}$ $\rho_a=4 \times 10^{15} \Omega\text{-cm}$ $r_e=3.5 \text{ mm}$ $d=2.4 \text{ mm}$	$R_s = \frac{\rho d}{\pi r_e^2}$ $C_s = \frac{\pi\epsilon_o\epsilon_r r_e^2}{d}$	$R_s=\infty \Omega$ vacuum $R_s=2.5 \times 10^{15} \Omega$ air $C_s=0.14 \text{ pF}$
Witness plate to EFP R_v C_v $\rho=4 \times 10^{15} \Omega\text{-cm}$ $r_w=5 \text{ mm}$ $d=0.125 \text{ mm}$	$R_v = \frac{\rho d}{\pi r_w^2}$ $C_v = \frac{\pi\epsilon_o\epsilon_r r_w^2}{d}$	$R_v=6.4 \times 10^{13} \Omega$ $C_v=5.6 \text{ pF}$

$$C_{eff} = C_e + C_p + \frac{I}{\frac{I}{C_S} + \frac{I}{C_{SG}}} + C_{FT} + C_v . \quad (2.2)$$

The wire chosen for this application was 36AWG (0.152 mm dia.) manganin wire (Lakeshore Part # WSL-32-100). The manganin wire has an alloy composition of 83% Cu, 13% Mn, 4% Ni and has an electrical resistivity of 48 $\mu\Omega$ -cm. The manganin alloy has a high diameter to strength ratio, allowing it to be manufactured in a much smaller gauge, reducing the system's capacitance, C_w . The ManganinTM wire has a thin polyvinyl formal (Formvar[®]) insulation. The Formvar[®] insulation has excellent mechanical properties, such as abrasion resistance and flexibility. The Formvar[®] insulation is 0.3 mm thick, which also helps in minimizing the capacitance of the system, making this wire the most suitable for the application at hand.

The two Au-plated electrodes are kinematically mounted and electrically isolated by sapphire spheres. Each plate is kinematically mounted to the probe body by six 0.5 mm in diameter spheres. The spheres are used because of sapphire's high-volume resistivity ($4 \times 10^{17} \Omega$ -cm @ 300 K). The resistance through six sapphire spheres in parallel is calculated in Table 2.2 to be 34 P Ω .

The feedthrough is a two-lead MHV ultrahigh vacuum feedthrough, from MDC. MHV is a good, readily available medium-power feedthrough with higher voltage ratings of 5 kV. It has a coaxial shielding for low-noise applications, and is shielded using a 40.5 mm aluminum oxide ceramic tube that is 12.7 mm outside diameter and 2.4 inside diameter. The resistance to ground of the feedthrough is approximated in Table 2.2 to be $1.3 \times 10^{14} \Omega$, and has a capacitance of 12.2 pF, making the feedthrough the largest contributor to the effective capacitance constant. The MHV feedthrough was chosen as the best fit, commercially available feedthrough, based from the experience of Dennison, Fredrickson *et al.* and Swaminathan (Dennison and Fredrickson, 2002; Fredrickson *et al.*, 2003; Swaminathan, 2004).

2.3.1.2. Electrostatic Voltmeter Probe

The setup allows for the usage of two different electrostatic field probes, the Trek Probe (Model 314A) and the Monroe Probe (Model #1015A). The Monroe Probe has a much smaller voltage range (-10 V to +10 V) giving better stability in this low-voltage range with a resolution of ± 1 mV. If the Monroe Probe gets a voltage overload, which occurs at magnitude of 10 V on the witness plate, the probe can be switched out to a Trek probe, the Trek probe has a much higher voltage range, ± 20000 V, however the voltage resolution is also much higher, 1 V, than the Monroe probe.

The electrostatic field probes have an electrode that looks at the witness plate through a small hole in the base of the probe assembly. A vane is mechanically vibrated in front of the electrode and the chopped AC signal induced on this electrode is proportional to the differential voltage between the witness plate and probe assembly. Its phase is dictated by the DC polarity (Monroe Inc., 1994). A reference voltage and this mechanically modulated signal, conditioned by the high input impedance preamplifier and signal amplifier, are fed to a phase sensitive detector whose output DC amplitude and polarity are determined by the amplitude and phase of the electrostatically induced signal relative to the reference signal. The output of this amplifier is used in a feedback loop to drive the probe to the same potential as that of the witness plate. The Monroe probe is driven to a DC voltage typically within 0.01% of the potential of the witness plate for a 1 mm probe to witness plate spacing. Simply by metering the output of the DC integrating amplifier, one has an accurate indication of the witness plate potential. (Monroe Inc., 1994) A schematic of the internal parts of the Monroe probe is provided for further explanation in FIG. 2.8.

This feedback principle and null seeking operation combine to make a remarkably stable and highly accurate instrument. The instrument's finite impedance is attributable only to ionic

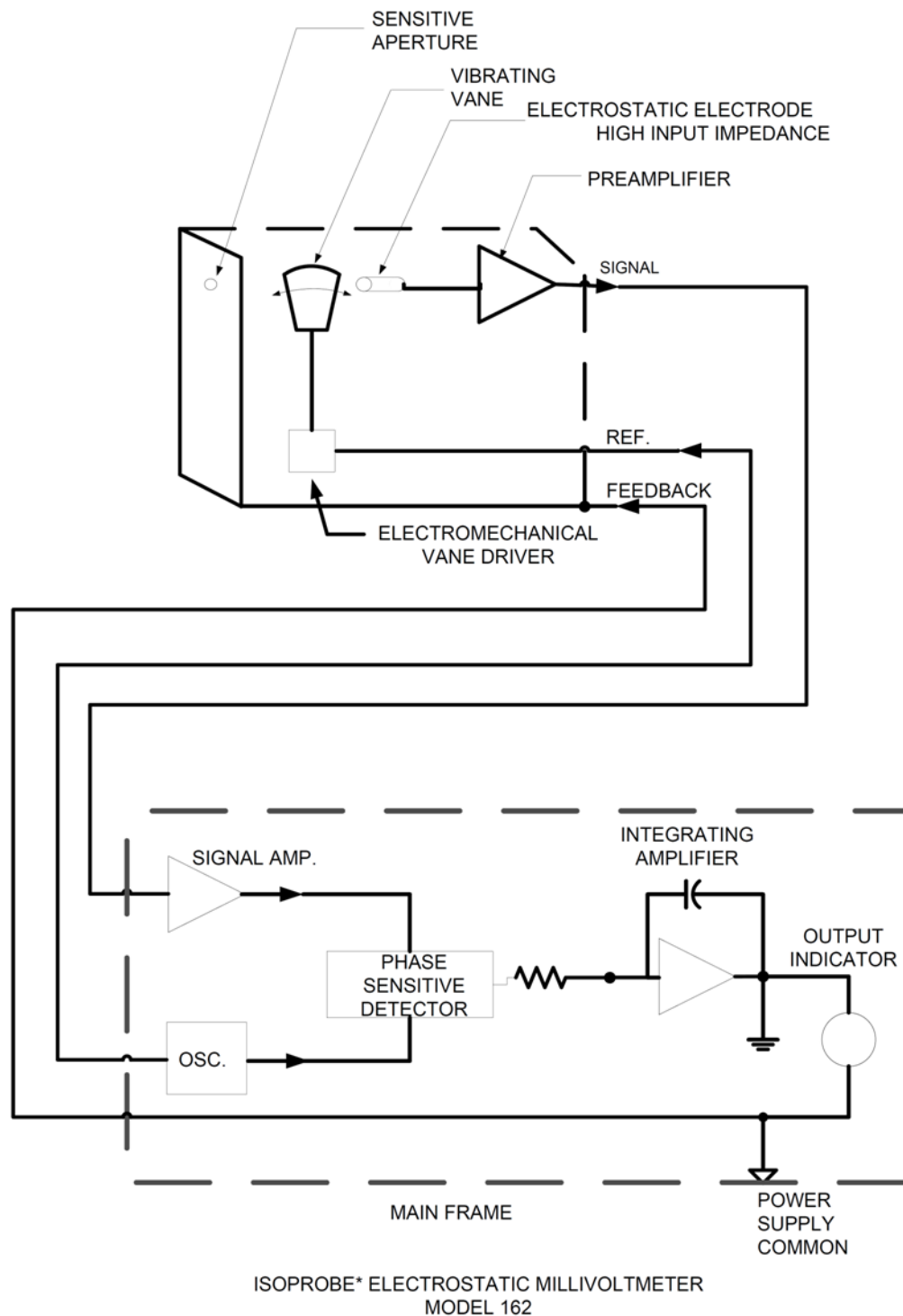


FIG. 2.8. Monroe probe electrical schematic as adapted from Monroe Inc. (1994).

conduction in the atmosphere. Therefore, the idea of placing the electrostatic field probe inside the vacuum chamber appears to be a good idea. However, the external mount used is preferred because the use of an electron beam to charge samples can cause erroneous effects on the probe itself and overload the probe. Discharging these effects on the probe inside the vacuum chamber becomes inherently difficult. For this reason, the probe is placed outside the vacuum chamber (Fredrickson *et al.*, 2003; Swaminathan, 2004).

Purified dry air is blown across the front of the mechanically modulated electrode. Figure 2.9 shows the Second Nature pump (Model Whisper 400) and desiccant filters to decrease the water in the air. The pump blows (~2 lit/min) of this dry air into an enclosed box creating a positive pressure of dry air around the EFP and witness plates; this reduces the ionic conduction between the probe and witness plate reducing R_e by 25% and therefore the drift of the probe electronics.

The noise related to the instrument is due to the high-impedance probe amplifier and is a function of the relative speed of response adjustment and probe-to-surface spacing. The Monroe probe has front panel switch for setting the relative speed of response (RSR). The switch selects



FIG. 2.9. Dry air purge pump and desiccant filter.

among a variety of integrating capacitors that sets the time constant of the capacitor to 0.005 s, 0.05 s, 0.5 s or 5 s. The longer integration time constants greatly reduce the electrical noise (Monroe Inc., 1994). A typical noise level for a 0.5 s RSR with a 0.8 mm probe-to-surface spacing is 3 mV RMS wide band. In the SVP measurements, the RSR is set to 0.05 s with a probe-surface-spacing of 0.5 mm, set with a 0.5 mm feeler gauge. A typical noise level for this setup is 1 mV. The Trek probe has a speed of response of $<200 \mu\text{s}$ and noise level of 1 V with a probe-to-surface spacing of 0.3 mm.

The output connector for the Monroe controller box is a front-mounted BNC connector. This output voltage is the measured voltage independent of the meter range or polarity switch. The output range is $\pm 10 \text{ V}$ and is short circuit proof. Output impedance is less than 0.1Ω ; therefore, for negligible loading error, the output load should be at least $10 \text{ k}\Omega$ (Monroe Inc, 1994). The Trek Probe buffered BNC output provides a 1000:1 reduction of the measured voltage and has $<20 \text{ mV}$ noise level. The maximum output of this voltage monitor is $\pm 29 \text{ V}$ (Trek Inc., 2000; Swaminathan, 2004).

2.3.1.3. Air Side Connection to Probe

Assuming the probe is assembled correctly, Table 3.1 shows the greatest source of a leakage path will occur in the vacuum feedthrough and the air side of probe. A two pin MHV feedthrough is used to make the link from the probe through the vacuum wall. The removable MHV connector was assembled with a copper rod (FIG. 2.10). OFHC Cu witness plates (12.75 mm diameter) were machined, polished with six micron polishing compound to a mirror finish, and then Au plated. This reduced edge effects by creating a more uniform electric field and eliminated stray surface voltage from oxidation or contamination. These witness plates were made significantly larger than the electrostatic field Monroe probe body (9.0 mm^2), minimizing any edge effects that would occur between the probe and the witness plate. However, smaller witness plates should lead to a smaller C_w , which leads to larger calibration factors and an

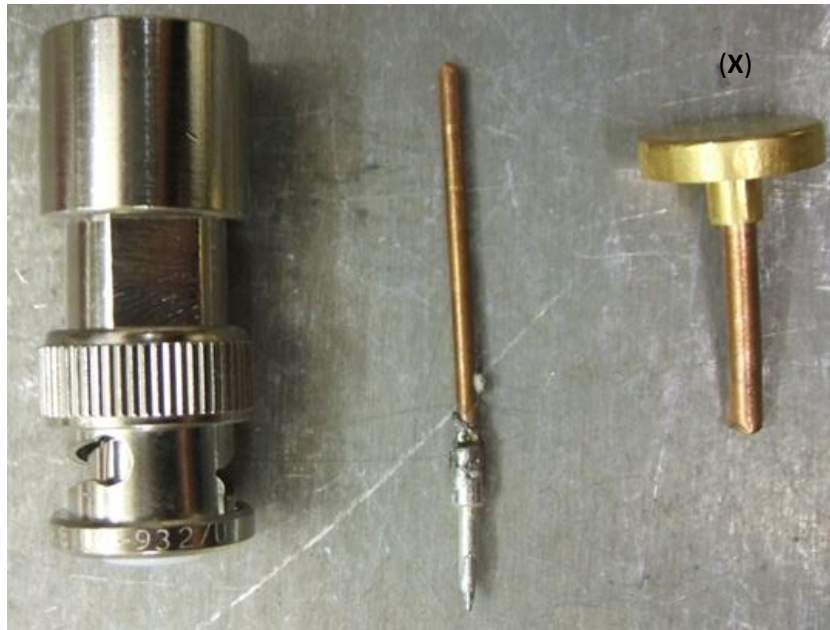


FIG. 2.10. Witness plate MHV connector assembly.

increase in range and resolution of the instrument. (A study should be conducted to determine the optimum witness plate size for future measurements.)

With two different electrodes in this instrument, the need for either two electrostatic field probes or the ability to easily move from one witness plate to the next is required. Since the probe was designed to take measurements using only one electrode at a time, the EFP holder was designed to be able to move between the two witness plates. The EFP is mounted on moveable mount with six degrees of freedom, precisely controlling the z and y dimensions, as well as coarse adjustments in the x direction, and rotations of the probe about the x, y and z axis (FIG. 2.11). The high-precision linear positoners are used to precisely locate the EFP to within 0.10 mm and parallel to the witness plate. The probe-to-surface spacing is set by a 0.5 mm feeler gauge and should be maintained as close as physically reasonable for best performance. Typical spacing ranges from 0.13 mm for mV resolution to 2.54 mm for measurements of volts (Monroe Inc., 1994).

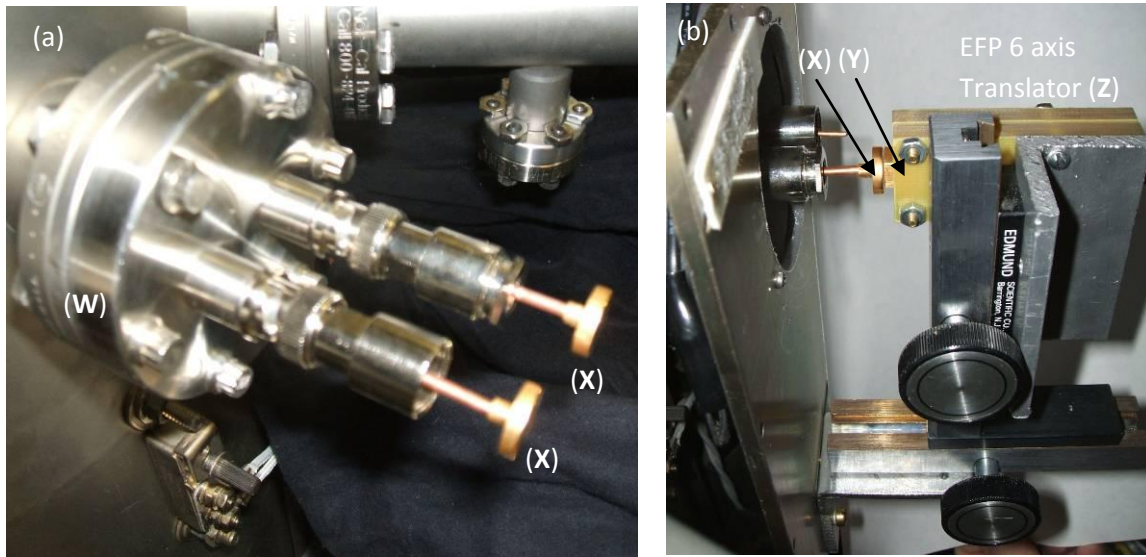


FIG. 2.11. Air side of SVP. (a) Witness plate feedthrough and connectors (b) six axis EFP positioner mounted parallel to a witness plate.

2.3.2. Mechanical

2.3.2.1. Solid Model

Before construction of the SVP assembly, a three-dimensional solid model of the detector motor was built using the Solid Edge V 20 graphics design program. The size and shape of the probe is driven by the dimensions of the HGRFA's 61.98 mm diameter inner grid. The SVP needs to be able to move completely off the large (19 mm) sample (FIG. 2.12) while staying confined inside the HGRFA's inner grid. The size of the SVP determines the maximum number of electrodes that could be installed (two), the diameter of those electrodes (4.7 mm and 9.65 mm) with active areas of 3 mm and 7 mm, respectively. From this point forward, the electrode with the 7 mm (**T**) active area will be referred to as the large electrode, and the electrode with the 3 mm (**U**) active area will be referred to as the small electrode. The large electrode covers nearly all the typical 10 mm sample. The small reduction in size eliminates edge effects on a completely charged sample. The large electrode has a radial resolution of 3 mm (see Section 3.6). The small electrode allows for a more detailed charge decay profile of the radial dispersion with a 1.5 mm

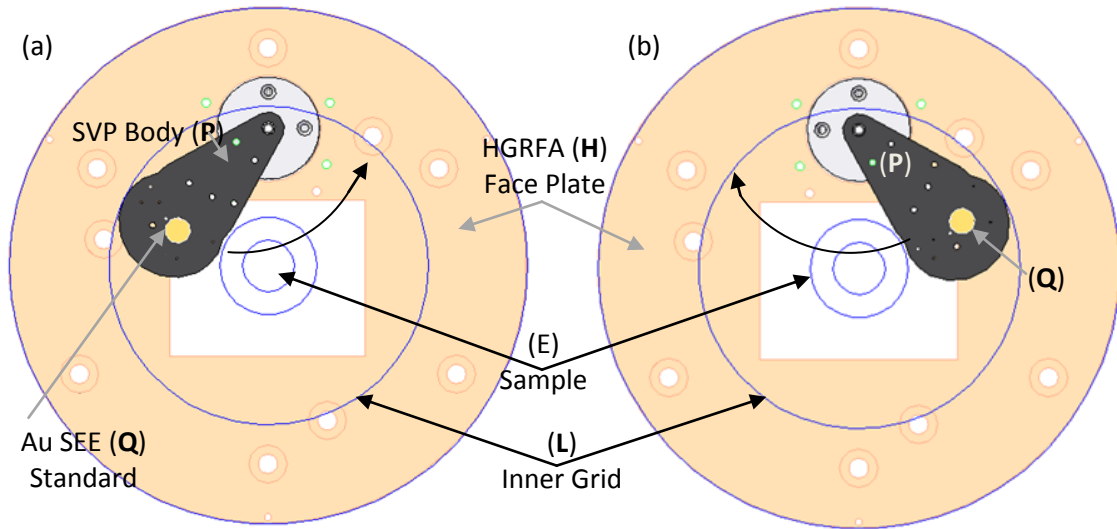


FIG. 2.12. View of the clearance of the inner grid and large sample. The view is looking toward the sample with the probe positioned at (a) hard right and (b) hard left.

radial resolution. The electrodes are made of a thin (0.51 mm) 316 stainless steel, which is Au plated to reduce edge effects and stray charge caused from contamination by oxide layers.

With the maximum number of electrodes determined, the shape of the body is then based on minimizing its size to decrease its effect of attracting secondary electrons during yield measurements, while remaining large enough to blank the sample while tuning the electron beam on a Faraday cup, or a Au sample located on the top of the probe (FIG. 2.13). Grooves cut on the side of the probe allowed for further clearance of the probe from the large sample (3.10 mm) (FIG. 2.12).

The final width of the probe is 21.26 mm at its widest point and has a maximum length of 33.05 mm. The center of gravity of the probe calculated from the solid modeling program is (20.32 mm) from the axis of rotation of the motor. The total mass of the probe calculated from the program is 3.51 gm (FIG. 2.14). The maximum torque due to gravitational force of the probe in its operational position is 0.1 N-cm. This is well under the 0.3 N-cm torque specification of the ANR50 motor (Attocube Systems, 2008).

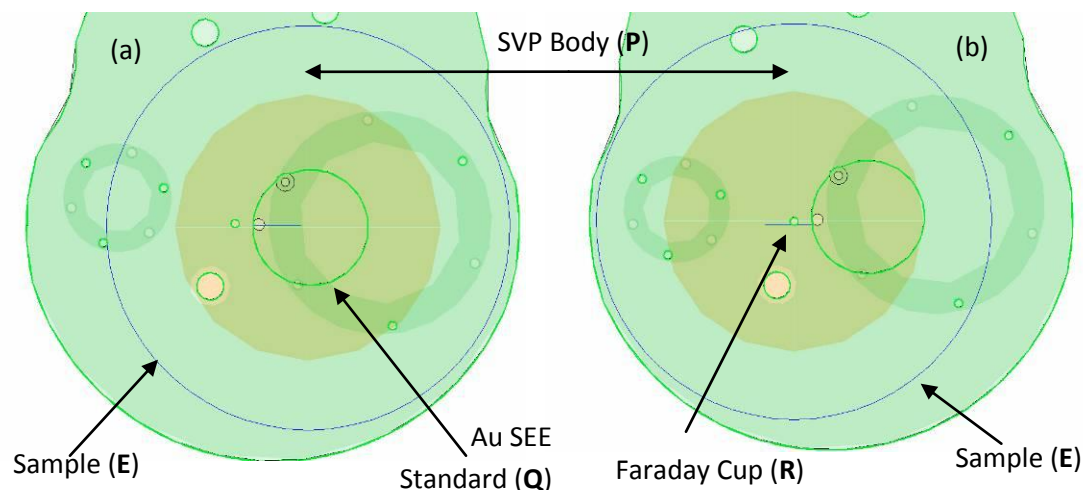


FIG. 2.13. View showing the sample blanked with the Au SEE standard and the Faraday cup. Image shows Au SEE standard (a) and the Faraday cup (b) centered on the large sample (blue circle) and the small 1 cm sample (orange disk) and the probe body fully blanking the sample.

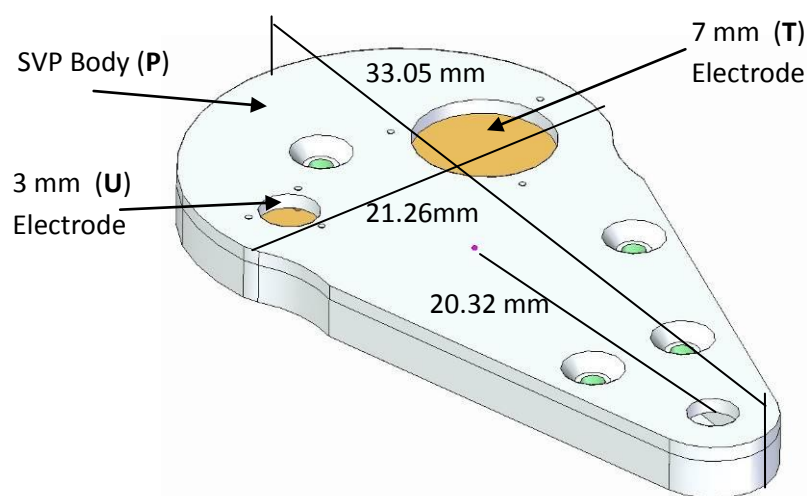


FIG. 2.14. Overall dimensions of SVP with center of gravity indicated.

2.3.2.2. Motor/Motion

The Attocube Systems' ultrahigh vacuum rotary motion stepper motor (Model ANR50UHV/LT/RES) was selected primarily based on its size. It stands 9.5 mm high and 20 mm in diameter. The small compact design makes it optimal for integration into the tight confines of the HGRFA detector assembly (See index I). The stepper motor runs on an impact drive mechanism (Attocube Systems, 2008). It utilizes static friction and impulsive forces caused by

the rapid displacement of a piezoelectric crystal. The motion mechanism of the motor consists of three parts: the main body, the piezoelectric crystal, and an inertial weight. When the piezoelectric crystal executes a slow reaction, the force due to static friction will exceed the inertial force so the main body keeps its position, when the piezoelectric crystal executes a fast expansion a strong inertial force is generated and the main body is displaced. Repeatedly combining these fast expansions and slow contractions will carry out a displacement in the motor. This kind of drive is called slip-stick drive.

The motor is controlled via a LABView™ virtual interface (VI) (FIG. 2.15), which drives the ANR150 motor controller. The motor controller allows for amplitude adjustments ranging from 0 V to 120 V and frequency adjustments ranging from 100 Hz to 4000 Hz to the piezoelectric crystal drive voltage signals. These input values allow for a range of step sizes of

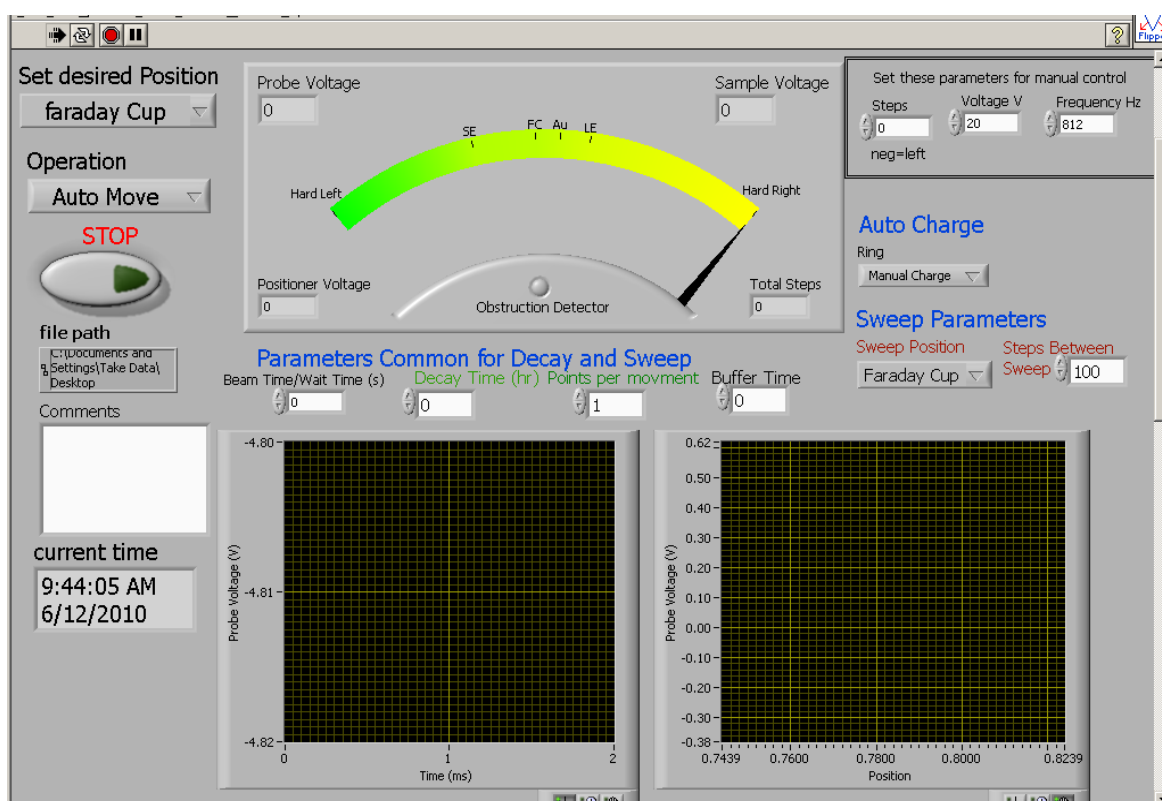


FIG. 2.15. Front panel of LABView™ VI control program.

0.005° to 0.070°. The resistive position encoder monitors the motor position to a 0.060° resolution driven by the 0.2 mV resolution of the DAQ card. This corresponds to a resolution of ± 0.02 mm on all elements of the SVP. The slip-stick drive allows for a continuous 360° endless rotation (315° position encoded), at 20 V amplitude, in both directions and has a speed of up to 10°/s during continuous usage. As configured, the stepper motor allows for a range of motion of 85°. Using a drive voltage of 20 V at 825 Hz the maximum angular speed of 10°/s is achieved (maximum linear speed of 4.6 mm/s in air.) It should be noted that continuous usage should not exceed 20 V amplitude due to overheating of the piezo-electric crystal (Attocube Systems, 2008). For rapid movements off the sample, unsticking of the motor, and long rest times, a higher amplitude up to 40 V is safe.

2.3.3. Assembly

With 15 internal probe parts, the complexity of assembling the SVP is challenging. Figure 2.16 shows an exploded view of the SVP with the main internal parts. Due to the

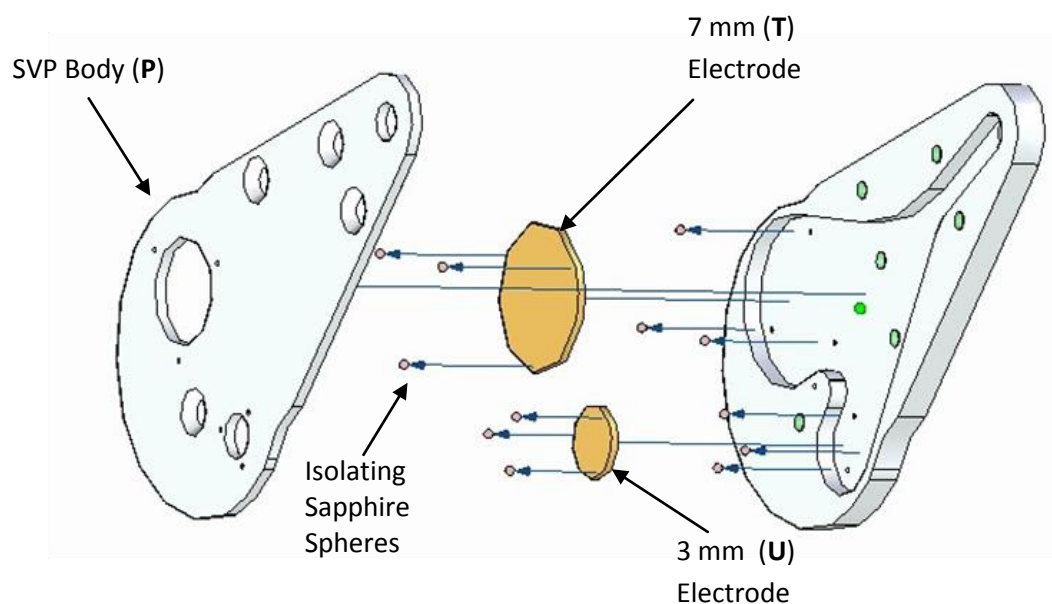


FIG. 2.16. Exploded view of SVP internal parts.

complexity of the assembly and the small size of the components, most notably the sapphire spheres (FIG. 2.17), it was necessary to use a removable adhesive to temporarily position component parts during the assembly process. To facilitate removal of these adhesives, they needed to be readily soluble in UHV solvents. Several different adhesives were tested to see ease of removal by an ultrasonic cleaner with methanol and warm water as solvents. The two adhesives that had the best solubility in the inert solvents were polyvinyl acetate to adhere the gold probes in place and a high-fructose corn syrup to locate the 0.5 mm sapphire spheres. The six sapphire spheres were adhered to the base of the probe and six were adhered to the cover. Once the sapphire spheres were set, a small amount of polyvinyl acetate was used to tack the electrodes in place (FIG. 2.18). Immediately after the second electrode was put in place, the cover was aligned and clamped.

The SVP assembly was initially checked with a multimeter for continuity between all parts to insure there was no continuity up to $2\text{ G}\Omega$ over all isolated elements. The SVP assembly was immediately placed in warm water and methanol solutions and then ultrasonically vibrated for 12 hours. Continuity between all parts and resistivity of each component was measured again to insure that good connections were made through the probes wires. The resistance was checked



FIG. 2.17. Isolating sapphire spheres (0.5mm diameter). Sapphire sphere shown in Roosevelt's ear for scale.

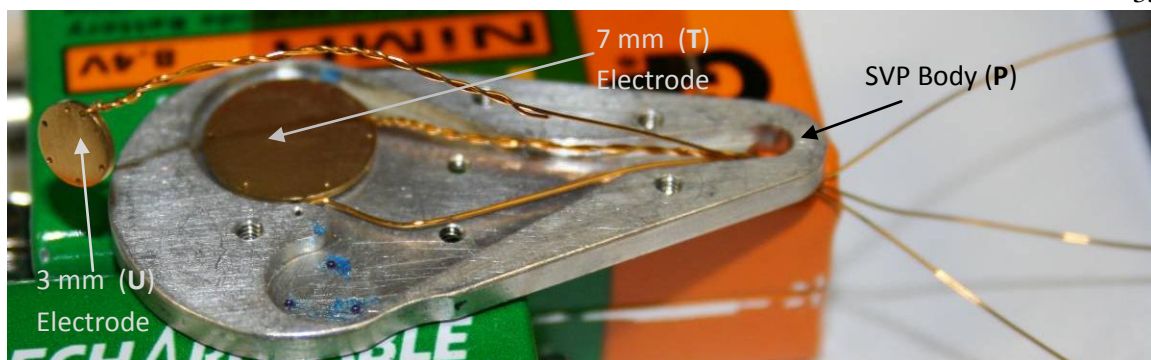


FIG. 2.18. Photograph of the assembly of the SVP. The large electrode is held in place with polyvinyl acetate and the small probe is ready for its kinematic placement via sapphire spheres.

between all parts again to ensure infinite resistance with a electrometer (Kiethly, Model 616), which can measure resistivities up to $2.0 \text{ T}\Omega$, to check that continuity between the parts did not exist.

When incorporating this new instrumentation into the HGRFA, careful thought must be given as to how the probe will alter the effectiveness of the old instrumentation. The HGRFA measures total electrons, therefore electrons may hit the probe during traditional yield measurements must be counted. This requires that the probe be isolated from the HGRFA face plate. Figure 2.19 shows an exploded view of the motor assembly, and the isolation elements. This is accomplished by a thin 0.127 mm sheet of Kapton tape between the probe and the motor mount plate. Two 0-80 polyetheretherketone (PEEK) UHV compatible highly insulating screws attach the probe to the mount plate electrically isolating the mount plate from the probe. In order to reduce the number of secondary electrons produced by backscatter electrons hitting the probe, it is covered with a 0.16 mm thick carbon conductive sheet (Ted Pella Inc. Product # 16085-1) that has a thin layer of Aquadag (Ladd Research Model # 60785) applied to the top layer (FIG. 2.19 and FIG. 2.20). This reduces the number of secondary electrons that are produced from backscatter electrons hitting the probe as the maximum secondary yield of microcrystalline

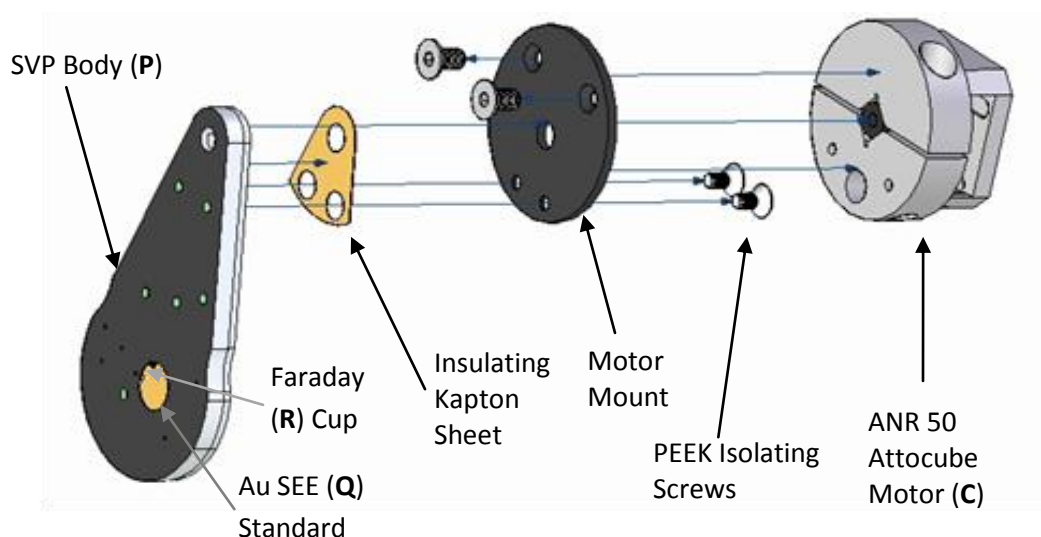


FIG. 2.19. Exploded view of SVP motor assembly. The isolation elements consist of 0.127 mm Kapton HN™ tape, and two countersink 0-80 PEEK screws that mount the SVP to the motor mount. The motor mount attaches to the motor with two stainless steel M2 flat head screws.

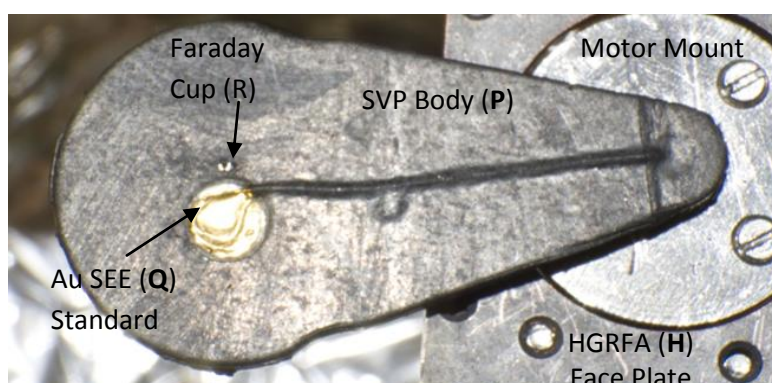


FIG. 2.20. Photograph of Au SEE standard and Aquadag surface of the SVP.

graphite is 0.9 (Nickles, 2002) as compared with peak yields of 2.4 for typical oxidized aluminum (Dennison, 2004).

The four SVP wires (large electrode, small electrode, Au sample, and Faraday cup/probe body) are threaded through the motor's 1.8 mm diameter hole and taken through the back of the motor positioning plate (FIG. 2.21b and c). The mount plate is attached to the motor via the two

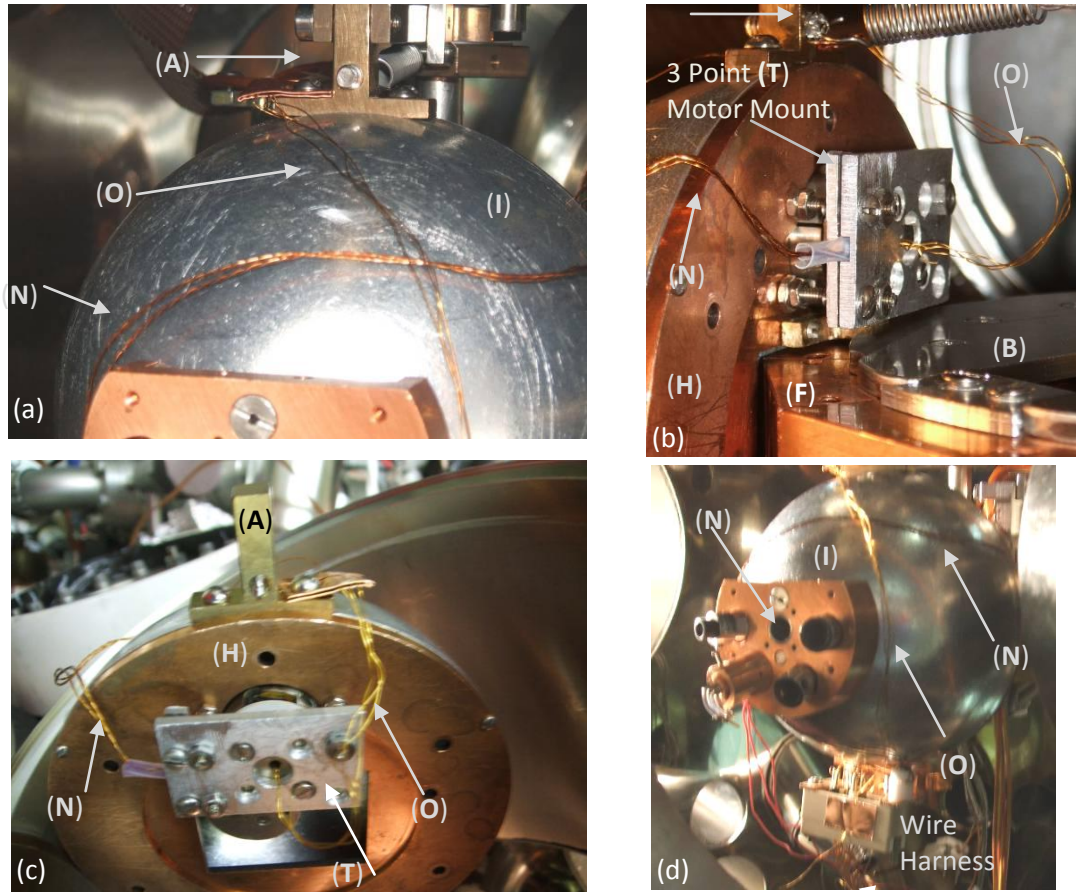


FIG. 2.21. Photographs of SVP motor and control wire routing: front and rear views. (a) Mounting of HGRFA. (b) Side view of the mounting of the Attocube UHF stepper motor. (c) Front view of Attocube UHF Stepper motor mount. (d) Isometric view of the HGRFA detailing.

M 2 3 mm screws and the SVP is positioned parallel to the HGRFA face plate (<2 mm) (FIG. 2.21) by a three-point floating clamp. The five motor control wires, three positioner (Voltage, Sweep, Ground) and two motor control (Power and Ground), are fed through the side of the motor positioning plate and clamped with a protective PTFE tubing (FIG. 2.21 b and c). In vacuum tests have shown when the four SVP wires are clamped, a significant amount of torque was placed on the motor, and motion was hindered when pressures reached $<10^8$ Torr. The hindrance in motor movement could be seen in air when the motor voltage is dropped to 16 V. Subsequent tests with the wires coming straight out the back of the motor as seen in FIG. 2.21 b and c show full motion is achieved in vacuum when there remains full motion with 14 V applied

to the motion controller in air. The motor wires are attached to the back of the HGRFA as seen in FIG. 2.21 (a) and fed into a ribbon cable that is attached to the wire clamp at the bottom of the HGRFA, eliminating the chance of damaging to the probe wires during normal operation FIG. 2.21 (d) .

To position the probe relative to the HGRFA, a printed template is used (FIG. 2.22). The probe is aligned using a printed template based off dimensions from the solid model FIG. 2.23. Twenty-two templates specifying specific positions of the probe were printed using defining features of the probe and stage, such as sapphire sphere holes, both 3 mm and 7 mm electrodes, and the 10 mm sample refer to FIG. 2.22. These templates were printed on transparency paper and then carefully aligned over the front of the face plate. The probe is moved with the stepper motor in one step increments until the outline of the probe matches the outline on the transparency. The voltages of the motor's potentiometer are noted for use in setting the absolute position of the SVP in the LABView™ motion control program. This method of alignment is estimated to be related to the printer's reproducibility and is accurate within 0.050° or 0.025 mm.

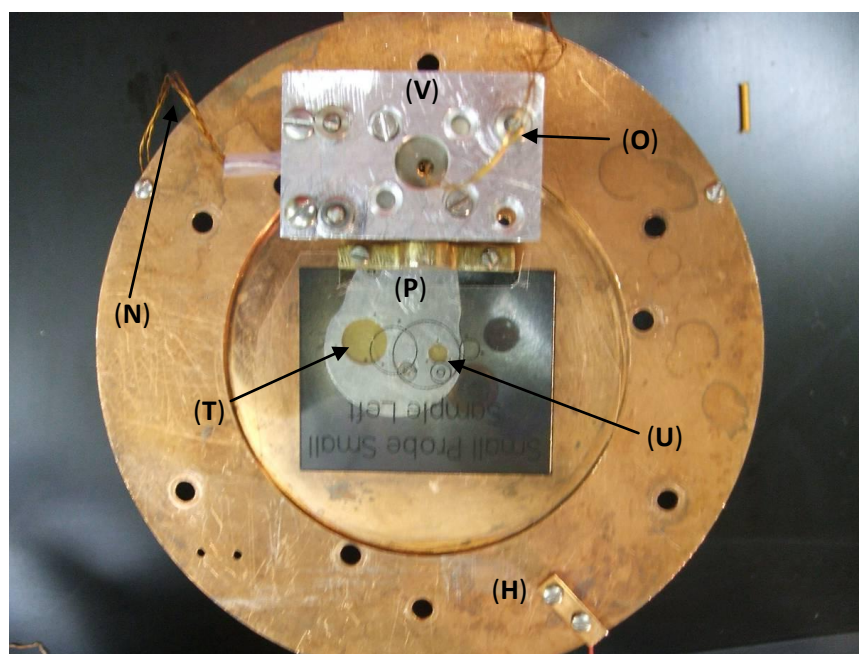


FIG. 2.22. Photograph of positioning using a template.

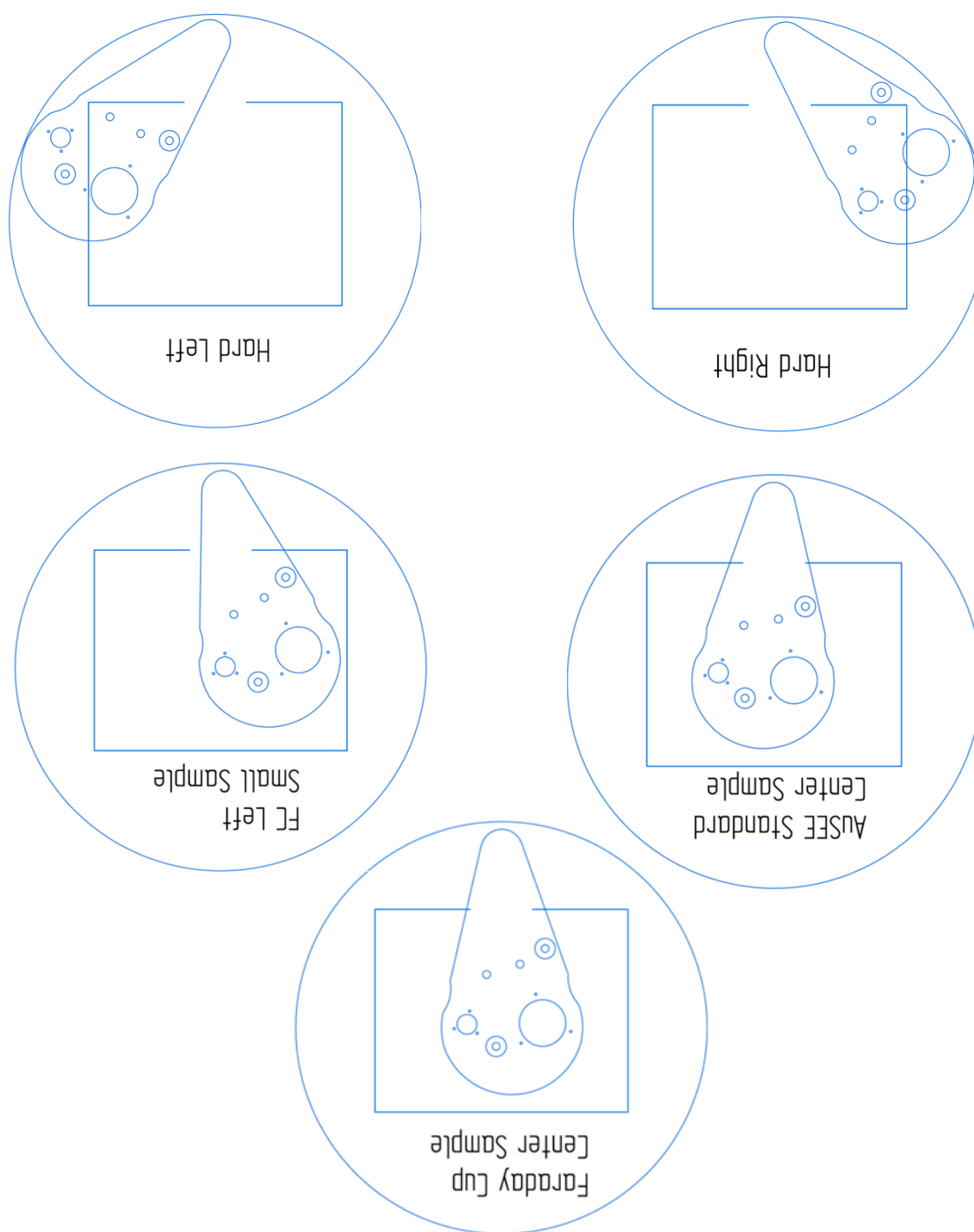


FIG. 2.23. Full-scale alignment template for LABView automatic positioning sequences. Templates used to find a corresponding potentiometer voltage for a given SVP position. Each template is printed as is at full scale on a transparency. The images are laid out to best help the experimenter when calibrating the instrument. The template is placed in the depression on the outside of the face plate with the words facing the SVP and carefully aligning the window outlines with the HGRFA face plate window. The SVP is moved until it aligns with the transparency. The positioned voltage is recorded for the LABView™ program.

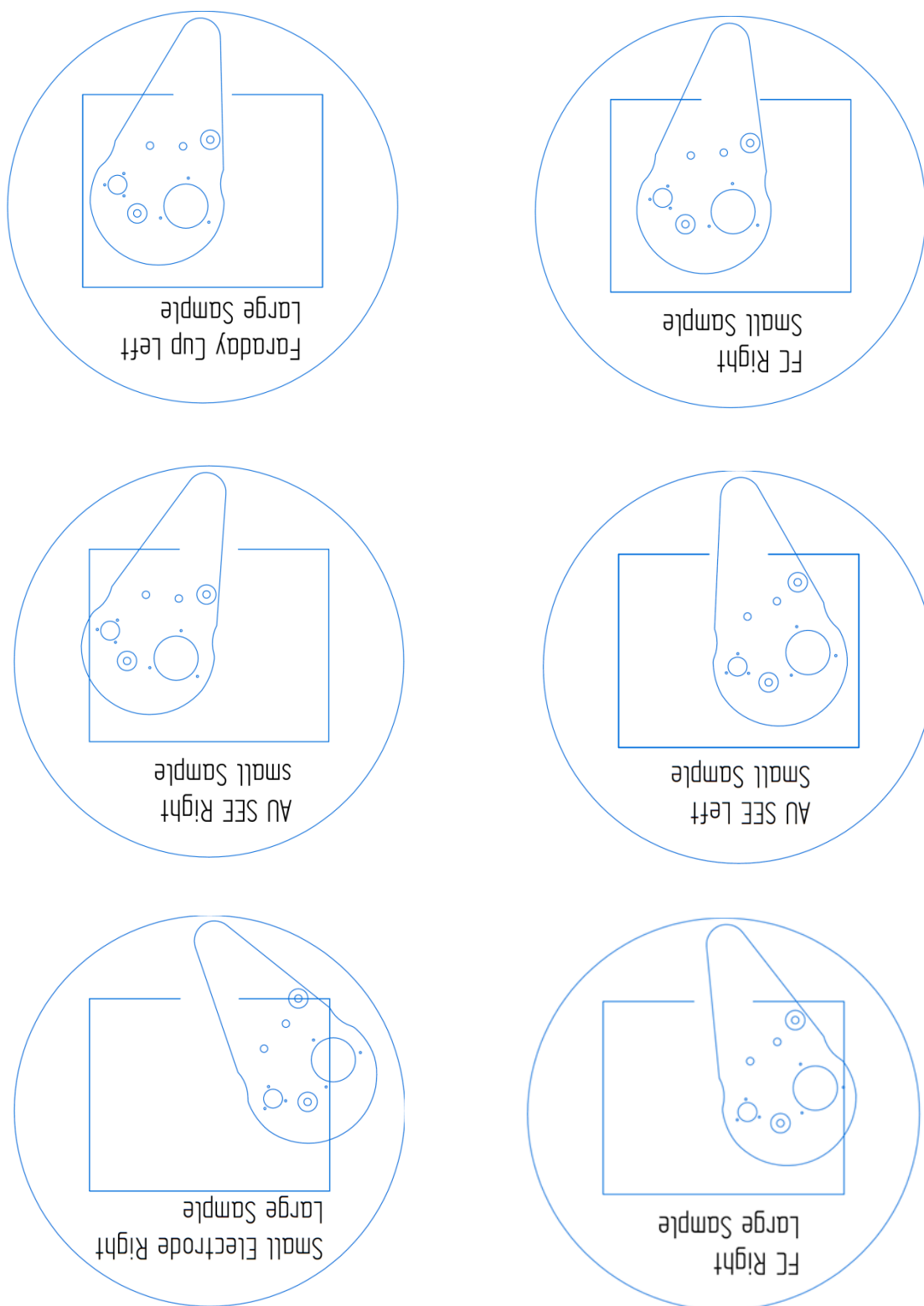


FIG. 2.23 con't. Full-scale alignment template for LABView automatic positioning sequences.



FIG. 2.23 con't. Full-scale alignment template for LABView automatic positioning sequences.

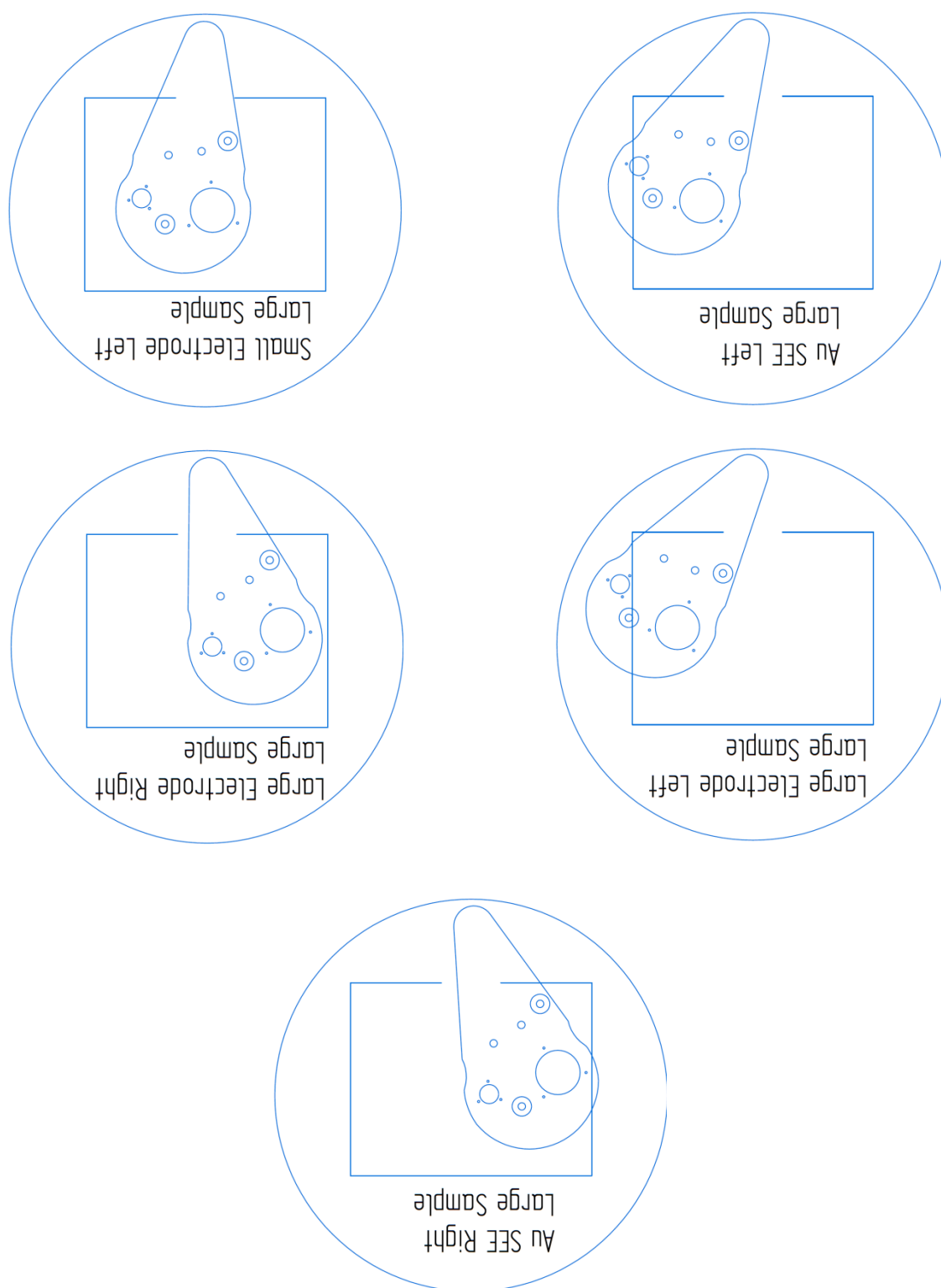


FIG. 2.23. con't. Full-scale alignment template for LABView automatic positioning sequences.

2.3.4. Extended Analysis Features

In addition to the SVP's voltage sensing electrodes, there are two features incorporated into the probe, which facilitate *in situ* calibration of the electron beam. A Faraday cup is placed in the center of the probe body and can be used, while measuring the current of the probe body, to center the beam on the sample. The Faraday cup is essentially a hole used to measure the electron (or ion) beam current without losing SE's or BSE's that would effectively reduce (or increase) the actual incident current. The typical design for a Faraday cup employs a ratio of 10:1 between the depth of the hole and the diameter of the aperture so that ~97% of the electrons emitted as a result of the incident beam do not escape the Faraday cup (Kite *et al.*, 2000). The Faraday cup has a minimized diameter of 0.35 ± 0.02 mm and a maximized depth of 2.02 ± 0.02 mm, making the largest depth to diameter ratio 5.8:1.

Use of this *in situ* Faraday cup removes the step of moving the HGRFA from the sample stage Faraday cup, to the sample, where it is estimated the largest error in positioning the beam in the center of the sample occurs. This feature can be particularly important for insulating samples where it is important not to expose the sample to the electron beam prior to commencing an experimental test. In this case, the Faraday cup can be centered over the sample, fully blocking electron impingement on the sample. The sample carousel can now be moved or the electrostatic deflection of the electron gun can be used to align the beam with the Faraday cup and the underlying sample without exposing the sample to the beam.

The second feature is a 4.15 mm Au disc located on the back of the probe body (FIG. 2.20). It is provided as a secondary electron emission (SEE) standard. It has a large maximum yield, σ_{\max} , of 1.8. Au is largely inert and does not oxidize. USU MPG has done a lot of work on Au as a standard (Davies, 1996; Kite *et al.*, 2000; Thomson, 2004).

2.4. Automation

2.4.1. LABView™ Interface

The use of a computer control interface is necessary to accomplish precision movements, long-term data collection, rapid data collection, and control of stability criteria. A LABView™ program was developed to control the movement of the probe and the collection of current, voltage, and timing data. The program has functions as simple as reading the SVP position, and ones of much higher complexities such as measuring surface voltage as the probe is swept across the sample face. The program collects 1000 data points every second providing the user with a standard deviation of the average of these points. The user has the ability to specify how many points should be taken throughout the course of the measurements. The LABView™ program records this data to a .txt file that is composed of five columns of data (Sample Voltage, Sample Standard Deviation, Probe Voltage, Probe Standard Deviation, and time).

Figure 2.15 shows a screen shot of the LABView™ front panel. The program allows for several inputs. The main program input dictates which loop the program runs through. The options for this loop are: Read Position, Auto Move, Manual Move, Long Decay, and Sample Sweep. A secondary input tab allows for a selection of the position of the probe to be set. The choices for the position input tab are: hard left (FIG. 2.22 q), hard right (FIG. 2.22 a), Au SEE standard (FIG. 2.22 n), Faraday cup (FIG. 2.22 p), small electrode (FIG. 2.22 k), and large electrode (FIG. 2.22 l).

The most basic loop is the Read Position loop. It takes voltage readings from the SVP's potentiometer and updates its position based on the precision alignment measurements used to set the probe position zero as discussed in Section 2.3.3. This updated number is graphed and the position is visualized on the front panel. The Read Position is best used when determining where the probe is. The loop should be used whenever the HGFRA is being moved from sample to

sample. The graphical interface can be used as a preventative measure to ensure that the SVP is not damaged during this movement.

The Manual Move and the Auto Move loops perform the same actions. They send information regarding steps, frequency, and amplitude to the Attocube motor controller. The Manual Move loop allows for the user to enter these values on the front panel. The program will pass this information to the motor controller to move the motor. The user should take care to not input any amplitude higher than 65 V and stay under 2000 Hz for long periods of time to avoid damaging the piezoelectric crystal due to overheating (Attocube Systems, 2008). If voltages and frequencies higher than this are needed for movement, refer to the Attocube ANR50 manual prior to movement. The Auto Move loop takes the position input tab value and calculates the number of steps to take based on the reading of the probe's current position. It passes the calculated number of steps, a 20 V amplitude, and a 825 Hz frequency to the Attocube motor controller. These values were chosen based on the speed and accuracy during in-vacuum motion tests. The program then repeats this loop until it reaches an acceptable tolerance of the probe position of six steps (30 m° or 0.013 mm).

The Long Decay loop is set up to measure surface voltage on a sample as it decays over long time periods. The loop is comprised of three functions: movement, data collection, and stability control. The movement is identical to the Auto Move loop; it provides movement from hard left, or hard right, to the selected feature in the position tab. Data are collected every second at 1000 Hz, unless specified by user, for a user specified number of points. Outputs of mean and standard deviation of the probe voltage, position, and time are written to a user specified file. The stability control is composed of a grounding sequence grounding the probe, a waiting sequence, and then an ungrounding sequence. Due to SVP drift, EFTP drift, and environmental effects, the measurements becomes inherently unstable. Periodic grounding of the probe minimizes these effects. Further explanations of drift and stability of the instruments are found in Section 3.1.

The final loop in the program is the Sweep loop. The Sweep loop is similar to the Long Decay loop. The difference between the two loops is the Long Decay loop moves the SVP directly to the desired location, takes data, then moves back to ground where the loop enters the stability control function, where the Sweep loop moves in increments across the entire sample taking data over each of a specified number of steps, before moving to ground and entering the stability control function.

2.4.2. Control Box

The addition of the control box increased system stability, reduced the noise in the system, and increased the speed of operation of the system. The schematic of the control box is shown in FIG. 2.24 and the schematic of the feedthrough cable shown in FIG. 2.25. It has three main components: a resistive position controller, an automatic ground controller, and a common ground plane.

The resistive positioner controller provides a front panel (FIG. 2.26) user-adjustable voltage (0 V-5 V) into the SVP resistive encoder, and returns a voltage signal, which identifies the location of the probe. To avoid putting an undesired voltage across the motor potentiometer, the control box is setup with a calibration potentiometer (P1 see FIG. 2.24 and FIG. 2.26). This matches the resistance of the SVP motor. With the resistance of the circuit matched to the motor's resistance, a voltage potentiometer (P2 see FIG. 2.24 and FIG. 2.26) can be used to adjust the voltage entering the motor. When adjusting the voltage to the motor, a front panel switch (S1 see FIG. 2.24 and FIG. 2.26) bypasses the motor and can be read via a front panel BNC. There are two front panel BNCs for potentiometer read outs and voltage calibration, and two back panel BNCs for positioning data sent directly to the DAQ card.

The SVP ground controller is a circuit that allows for a computer signal or a user input signal to switch a relay that controls a grounding solenoid. This solenoid grounds the selected witness plate, while the other witness plate is directly wired to ground. Grounding the probe when

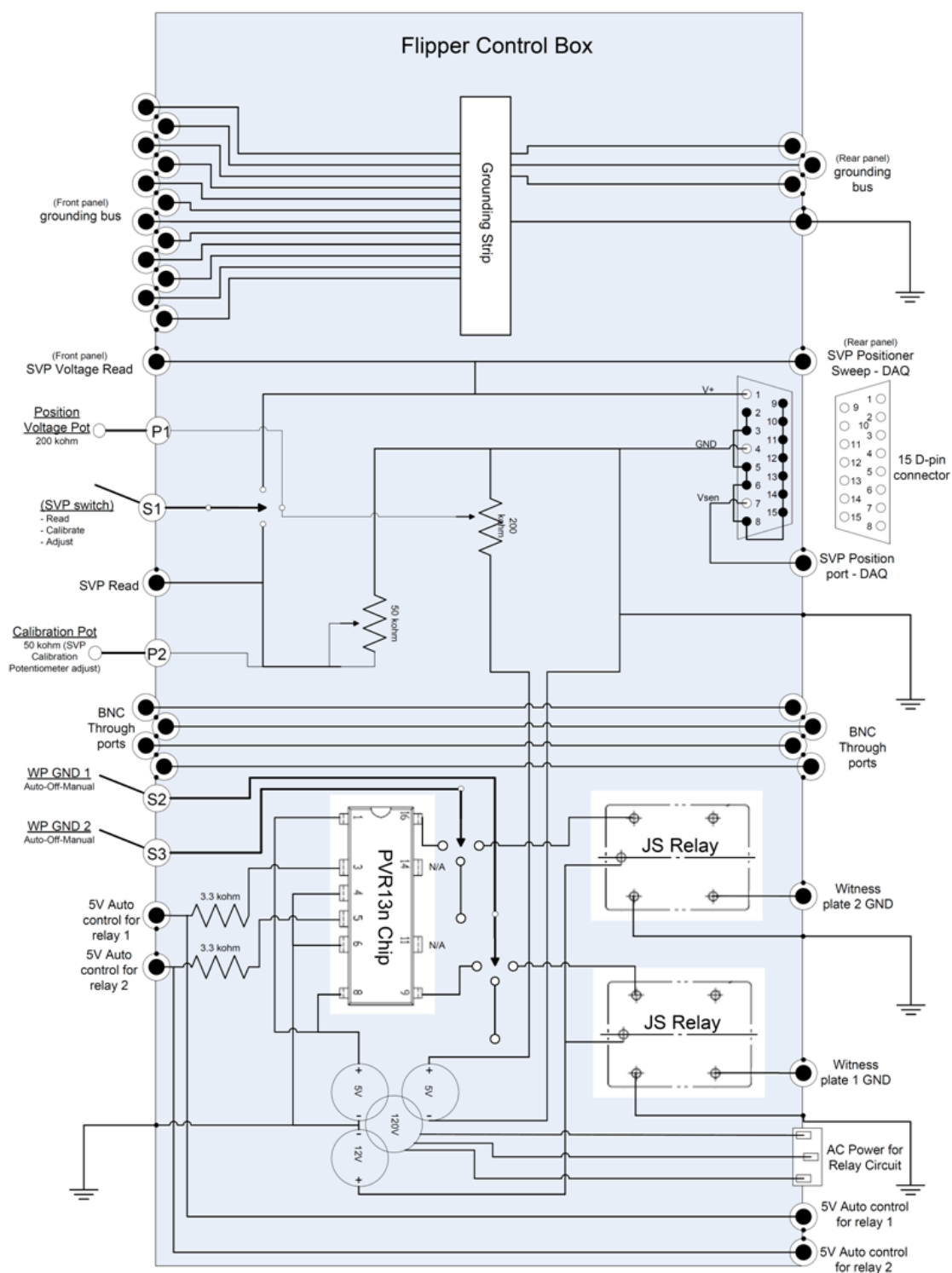


FIG. 2.24. Control box schematic.

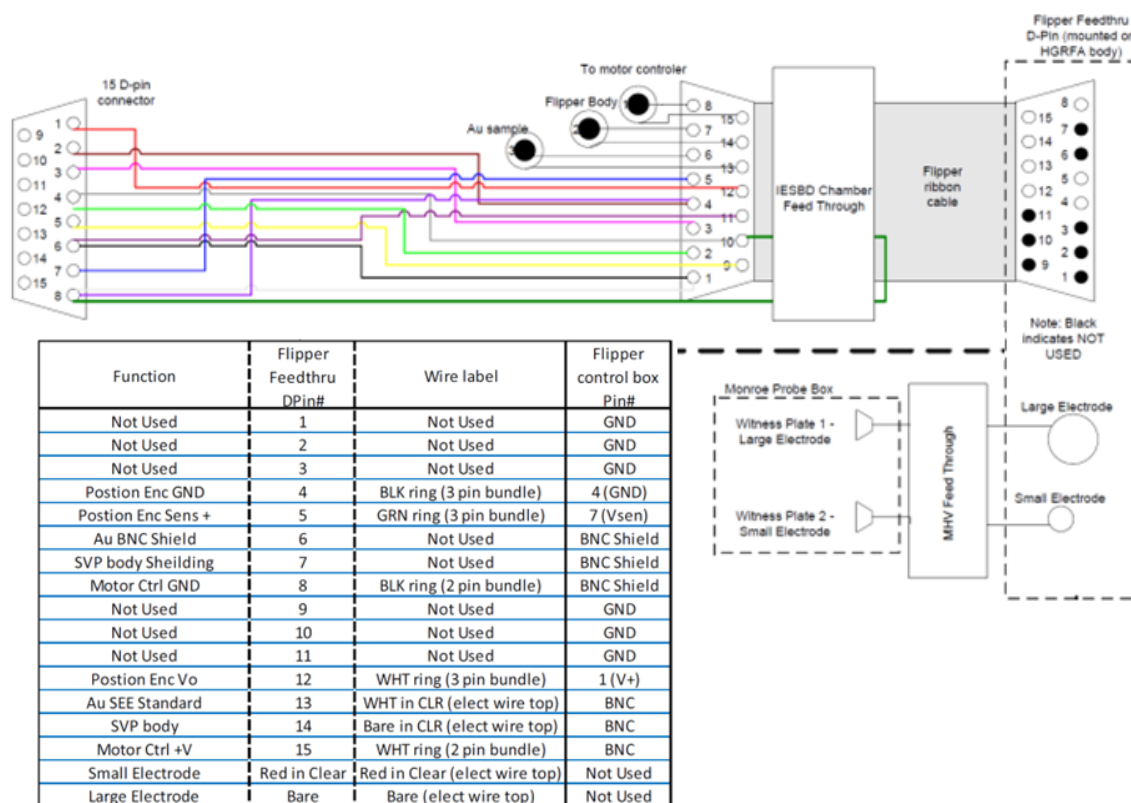
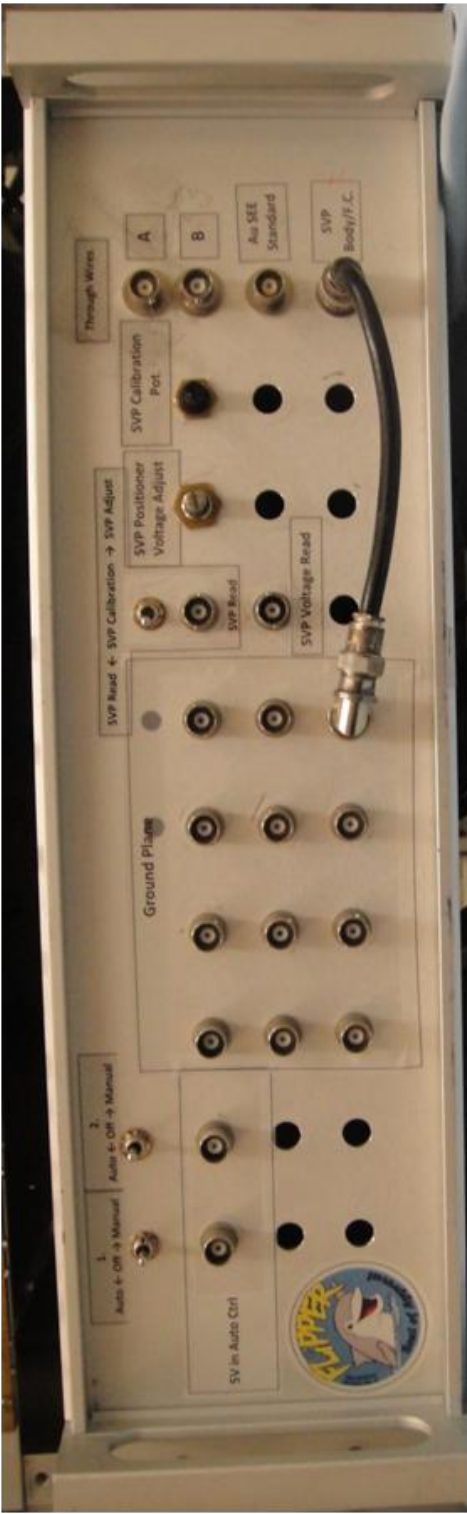


FIG. 2.25. Feedthrough cable layout.

over a grounded sample insures a net zero charge on the probe. The effects of grounding are discussed further in Section 3.1. The control box front panel has two selection switches (S2 and S3, see FIG. 2.24 and FIG. 2.26) for on/off or computer control, and an input for a 5 V TTL signal to be used in quick debugging and troubleshooting situations. The back panel has the output for the solenoid and a computer control input signal.

The common ground plane provides a common location for the common ground plane attachment of anything that needs to be grounded during operation and measurements of the SVP. The ground plane is nothing more than an array of 12 BNC connectors that allow different components to be grounded to a common chamber ground. Tests have shown that the grounding of components during data collection is of extreme importance and the greater detail paid to proper grounding practices, the fewer effects vibrational and electrical noise have on the measurements. Figure 2.27 shows a block diagram of the system layout.



Front Panel



Back Panel

FIG. 2.26. Front and back panels of SVP control box.

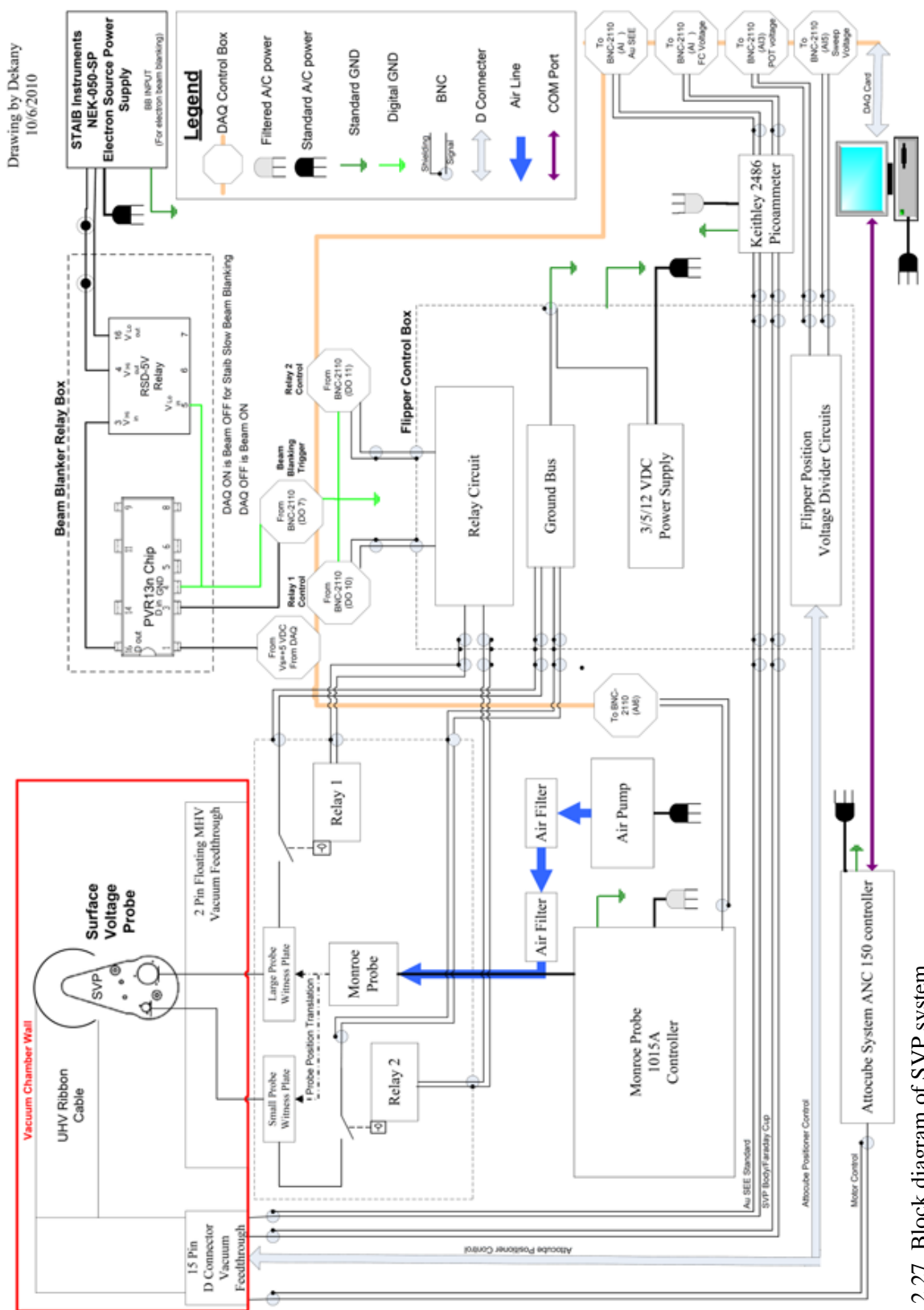


FIG. 2.27. Block diagram of SVP system.

Drawing by Dekany
10/6/2010

CHAPTER 3

INSTURMENTATION VALIDATION AND CHARACTERIZATION

This chapter discusses the testing and characterization of the SVP, as well as a method for data analysis. To understand how the SVP reacts to certain applied electric fields, extensive testing and calibration with grounded and biased conductors has been done. From proof of concept, through construction, to final implementation, the probe was tested along the way as shown in FIG. 3.1. Extensive *ex situ* testing was done to become familiar with the complexities of the probe. The drift, calibration factor, and stability were all evaluated and characterized before installing the probe into the vacuum chamber. The introduction of the probe into the vacuum chamber changed all these measurements. This would normally have been a cause for concern, but the complex nature of the SVP system and the anomalies that appeared during *ex situ* testing,

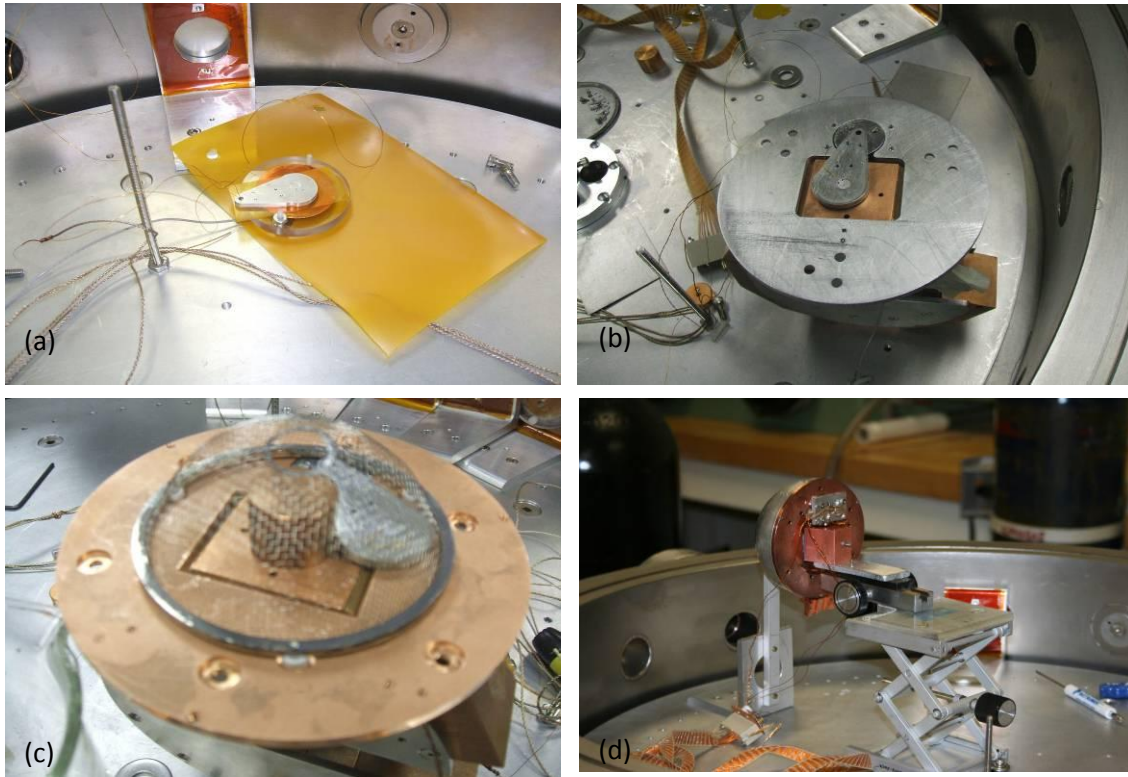


FIG. 3.1. Visual progression of *ex situ* testing. (a) Testing proof of concept before motor purchase. (b) Testing implementation of motor in new detector plate. (c) Testing clearance and effects of grids. (d) Testing of final assembly.

such as the hokey pokey effect discussed further in Section 3.1.1, demonstrated this was not a surprising result. In the end, the calibration tests detailed in this chapter have validated the measurement and data collection methods of the SVP.

In order to know the values the probe is measuring, it is imperative to determine the relationship between probe voltage and sample voltage. Using all drift information and the calibration factor the equation to find the sample voltage during anytime in the run is:

$$V_{sample} = CF \left[V_{probe} - V_{offset} - V_{elec_o} \left(1 + V_{elec}(t - t_d) \right) - V_{drift_o} \left(1 - e^{-\frac{(t-t_d)}{\tau_d}} \right) - \left(1 - e^{\beta V_{probe}} \right) \left(1 - e^{-\frac{(t-t_v)}{\tau_v}} \right) \right], \quad (3.1)$$

where the coefficients in Eq. (3.1) are outlined in TABLE 3.1.

TABLE 3.1. Definitions of values in the sample voltage equation.

CF	Linear voltage calibration compares sample voltage to probe voltage	$\frac{V_{probe}}{V_{Sample}}$	(1084.5±0.5) L.E. (14900±125) S.E.
V_{elec}	Offset of electronics value is enveloped in the Probe offset and adjusted by user on front panel of EFTP controller	$V_{offset} + V_{elec_o} [1 + V_{elec}(t - t_d)]$	(1.0±.8)mV
V_{elec_o}	Drift of the EFTP controller, value is small on typical timescales of measurements		Typically (2.0±0.2)mV/hr
V_{offset}	Probe Voltage Offset, determined from the exponential fit to the drift data		Measured each run (13±3)mV
V_{drift_o}	Probe ground drift rate, determined from the exponential fit to the drift data	$V_{drift_o} \left(1 - e^{-\frac{(t-t_d)}{\tau_d}} \right)$	Measured each run (32±1)mV/s
τ_d	Time constant of the probe ground drift, determined from the exponential fit to the drift data		Measured each run typical on the order of (1400±100) s
B	Sample voltage drift slope, determined from the exponential fit to the drift data	$(1 - e^{V/\beta}) \left(1 - e^{-\frac{(t-t_v)}{\tau_v}} \right)$	(-6x10 ⁻⁶ ±2x10 ⁻⁶) mV
τ_v	Time constant of sample voltage drift, determined from the exponential fit to the drift data		(0.4±0.4) s

3.1. *Ex Situ* Testing

In order to determine the characteristics of the new SVP instrument, a vacuum chamber shell was modified to do in-air testing (FIG. 3.1 d). In-air testing allowed for modifications, trouble shooting, and easy testing of critical items, such as sample distance and sample size. The chamber shell had Conflate flanges and ports, which allowed the probe to be setup in a manner similar to how it is used in the Electron Emission chamber. The lengths and connections of components were kept as close to the final setup as possible. A variable-voltage supply (Bertan Model 230 0-1 kV) was connected to an OFHC Cu conductor mounted on a sample block to simulate a charged sample. This block was setup on an adjustable positioning mount to control probe-to-sample spacing, and vertical alignment (FIG. 3.1 d). Measurements such as noise, ground drift, and voltage drift of the system were monitored and characterized.

Initial characterization and drift measurements showed the importance of the need for proper grounding, as ground drifts were large and obtrusive (15 ± 3 mV/s) to the stability and accuracy of the measurements. The grounding of the SVP and unused elements (Au SEE standard and small electrode) reduced the drift of the system to acceptable, but still relatively high levels (8.9 ± 0.01 mV/s see FIG. 3.2). Once satisfied with the drift results, voltages were applied to the

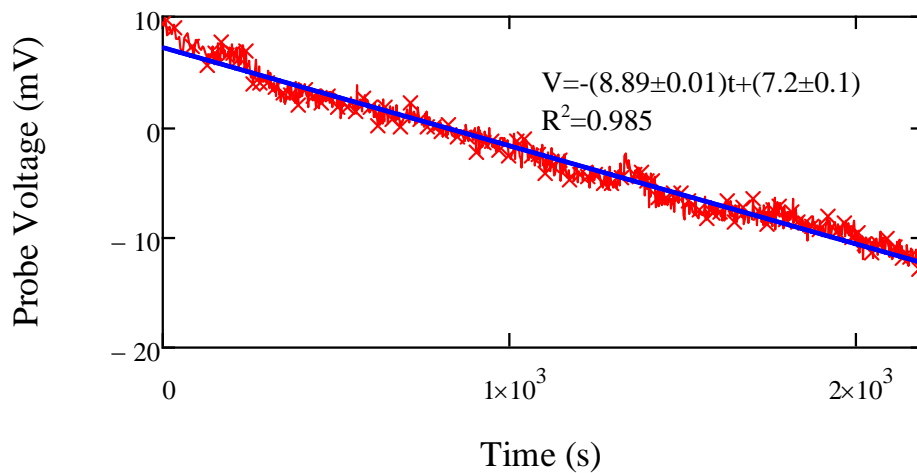


FIG. 3.2. Preliminary *ex situ* drift measurements, showing a large linear drift effect.

sample. Calibration factors and voltages drifts were measured, usually giving a calibration factor of $\sim 500 V_{\text{sample}}/V_{\text{probe}}$ with drifts results approximately $\sim 8 \text{ mV/s}$. These results, however, were sometimes unpredictable, making it impossible to achieve the measurement accuracy required in Chapter 2. The most unpredictable results were measured with people present in the room.

After some careful investigation, the phenomena now known as the hokey pokey effect was discovered. As the probe was positioned over a grounded sample and the voltage monitored, the extreme sensitivity of the instrument was evident. When monitoring the probe voltage a 60% increase was seen when a person walked into the room. When that person lifted his foot, a decrease of 30% was observed. The voltage would return to the 60% increase when the person put his foot back on the ground. This effect disappeared when the person removed his shoes or exited the room, further complicating the physics behind this effect. This effect scaled linearly with the addition of more people in the room. FIG. 3.3 shows the hokey pokey effect and demonstrates the drastic changes that resulted from what appeared to be insignificant changes in the environment.

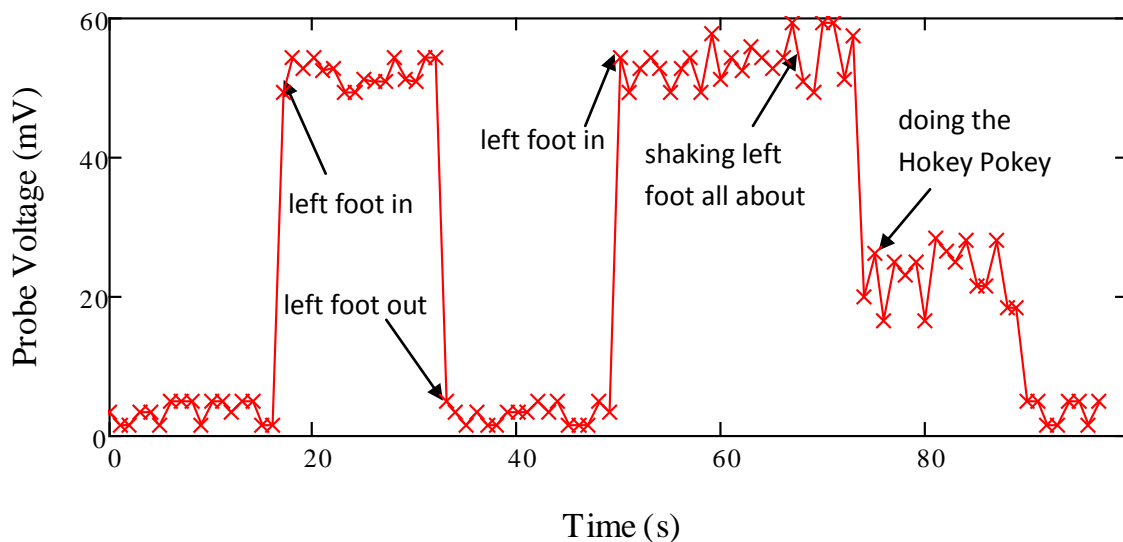


FIG. 3.3. Hokey pokey effect. The hokey pokey effect shows the extreme sensitivity of the probe. What is it all about?

A Faraday cage was set up around the probe to reduce such environmental effects (FIG.

3.4) on the probe. The vacuum chamber walls or a perforated metal cover acted as a Faraday cage and caused a significant decrease in measured results. The drift effects were reduced to 4.1 ± 0.3 mV/s with the Faraday cage. Due to a significant decrease in the measurements of the instruments drift, all tests were repeated *in vacuo*. However, results obtained on the probe-to-sample distance and test methods developed to correct for the probe drift still proved useful.

3.2. Ground Drift

Three different types of drift measurements were made to calibrate the instrument, EFTP drift (V_{elec} , V_{elec_o}), ground drift (V_{drift_o} , τ_d), and voltage drift (β_v , τ_v). Each drift provides instabilities in the system and each drift is accounted for in the final results. All measurements were taken in vacuum with pressures $<10^{-7}$ Torr to reduce the RC time constant, as found in 2.3.1.1.

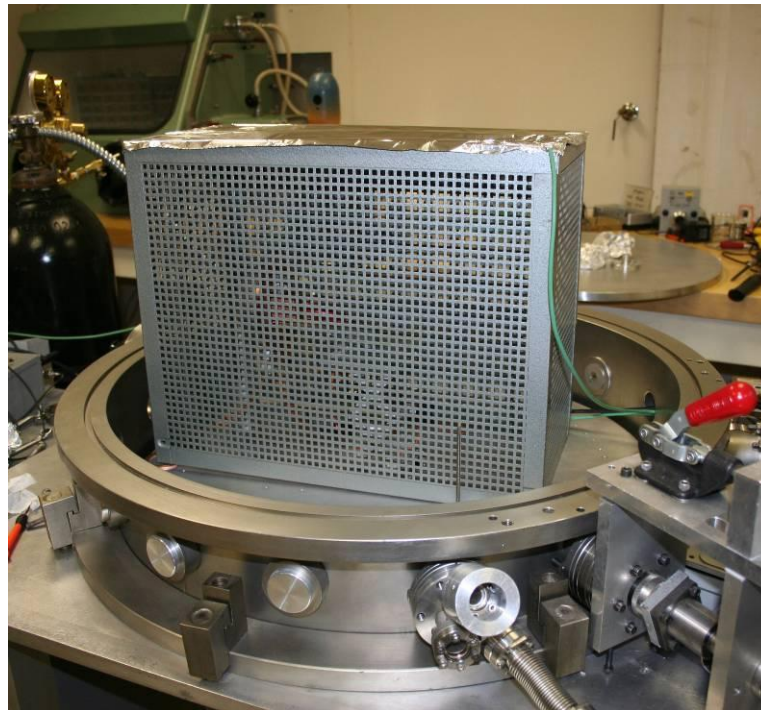


FIG. 3.4. Faraday cage to help reduce the noise of the *ex situ* tests.

The EFTP drift is the zero drift of the electrostatic field probe and the controller. This is measured by grounding the witness plate and monitoring the probe voltage (FIG. 3.5 a). Drift from the probe is caused by the open aperture on the probe necessary to take measurements. Foreign materials may enter the volume associated with the vibrating vane causing undesirable effects on the noise or a DC offset. The probe has a dry air purge line that blows 2 cfph of filtered air across the vane creating a positive pressure, which reduces the drift of the probe and stabilizes the measurements. Figure 3.6 shows the long-term drift of the probe's zero voltage with the dry air purge running. A voltage offset V_{electo} appears when the ground is removed from the witness plate. This effect has been decreased to $< (10 \pm 3)$ mV by implementation of the grounding system explained in Chapter 2.

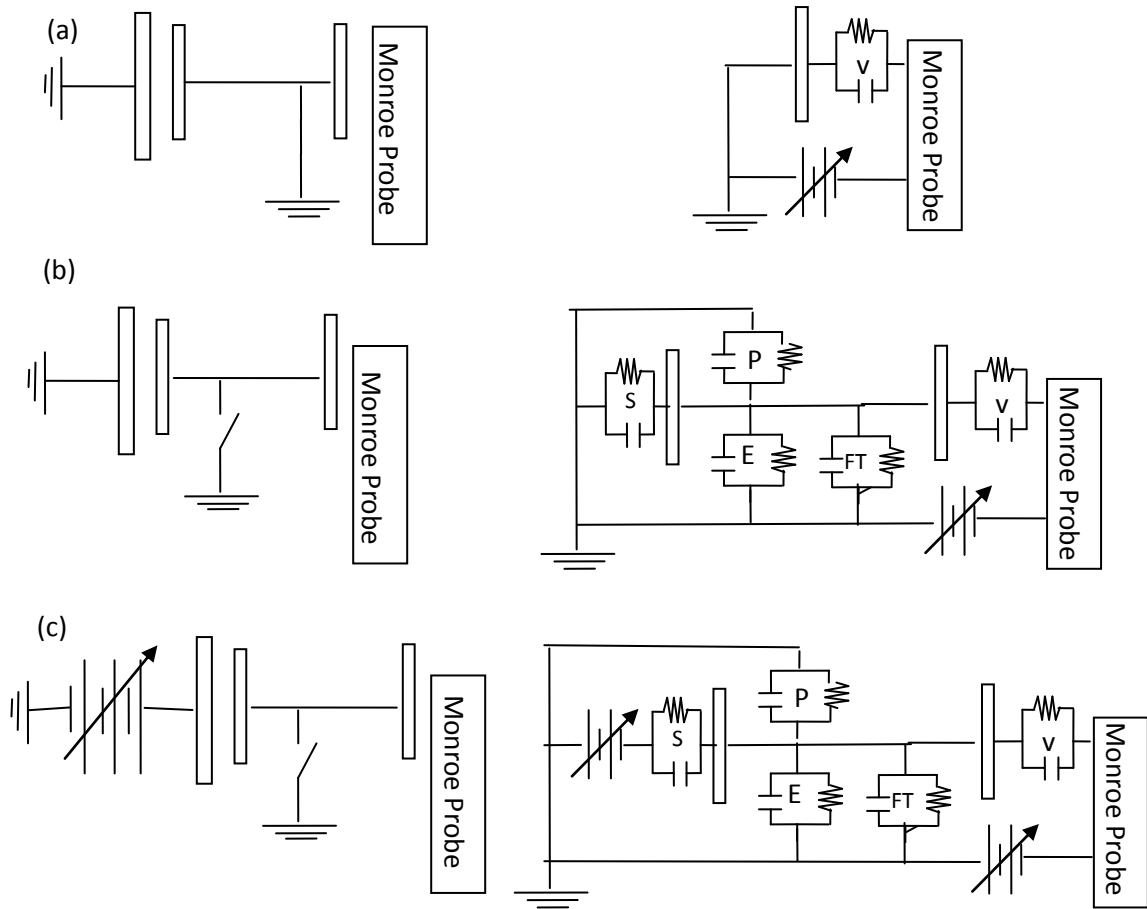


FIG. 3.5. Three calibration setups and their corresponding electrical diagram to measure different drifts of the system.

The ground drift measurement is done by measuring the EFTP voltage while switching between the configuration in (FIG. 3.5 a and b). The probe voltage of configuration FIG. 3.5 (b) was measured for three lengths of time, long (~24 hr), intermediate (~3600 s), and short (~60 s). Over long periods of time, the drift is not stable and changes in slope have been seen. This is exaggerated in *ex situ* testing and is seen in FIG. 3.7. The drift is due to charge being acquired by the SVP. This charge can come from many places, for example from the Malter effect from the sample, from ions in the atmosphere, or the triboelectric effect from small movements or vibrations.

Over intermediate times, the drift has the form of charging capacitor TABLE 3.1. V_{drift_0} is related to the capacitance of the system and τ_d is related to the effective resistance and

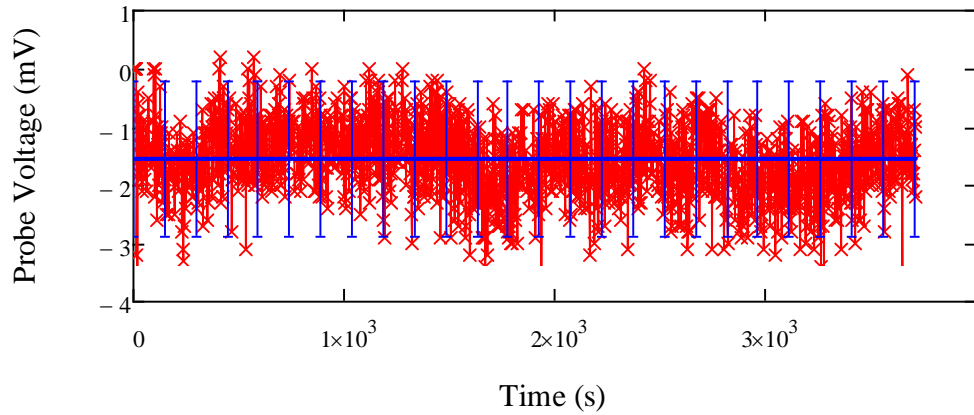


FIG. 3.6. Long-term drift of a grounded witness plate detailing Monroe probe controller drift. Drift of controller is within the standard deviation of the mean (blue) of typical probe measurements.

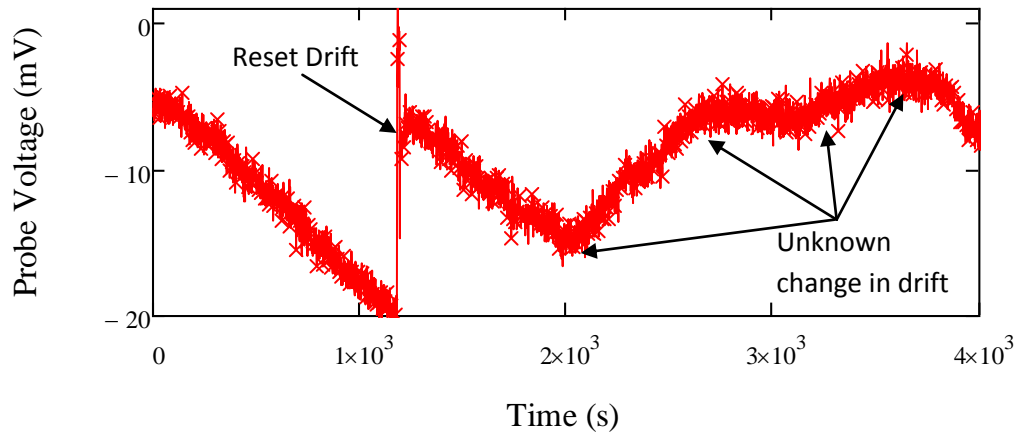


FIG. 3.7. Long-term *ex situ* drift test shows extreme changes of slope in short time periods.

capacitance. Tests (See FIG. 3.8) have shown the capacitance and resistance of the system do not remain constant. The drift over these two consecutive runs show distinctly different amplitudes (V_{drift_o} (Run 1 0.411 ± 0.001 V, Run 2 0.362 ± 0.001 V) and time constants τ_d (Run 1 1325 ± 34 s, Run 2 1450 ± 36 s). Operationally, this requires a grounded drift measurement be made frequently, before each set of surface voltage measurements. This determines a unique set of constants V_{drift_o} and τ_d , for each time the SVP is ungrounded.

For short timescales the drift tends to be on the order of $< (1.0 \pm 0.8)$ mV/s. A Taylor series expansion can be made of the exponential decay giving a linear approximation, Eq (3.2).

$$V_a(t) = V_{offset} + \frac{V_{drift_o}}{\tau_d} t - \dots O(h^2). \quad (3.2)$$

The uncertainty $\Delta V_a(t)$ is given by Eq (3.3) as

$$\Delta V_a(t) = \sqrt{\frac{1}{N-2} \sum_{i=1}^N \left(y_i - V_{offset} - \frac{V_{drift_o}}{\tau_d} t \right)^2}. \quad (3.3)$$

Typical uncertainties of the drift are calculated to be 0.8 mV/s. Figure 3.9 shows the error

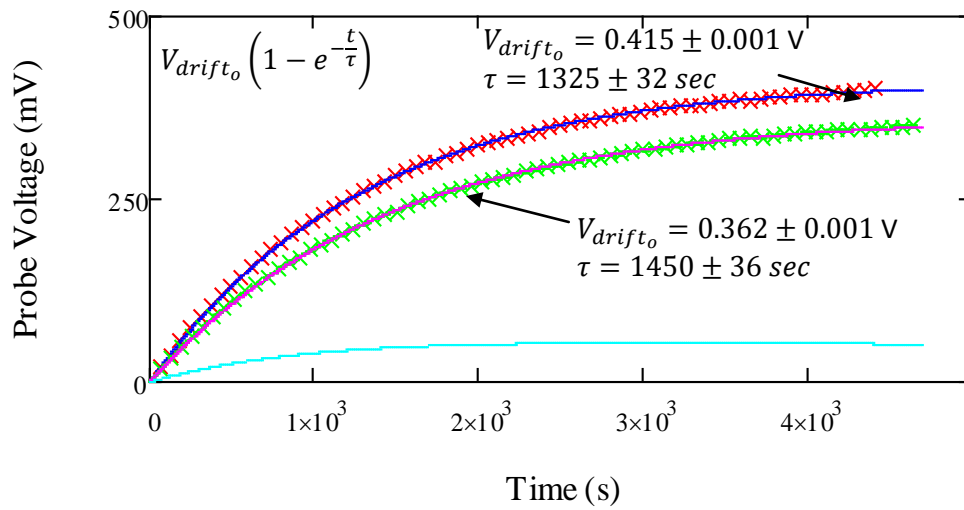


FIG. 3.8. Graph of *in situ* measurements and exponential fits of the drift of the SVP over ground. Cyan curve shows the difference in the exponential fits.

of a linear fit to an exponential decay. This approximation becomes large and exceeds the desired resolution at ~ 150 s. Errors can also increase to unacceptable values under some normal operations of the vacuum chamber. These operations are detailed below and should be used to avoid large errors in measurements.

Measurements cannot be taken at any time while the sample stage is moving. The added noise is attributed to both tribostatic effects and the noise from the pulsed motor control signals. Even at the slow translational rates of the automated LABView™-controlled movement of the sample stage (~ 0.1 mm/s), the standard deviation of the SVP over a grounded sample increases from ~ 1 mV to an undesirable amount of noise (~ 200 mV).

The probe cannot be used with any pressure gauge that uses a filament during operation. The filaments produce ions or electrons that will overwhelm the signal and produce a high enough charge to overload the Monroe probe, or create a large ground drift. To avoid this problem, pressure measurements, which are required to ensure pressures are low enough to run

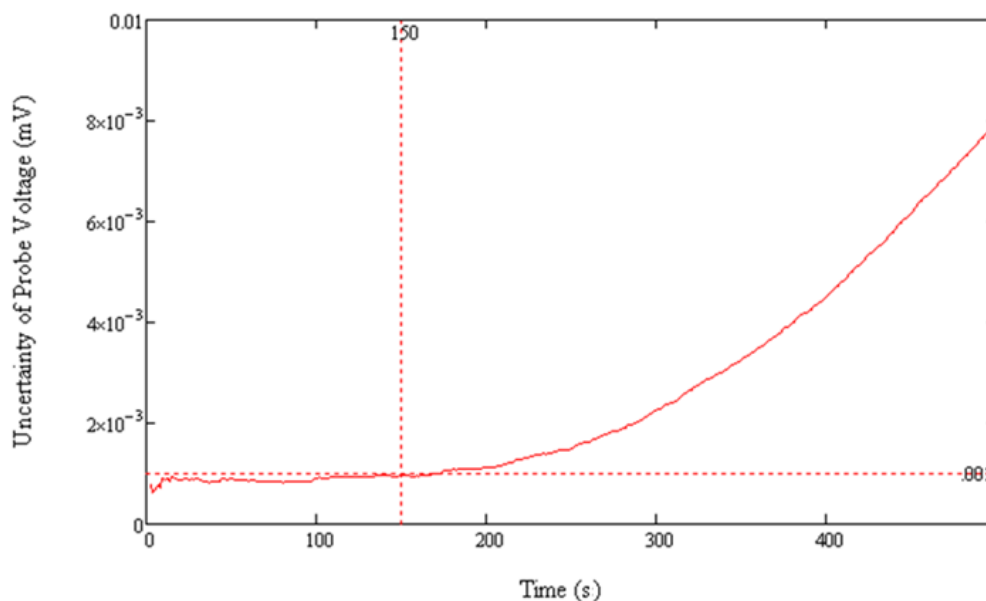


FIG. 3.9. Uncertainty in the linear approximation to the drift of a grounded sample. At 150 s (Vertical Line) the error of the linear approximation becomes larger than the error of the system (Horizontal Line).

the necessary equipment, should be taken prior to the collection of data. Once all voltage probe measurements are complete, another pressure measurement can be taken to confirm the chamber is still under sufficient vacuum conditions. If, as taking voltage probe data over several days, monitoring of the vacuum pressure is necessary, it is advisable to take the measurements during a period when the probe is grounded to avoid negatively impacting the voltage probe data.

Vacuum pumps are another source of electrons or ions that can increase ground drift. Unfortunately, turning off the pumps is not an option. Loss in ultrahigh vacuum is detrimental to electron sources and other equipment used during typical measurements. Vibrations from the mechanical pump and both vibrations and high-frequency electrical noise from the turbo molecular pump have been shown to adversely affect the ground drift rate. Both these pumps should typically be off during SVP measurements. This is not usually a problem as the ion pump is the only pump running during routine low pressure ($\leq 10^{-7}$ Torr) operation of the chamber. The drift from the ion pump has been shown to be detrimental in past measurements, but has been reduced dramatically with proper grounding. The ground drifts caused by the ion pump have been reduced to an acceptable level through grounding. A second step has been shown to further reduce ground drift due to ion pump operation. The ion pump is located in the bottom of the chamber, separated from the sample holder and SVP by a poppet valve. Partially closing this poppet valve can minimize ground drift from the ion pump, without completely stopping the vacuum pumping. It is recommended the poppet valve be closed gradually, until the ground drift is diminished sufficiently for the application at hand. This will help retain the pressures of the chamber while reducing the noise.

3.3. Linear Calibration

The method of measuring the calibration curve uses the configuration in FIG. 3.5 (b) to get a ground drift measurement. A voltage is then applied via the configuration in FIG. 3.5 (c) and the probe voltage is monitored. The initial points are used in determination of CF. The

ground drift is reset by the configuration in FIG. 3.5 (a) and the measurements are repeated for a desired number of voltages. A LABView™ program (Flipper Ramp Up.llb) was modified to repeat a voltage ramp sequence for the calibration using a low-voltage supply (Agilent Model E3647: 0-60 V DC) 1 V to 10 V DC in 0.1 V increments, then to 10 V to 25 V in 0.25 V increments. The power supply was then switched to a high-voltage power supply (Bertan Model 230: 0-1 kV DC) and the voltage was ramped from 25 V to 1000 V in 25 V increments. The resulting data are shown in FIG. 3.10. Correcting for the ground drift, a very clear voltage drift is evident (see FIG. 3.11 d). This is discussed in the following section. Using the initial points of each voltage ramp a linear fit gives a calibration factor of 1084.0 ± 0.5 ($V_{\text{sample}}/V_{\text{probe}}$) ($\pm 0.05\%$) with a correlation coefficient of 1.00. Figure 3.12 shows three calibration curves for the large probe.

The sample voltage range of a single-surface voltage measurement with the SVP is thus estimated by this linear calibration slope and the overload voltage of the Monroe probe. The Monroe mV probe (Monroe Isoprobe, Model 162) can read measurements from -10 V to 10 V with a 1 mV resolution (Monroe Inc., 1994); this corresponds to a range in sample voltages of +10.8 kV to 10.8 kV to, with a low voltage of resolution of ~ 1.1 V with the large probe. This agrees with the linear calibration curve where the linearity of the curve diminishes at ~ 1.5 V.

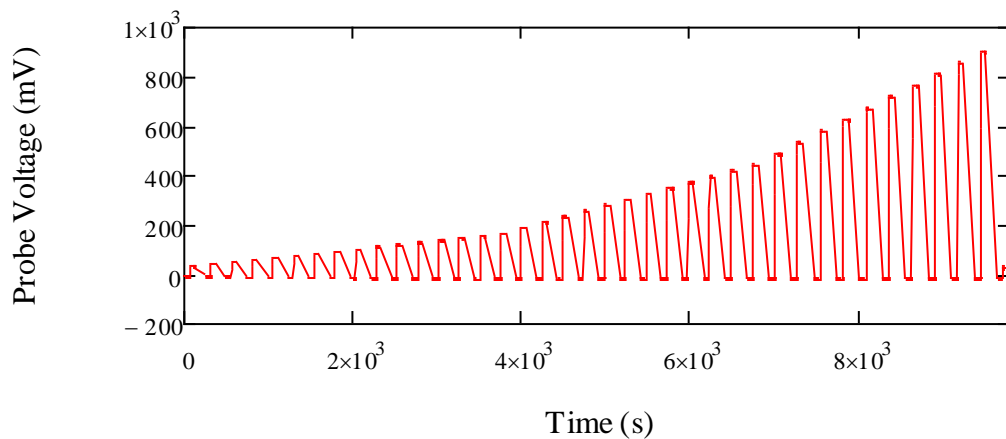


FIG. 3.10. Large probe calibration curve data (uncorrected). Peaks represent charged sample measurements, and valleys represent grounded drift measurements.

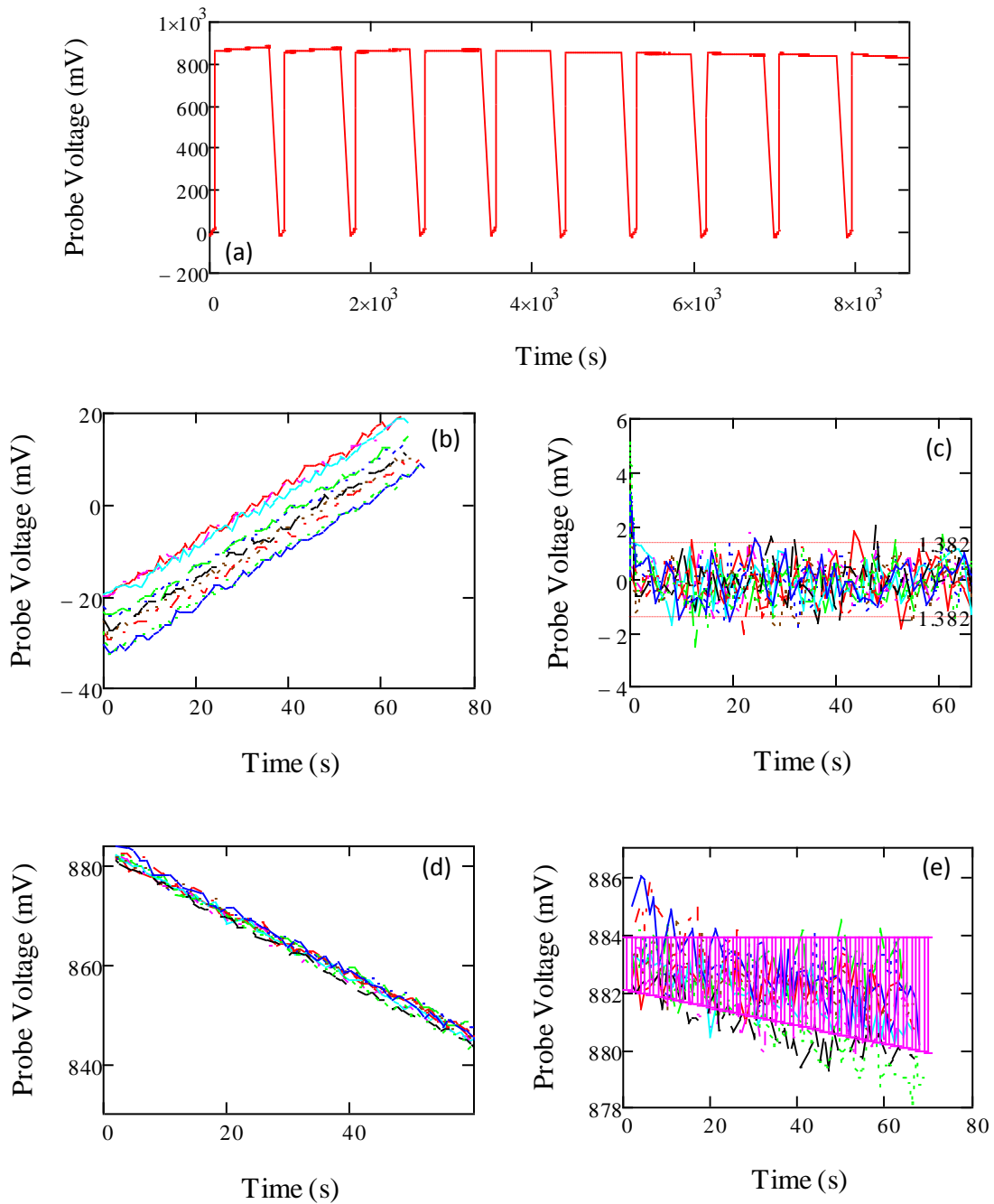


FIG. 3.11. Repeated 10 voltage ramp runs of 1000 V sample voltage with corrections. (a) Raw data showing plot of voltage versus time for 10 ~600 s, voltage ramps. (b) Each run has a unique ground drift that was monitored for ~60 s. (c) These drifts were automatically corrected for using a unique self calibration that applies a linear fit to each set of data and corrects the data based on the fit's unique slope and intercept. (d) The voltage runs are then separated and also corrected using the fitting parameters that correspond to the ground drifts. A significant slope remains after the data is corrected for. This is known as the voltage drift. A 1000 V sample voltage has a SVP voltage drift of 0.61 ± 0.02 mV/s. (e) Data were corrected for several different voltages and a correction for the voltage drift is used. The data seen in (e) has been corrected for both ground and voltage drift. This is the value used to determine the linear calibration curve.

The small electrode, as expected, has a much larger calibration factor. Measurements show a CF of $14890 \pm 125 \text{ V}_{\text{sample}}/\text{V}_{\text{probe}}$ (FIG. 3.13). By sacrificing resolution, the range of the small probe can be much higher. Theoretically the maximum sample voltage range of the surface voltage using the Monroe probe is $\pm 148 \text{ kV}$ with a resolution of 14.9 V . In practice, this value is $\sim 30 \text{ kV}$ based on arcing from the charged sample to the SVP, or the sample stage.

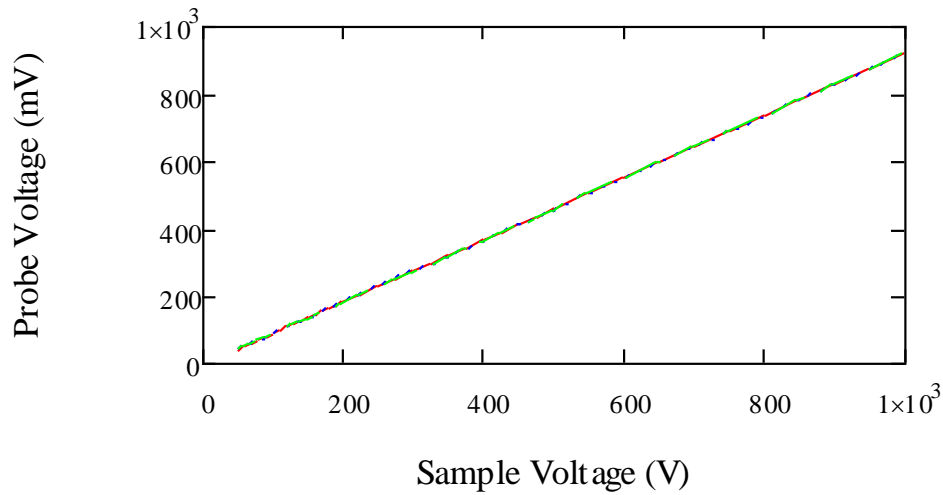


FIG. 3.12. Three superimposed calibration curves of the large electrode. The large electrode has a repeatable calibration factor of $\text{CF } 1084.5 \pm 0.5 \text{ V}_{\text{probe}}/\text{V}_{\text{sample}}$ and a correlation coefficient of 1.000.

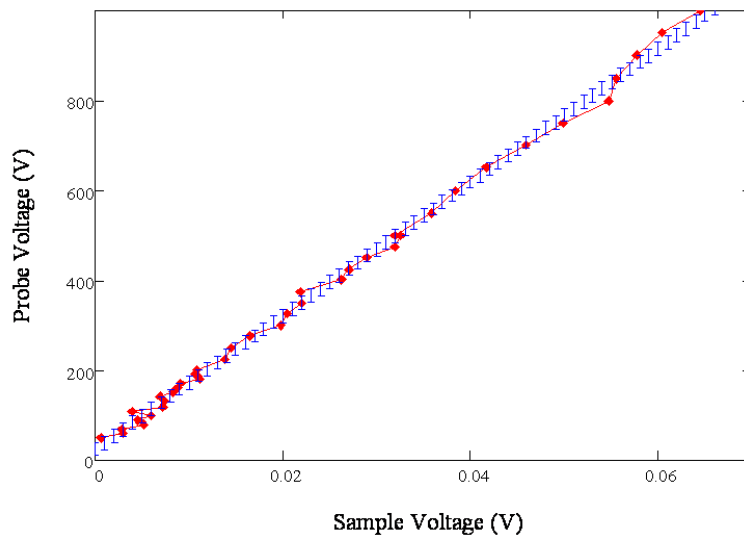


FIG. 3.13. Single small probe calibration curve $\text{CF } 14890 \pm 125 \text{ V}_{\text{sample}}/\text{V}_{\text{probe}}$.

3.4. Voltage Drifts

Close investigation of the data from the calibration curve showed the greater the sample voltage, the steeper the slope of the voltage drift (FIG. 3.11d). The voltage decays at a different rate than the ground drift, but approaches V_{drift_0} as shown in FIG. 3.14. This also shows the voltage drift takes on the exponential decay function shown in Table 3.1. Figure 3.14 (blue line) shows a long-term decay of the voltage drift for a 1000 V applied sample voltage. An exponential fit was applied with coefficients β_v and τ_v . Table 3.1 shows values for the time constants for vacuum measurements. The drift is attributed to charge on the SVP leaking to ground. Initial *ex situ* tests with the SVP show the voltage drift for equal magnitude negative and positive sample voltages are identical and drift toward a zero value. The voltage of the SVP decreases by 75% when the tests were done in vacuum. The increased drift in air is a result of the small distance between the probe body and the electrodes (<0.5 mm). Figure 3.15 shows the decay rate of the voltage drift, β/τ_v , as it changes with the corresponding probe voltage and is approximated by a linear relationship.

Repeated measurements were taken to ensure reproducibility of the voltage drift

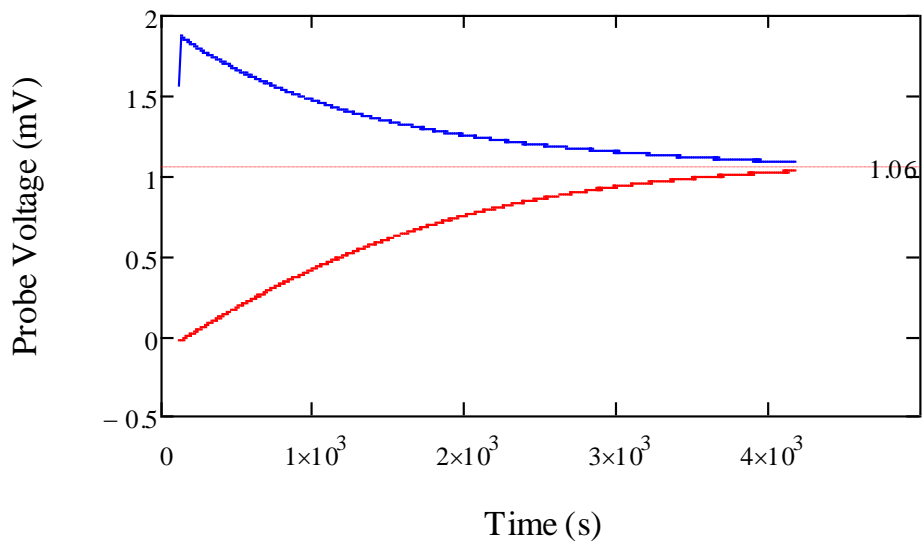


FIG. 3.14. Sample voltage (blue) and ground (red) measurements drift approach an equilibrium value V_{drift_0} (dashed line).

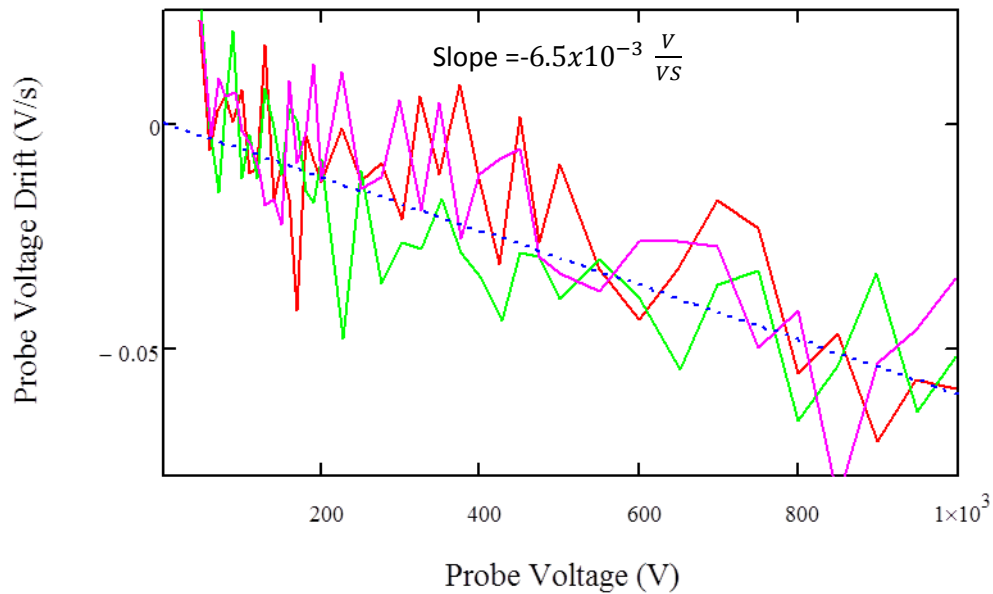


FIG. 3.15. Repeated measurements of slope of voltage drift versus probe voltage for the large electrode with a linear fit.

measurements. This is necessary as the self-calibration process is not possible during data runs as the sample voltage during actual data runs will be unknown. Caution must be used when using β and τ_v ; when the sample voltage is rapidly decaying, the probe voltage decay will be changing as well. It also must be noted when doing a sweep, the voltage changing because of the position of the probe will have a nontrivial effect on the voltage drift of the probe. This is explained more in Section 4.4.

3.5. Voltage Resolution

To reduce the uncertainty in surface voltage measurements associated with a single measurement, a computer-controlled algorithm was developed to acquire multiple voltage measurements. The SVP data are sampled at 1000 Hz for one second intervals. A standard deviation of a typical set of 1000 measurements is on average 1.2 mV, in agreement with the stated uncertainty of the Monroe probe controller of 1 mV. Errors associated with the measurements of the Monroe controller voltage by the DAQ card (NI model BNC-2110 16-bit)

are significantly less than the errors of the Monroe controller voltage. At $\pm 10\text{V}$ input to the DAQ card, the single-bit resolution is $\leq 0.3\text{ mV}$. The response time of the Monroe probe is 50 ms as set by the user (Monroe Inc., 1994). Thus, there are approximately 20 independent measurements of the probe voltage in each one second interval. For each second, the standard deviation of the mean of the 1000 point data set is $\sim 1.2\text{ mV}/\sqrt{20}$ or $\sim 0.2\text{ mV}$. This matches the uncertainty of the DAQ card, which thus sets the ultimate resolution, ΔV_{probe} .

Assuming linear approximations to the voltage drift and ground drift, and assuming the EFTP drift from the controller, V_{elec_o} , is zero, Eq. (3.1) can be linearized and reduced, Eq. (3.4).

$$V_{\text{sample}} = CF \left(V_{\text{probe}} \left(1 + \frac{\beta}{\tau_v} (t - t_v) \right) - V_{\text{offset}} + \frac{V_{\text{drift}_o}}{\tau_d} (t - t_d) \right). \quad (3.4)$$

To find the error in the measurement, the error of Eq. (3.4) needs to be evaluated. It is further assumed the time the SVP is ungrounded, t_d , and the time the SVP is over the charged sample, t_v , is short enough the error terms from these do not exceeded error of the nontime-dependent terms. Therefore, the nontime-dependent error terms will drive the errors in Eq. (3. 5):

$$\Delta V_{\text{sample}} = \Delta CF \left(V_{\text{probe}} \left(1 - \frac{\beta}{\tau_v} (t - t_v) \right) - V_{\text{offset}} - \frac{V_{\text{drift}}}{\tau_d} (t - t_d) \right) + \\ CF \left(\Delta V_{\text{probe}} \left(1 - \frac{\beta}{\tau_v} (t - t_v) \right) + \Delta V_{\text{offset}} - \Delta \frac{V_{\text{drift}}}{\tau_d} (t - t_d) \right). \quad (3.5)$$

In order to satisfy this last assumption, a time limit must be set for the probe to be ungrounded, as well as a limit for the time the probe to be over the charged sample. For this assumption to be true, the values of the four time-dependent terms need to be negligible compared to the Monroe probe terms. When looking at just the ground drift measurements, the error of the sample is given by:

$$\Delta V_{sample} = \Delta CF \left(V_{offset} - V_{probe} + \frac{V_{drift}}{\tau_d} (t - t_d) \right) + CF \left(\Delta V_{probe} + \Delta V_{offset} + \Delta \frac{V_{drift}}{\tau_d} (t - t_d) \right); \quad (3.6)$$

therefore, it is required that

$$(V_{probe} - V_{offset}) > -\frac{V_{drift}}{\tau_d} (t - t_d), \quad (3.7)$$

or in terms of uncertainties,

$$(\Delta V_{probe} + \Delta V_{offset}) > -\Delta \left(\frac{V_{drift}}{\tau_d} \right) (t - t_d). \quad (3.8)$$

Solving for t_d shows the probe cannot be ungrounded for longer than ~200 s. Eq. (3.9) dictates how long the SVP can be over a charged sample.

$$\Delta V_{sample} = \Delta CF \left(V_{probe} \left(1 + \frac{\beta}{\tau_v} (t - t_v) \right) - V_{offset} \right) + CF \left(\Delta V_{probe} \left(1 + \frac{\beta}{\tau_v} (t - t_v) \right) + \Delta V_{offset} \right). \quad (3.9)$$

Again, comparing the time-dependent terms gives:

$$V_{probe} - V_{offset} > -V_{probe} \frac{\beta}{\tau_v} (t - t_v) - V_{offset} \quad (3.10)$$

or in terms of uncertainties,

$$\Delta V_{probe} + \Delta V_{offset} > -\Delta V_{probe} \Delta \left(\frac{\beta}{\tau_v} \right) (t - t_v) - \Delta V_{offset}. \quad (3.11)$$

Solving for t_v shows the time the electrode can be over a charged sample is ~7000 s. Therefore, the error of the sample voltage error is driven by the ground drift, and for times less than ~200 seconds this error can be neglected. When this assumption is simplified, error in the sample voltage can be reduced to:

$$\Delta V_{sample} = \Delta CF(V_{probe}) + CF(\Delta V_{probe} + \Delta V_{offset}), \quad (3.12)$$

where ΔCF is the error and reproducibility of the slope for the calibration factor, ΔV_{probe} comes from the DAQ card error, and ΔV_{offset} comes from the error in the intercept of the V_{drift} equation (which is measured each time, so there is no contribution from reproducibility). Finding the relative error of the system by dividing through by the sample voltage reduces Eq. (3.2) to

$$\frac{\Delta V_{sample}}{V_{sample}} = \frac{\Delta CF}{CF} + \frac{\Delta V_{probe}}{V_{probe}} + \frac{\Delta V_{offset}}{V_{probe}}. \quad (3.13)$$

Since the error of the probe is controlled by the DAQ card, $\Delta V_{offset} \approx \Delta V_{probe}$:

$$\frac{\Delta V_{sample}}{V_{sample}} \approx \frac{\Delta CF}{CF} + 2 \frac{\Delta V_{probe}}{V_{probe}}. \quad (3.14)$$

Figure 3.16 shows the relative error in the system as a function of sample voltage. For sample voltages over ~ 400 V, the relative error is controlled by the relative error of the calibration factor or 0.05% for the large probe, or 0.8% for the small probe.

3.6. Radial Resolution

The maximum possible radial resolution is determined by the size of the electrode used for the measurement (large electrode 7 mm, small electrode 3 mm). The minimum radial resolution that can be achieved by this instrument is governed not by the resolution of the stepper motor (0.02 mm), but by the voltage resolution of a measurement. As the SVP is swept across the samples surface, there comes a point where the spatial steps are small enough there is no discernible difference in voltage measurements. This relationship holds if the requirements found in Section 3.5 are valid, thus defining the spatial resolution by Eq. (3.15),

$$\frac{\Delta A_{elec}}{A_{elec}} = \frac{\Delta V}{V}, \quad (3.15)$$

where $\Delta A/A$ is the relative resolution of the probe and $\Delta V/V$ is the relative voltage resolution of the electrodes as found in Section 3.5. Since the electrodes relative voltage resolution is dependent on the sample voltage, as seen in FIG. 3.16, the radial resolution will also be sample voltage dependent. Solving for ΔA will lead to the minimum radial resolution of the instrumentation shown in FIG. 3.17 (for large voltages, 0.08 mm on the large probe, and 0.14 mm on the small probe). The maximum and minimum radial resolutions define a range of possible resolutions, and various tests similar to the one shown below will narrow this range.

A simple test was setup to sweep the large electrode across a charged conductor. The conductor was charged to 1000 V and measurements were taken every 100 steps (1.3 mm). A convolution of the circular 7 mm electrode, estimated as a circular step function, over this 10 mm charged conductor (also estimated as a circular step function) provides an estimation of the voltage profile, which should be read by the SVP. Figure 3.18 shows the agreement of this profile

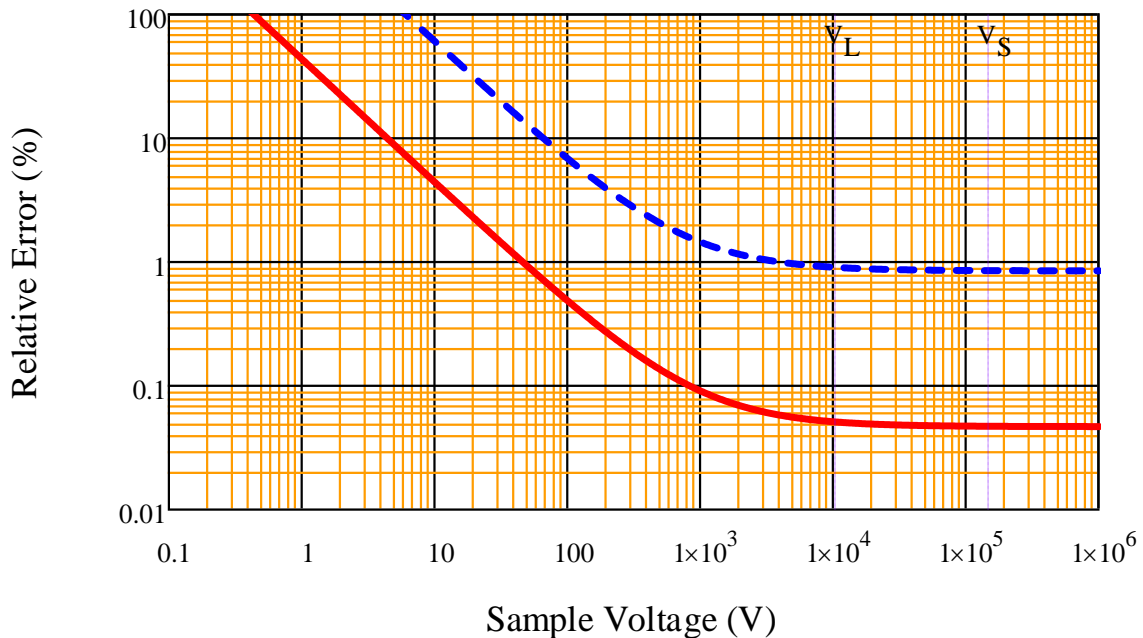


FIG. 3.16. Graph of relative error as a function of surface voltage. Large electrode (Red) and the small electrode (Blue), vertical red lines show the voltage limits of the large probe where the vertical blue lines show the voltage limit of the small probe.

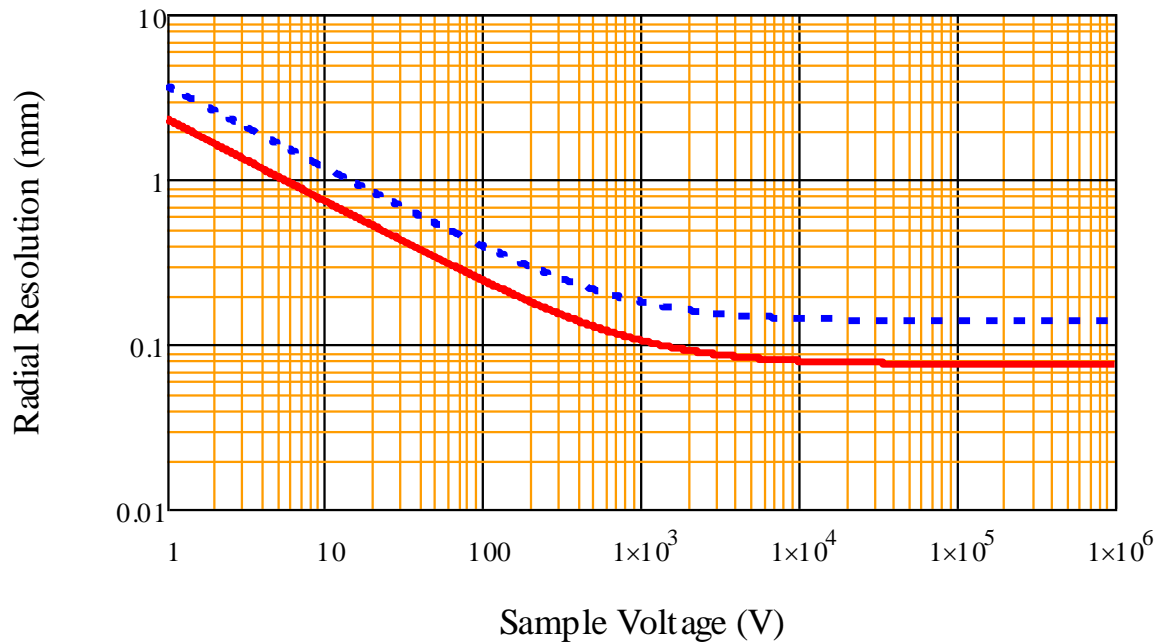


FIG. 3.17. Minimum radial resolution based on sample voltage. Large electrode (Red) and the small electrode (Blue).

(red) with the measured results (blue). From this information it can be estimated the radial resolution is at most half the diameter of the electrode (3.5 mm for the large electrode, 1.5 mm for the small electrode). Without further tests, this is the best resolution that can be predicted. Detailed test should be completed exploring smaller conductor sizes, as well as decreasing the step size for each measurement. A useful test can be made with a 3 cm dia-biased electrode surrounded by a grounded electrode. This configuration would provide a radial voltage step profile. Measurement of the width of the voltage step would provide a direct measurement of the radial spatial resolution of the SVP.

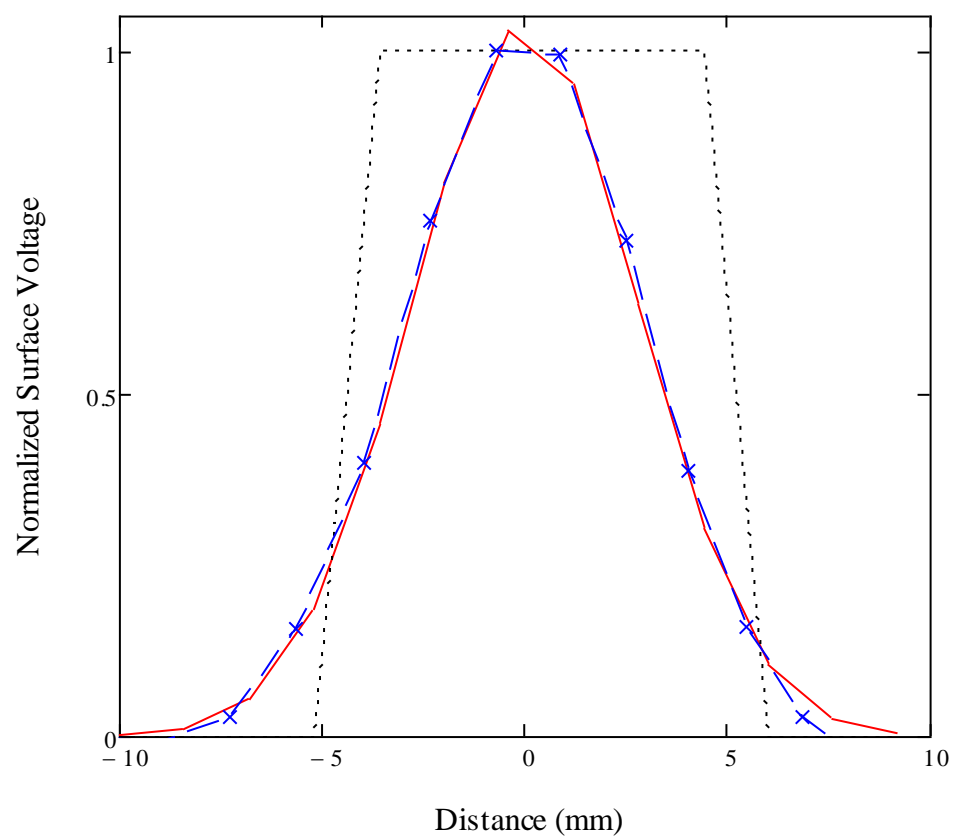


FIG. 3.18. Comparison of expected profile measurements (red) and data (blue).

CHAPTER 4

APPLICATIONS OF INSTRUMENT

This chapter reports on three types of measurements of two common spacecraft insulators, LDPE and Kapton HNTM. The measurements are intended to validate the operation and calibration of the SVP and to test and extend the limits of its application.

These two materials typify a wide range of material properties and have been extensively studied at USU, within the spacecraft charging community, and by investigations of electron transport in highly disordered polymeric insulators. The LDPE and Kapton HNTM samples were purchased from Goodfellow and Sheldal, respectively. Samples of branched LDPE (Goodfellow, ASTM type I) of (27.4 ± 0.1) μm thickness had a density of (0.92 ± 0.01) g/cm^3 (Goodfellow Cambridge Ltd., 2006) with an estimated crystallinity of 50% (Wintle, 1999), an estimated peak fractional mass distribution of $\sim 6 \times 10^3$ amu or $\sim 2 \times 10^3$ C_2H_4 mers per chain (Peacock, 2000; Brunson, 2010), and a relative dielectric constant of 2.26 (Goodfellow Cambridge Ltd., 2006). Samples of Kapton HNTM (Dupont, ASTM D-5213 type I) of (25.1 ± 0.2) μm thickness had a density of (1.43 ± 0.01) g/cm^3 (DuPont, 2010), and a relative dielectric constant of 3.5 (Goodfellow Cambridge Ltd., 2006). A single mer of Kapton HNTM has an atomic composition of $\text{C}_{22}\text{O}_5\text{N}_2\text{H}_{10}$ (DuPont, 2010). Material parameters are summarized in Table 4.1.

TABLE 4.1. Common material properties for tested materials.*

Material	t_s (μm) (a)	ρ (g/cm^3) (a)	ϵ_r (b)	ESD Field Strength (MV/m) (a)	$\sigma_{\text{DC}(295\text{K})}$ ($\Omega\text{-cm}$) ⁻¹ (a)	$\sigma_{\text{RIC}(295\text{K})}$ @5keV and 1 nA/cm ² ($\Omega\text{-cm}$) ⁻¹ (a)	E_1 E_2	R @5keV (μm) (a)
Kapton HN TM	25.1	1.42	3.5	~ 280	1.5×10^{-19}	6×10^{-18}	$\sim 45(\text{eV})$ (a) $\sim 1.75(\text{keV})$	0.50
LDPE	27.4	0.92	2.3	~ 270	1.4×10^{-18}	1.5×10^{-16}	$\sim 42(\text{eV})$ (b) $\sim 0.7(\text{keV})$	0.60

(a) Values measured by USU MPG. (b) Manufacturers' listed values.

*Uncertainties of values can be found in text.

The electron yields of highly insulating materials are difficult to measure (Hoffmann and Dennison, 2010); however, values of the total, secondary, and backscattered electron yields have been measured for both Kapton HNTM and LDPE over limited incident electron energy ranges. For Kapton HNTM, the yields measured by the USU MPG cover an energy range of 0.2 to 5 keV and are shown in FIG. 4.1 (Hoffmann, 2010). For the 5 keV incident beam energy used to acquire the data described in this chapter, the total electron yield of Kapton HNTM is ~ 0.32 electrons per electron. The first and second crossover energies at which the total yield is unity are approximately 42 eV and 900 eV, respectively. These values of the total yield at 5 keV and the secondary crossover energies are comparable to, but somewhat higher than, those measured by (Willis and Skinner, 1973) and predicted by Monte Carlo simulation by Yasuda (Yasuda *et al.*, 2004). The maximum total yield of ~ 2.2 electrons per electron at ~ 200 eV in FIG. 4.1 is close to

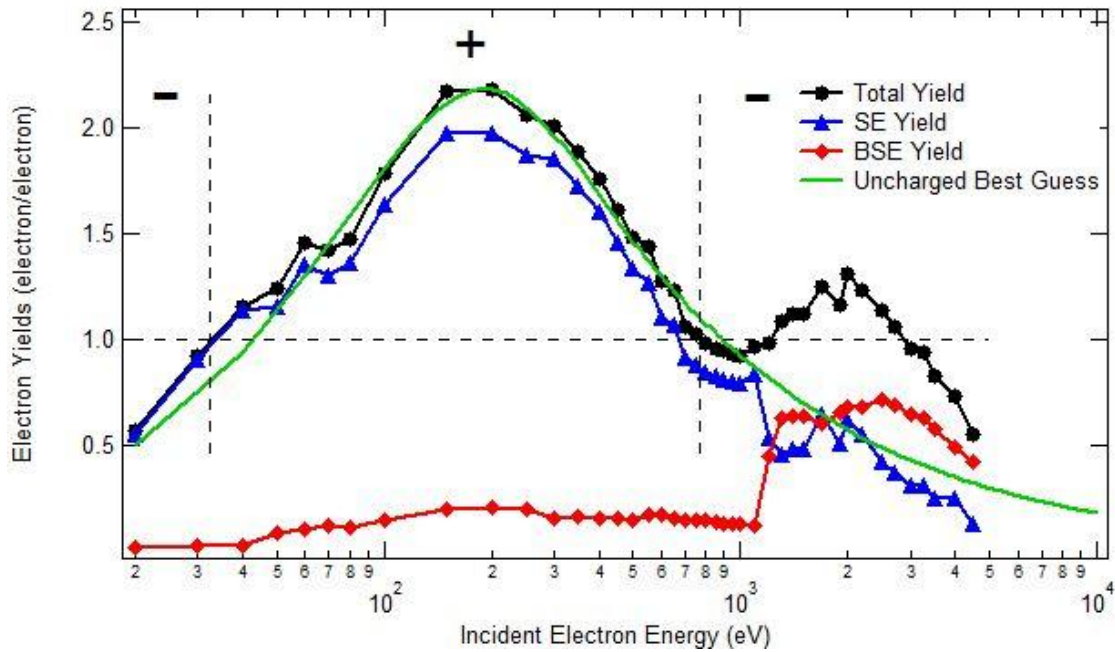


FIG. 4.1. Composite total yield curve of Kapton HNTM. Data points show measured yields for charged samples. Green curve is the yield calculated of an uncharged sample. After Hoffmann (2010).

that measured by (Willis and Skinner, 1973). The yields of LDPE have been measured in the range of 5000 V to 35000 V by (Song *et al.*, 1997) and 200 eV to 2500 eV by Matskevich (Matskevich, 1959), as shown in FIG. 4.2. At the 5 keV incident energy for the tests performed in this chapter, the total yield is ~ 0.50 electrons per electron. From these data, the first and second crossover energies are estimated to be in the range of ~ 45 eV and ~ 1750 eV, respectively, with a maximum total yield of 2.7 electrons per electron at ~ 250 eV.

Incident electrons lose energy through a series of small energy inelastic collisions as they penetrate into a material. The mean penetration depth at which incident electrons come to rest is referred to as the range, R . Wilson and Dennison (2010) give a detailed discussion of the energy dependence of the range in the mean Continuous Slow Down Approximation (CSDA). The ranges as a function of incident electron energy for Kapton HNTM and LDPE are shown in FIG. 4.3. At a 5 keV incident energy, the ranges for Kapton HNTM and LDPE are (0.5 ± 0.1) μm and (0.6 ± 0.1) μm , respectively.

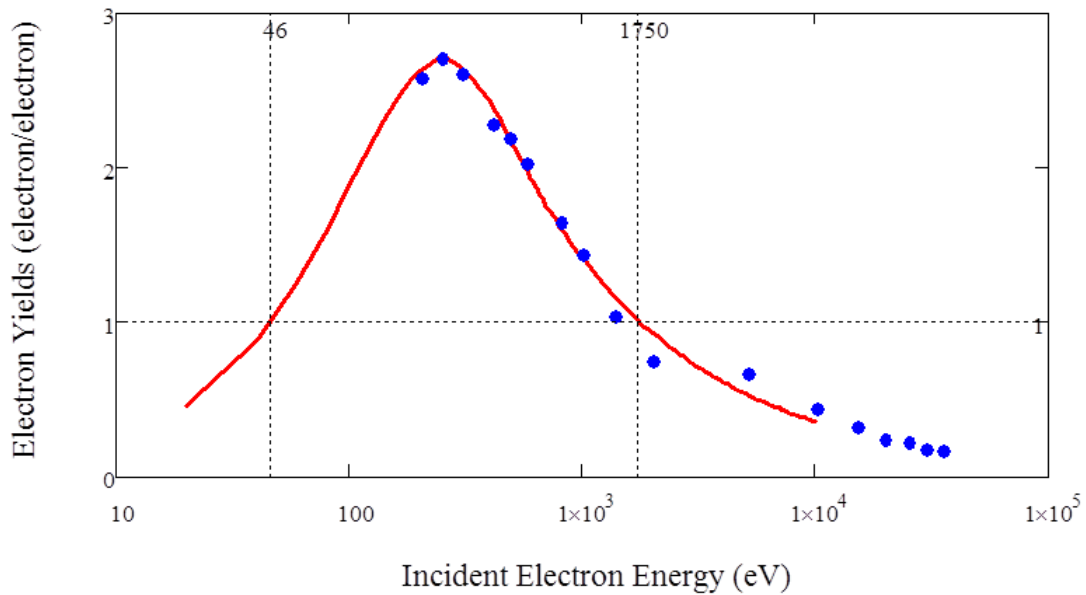


FIG. 4.2. Experimental yield curve of LDPE. Data from (Song *et al.*, 1997; Matskevich, 1959; Montanari *et al.*, 2001; Dennison *et al.*, 2009) (blue) with NASCAP 5 parameter fit (red).

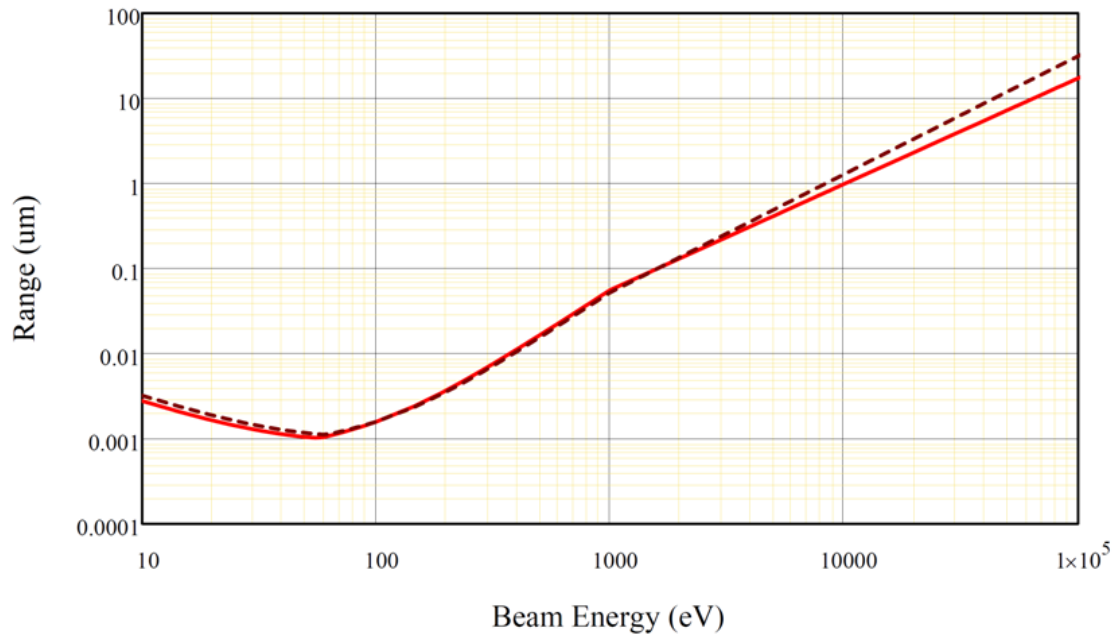


FIG. 4.3. Penetration Range of Kapton HN™ (dashed) and LDPE (solid).

Electron transport properties of Kapton HN™ and LDPE have been measured, as well. Room-temperature, dark-current conductivities were measured by the USU MPG to be $1.5 \times 10^{-19} (\Omega\text{-cm})^{-1}$ for Kapton HN™ (Dennison *et al.*, 2009) and $1.4 \times 10^{-18} (\Omega\text{-cm})^{-1}$ for LDPE (Dennison *et al.*, 2009; Brunson, 2010). The electrostatic field strengths were also measured by the USU MPG as ~ 280 MV/m for Kapton HN™ and ~ 270 MV/m for LDPE (Sim and Dennison, 2010). A list of corroborating measurements and a discussion of conduction-related properties, such as densities of trap states, energy depths of trap states, rates of carrier capture and release from trap states are included in the discussions of models used to fit the data in Sections 4.2 and 4.3. The enhanced conductivity due to energy deposition and subsequent excitation of trapped carriers into conduction states is known as radiation-induced conductivity (RIC) (Rose, 1951; Fowler, 1956). RIC is expressed as a power law of dose rate, $\sigma_{\text{RIC}}(\dot{D}) = k_{\text{RIC}}(T) \dot{D}^{\Delta(T)}$, with temperature-dependent material parameters $k_{\text{ric}}(T)$ and $\Delta(T)$ (Corbridge *et al.*, 2008). Values of RIC as a function of dose rates of 10^{-2} rad/s to 10^2 rad/s over temperatures from ~ 100 K to ~ 360 K for both

Kapton ETM and LDPE were measured from studies done by the USU MPG at Idaho Accelerator Center. For Kapton ETM (very similar to Kapton HNTM used for studies in this thesis) at room temperature k_{ric} is $(6\pm2)\times10^{-18}$ (rad/s· Ω -cm)⁻¹ and $\Delta=1.00\pm0.01$ (Corbridge *et al.*, 2008). For LDPE at room temperature, K_{ric} is $(1.5\pm0.5)\times10^{-16}$ (rad/s· Ω -cm)⁻¹ and $\Delta=0.85\pm0.05$ (Corbridge *et al.*, 2008). These results are similar to other studies as reviewed in the cited references (Rose, 1951; Fowler, 1956).

All samples were chemically cleaned with methanol prior to testing in the vacuum chamber. Typically, samples are baked out at elevated temperatures (120 ± 2 °C for Kapton HNTM and 65 ± 1 °C for LDPE) under $\sim10^{-4}$ Pa vacuum for 48 hr to eliminate absorbed water and volatile contaminants. Sample's condition in this manner had a measured outgassing rate of $<0.05\%$ mass loss/day at the end of bake out, as determined with a modified ASTM 3740 test procedure (Brunson, 2010). By contrast, the specific samples used for the tests described in this chapter were not baked out in this manner. Instead, the samples were held at pressures of $\sim10^{-8}$ Torr for ~7 days, effectively pumping off most of the water that may have been absorbed or adsorbed by the materials.

Three measurements were made that investigate the charge accumulation in materials, how a charge in a sample decays over time, and the radial distribution and diffusion of charge across the face of the samples. The results obtained in these studies, as described in the subsequent sections, offer proof of concept and validation of the new instrumentation, as well as extending the investigations within the USU MPG. In each of these three experiments, the sample was charged using pulsed beams from the Staib electron gun. Surface voltages were measured between pulses using the SVP to monitor charge build up and decay occurring during the charging procedures. For all experiments described in this chapter, the materials were initially charged with $\sim(10\pm2)$ s pulses, with a beam energy of (5.000 ± 0.005) keV and a flux density of (1.1 ± 0.1) nA/cm². The incident beam energy was selected to be well above the second crossover

energies of both Kapton HN™ and LDPE with a yield ≤ 1 , as shown in FIG. 4.1 and FIG. 4.2.

This ensured that all the samples charged to large negative potentials.

4.1. Collection and Processing of Data

4.1.1. Methods of Collecting Data

The LABView™ program discussed in Section 2.4.1 was used for all data collection in this chapter. This section defines the parameters for the Flipper Simple5.llb LABView™ VI, which was used to collect the majority of data for all three experiments performed.

To measure charge accumulation, the Long Decay Loop in the LABView™ program was used (see Section 2.4.1.). An automated charge-up option is available for very short pulses (< 0.5 s) or long-term charge-up collection (> 7200 s), but the manual charge-up option was used for these tests to provide the experimenter with more control of the amount of charge injected. The experiment parameters were chosen so the beam was manually turned on and off while the witness plate was grounded. This reduced the drift effects from electrical noise generated by the electron beam. The timing sequence shown in FIG. 4.4 allowed for ~ 10 s of the 5 keV 1.1 nA/cm² electron source to irradiate the samples. A delay time between sets of measurements was set to 12 s to allow time for the electrical noise to dissipate for ~ 1 s before and after the charge injection occurred. For the Kapton HN™ data, charge-up times were increased throughout the run. The beam on time was changed from 10 s to 30 s at approximately 340 s of injected charge and then again from 30 s to 120 s at approximately 890 s of injected charge. The tests were conducted until it appeared to the experimenter that the sample surface voltage had reach equilibrium. 10 s of data were collected for each ground measurement, as well as the voltage measurement (see FIG. 4.4). These data were used to allow for steady ground drift measurements and, if necessary, to get detailed short-term charging measurements; however, as discussed in Section 4.1.2, these charging data were largely ignored.

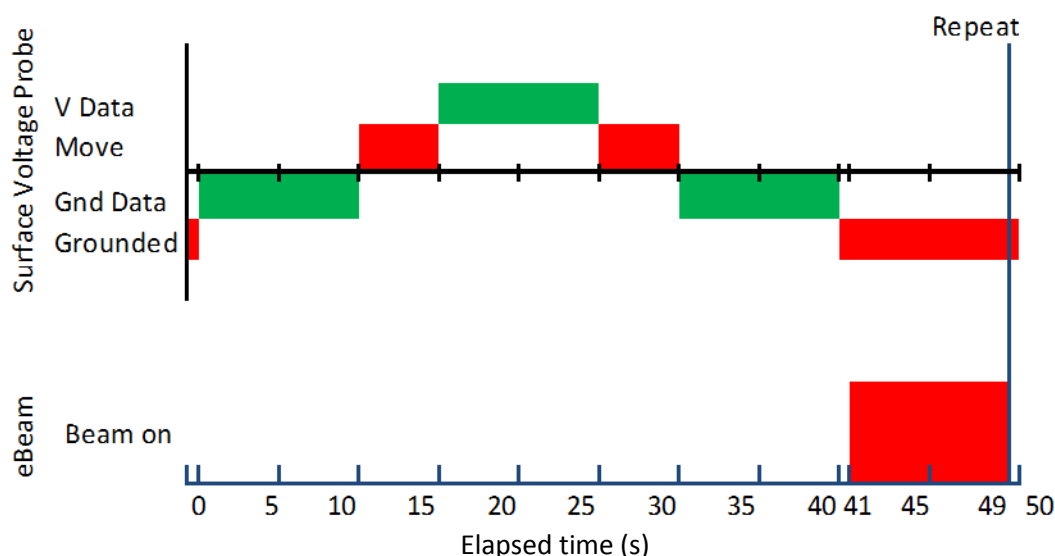


FIG. 4.4. Timing of a standard charge accumulation/dissipation run. Grounded times varied depending on the beam on time. For dissipation runs, the electron source was not used. Green represents time at which data are being collected.

The LABView™ Long Decay Loop with the same settings was also used to monitor the surface voltage as charge bled through the sample. The difference between the charge-up and voltage-decay procedures consisted of simply setting the same control program to manual charge, but never manually turning the beam on. The test was setup to watch the voltage decay over a 24 hr period, with a wait time that governed time between surface voltage measurements set to ~2 min. A second test also looked at the feasibility of using the surface voltage apparatus in a manner similar to that used for the charged storage chamber, where simultaneous tests on multiple samples could be performed in the chamber (Dennison *et al.*, 2003a). The SVP and collector were moved off the sample to perform simultaneous tests on different materials on the sample stage. When those tests were concluded, the SVP and collector were returned to the original sample and normal data collection was continued.

The lateral charge dissipation was measured via the Sweep Loop of the LABView™ program (see Section 3.6). The sample surface voltage was measured at 11 points along the surface as the charge decayed. The sample was charged with two 30 s pulses of a 1.1 nA/cm^2 , 5

keV beam. The large electrode was swept across the surface of the sample, taking measurements at ~1.5 mm increments (100 motor steps). Data were taken over a 24 hr period at 2 min intervals as the voltage decayed.

4.1.2. Data Processing

After the data runs were complete, the data were processed using the programming capability available in MathCAD. Each of the loops completed by the LABView™ automated data acquisition program had 30 data points (20 over a common ground and then 10 over the charged sample). The first programmatic adjustments were done to correct the data for ground drift. The MathCAD function, Slope, was used to determine the slope of the initial 10 data points collected over the grounded surface. This slope was used with the recorded time to correct each block of 30 data points, using a linear time correction. Equation (4.1) was used, which is similar to Eq. (3.9), described in Chapter 3, with the omission of the voltage drift.

$$V_{corrected_i} = V_{probe_i} - Slope \left(V_{overground_{1..10}}, t_{overground_{1..10}} \right) (t_i - t_1) - V_{probe_1}. \quad (4.1)$$

The second set of corrected ground drifts were checked to ensure that no oddities appeared during the data correction. This corrected data was then parsed out, so only the corrected data over the charged sample were available. From this point on, the voltage drift, as discussed in Section 3.4, was neglected; over short periods of time, this is a valid assumption. To avoid any inherited error due to not correcting for voltage drift only, the first data point over the sample from each loop was used. These additional data were left out at the time of analysis, because there was not a complete understanding of the complexities and the repeatability of the voltage drift. With a better understanding garnered from the more detailed calibration and the follow-up work done with the SVP, Wilson, Dekany, and Dennison have added the details of the voltage drift into the LABView™ VI, thus automating the data processing to be completed on the fly.

The lateral charge dissipation data were processed in a similar manner to the charge accumulation and charge decay data. The differences came in the amount of data points collected. For the lateral charge dissipation, five ground measurements were taken on either side of the 16 profile measurements for a total of 26 data points per sweep. The first five ground measurements were used to find the ground drift slope and adjust all the data using Eq. (4.1). Again voltage drift was neglected, but not for the same reasons outlined in the accumulation/decay results. Voltage drift was neglected for these measurements due to the complexities inherited by a dynamic voltage drift caused by a radial voltage profile. As the probe moved closer to the center of charge injection, the voltage drift would inherently change. Initial measurements showed the error caused by not correcting for the drift; but, this was shortly washed out by a floating conductor, which is discussed later in this chapter.

4.2. Charge Accumulation and Electron-Induced Electrostatic Discharge

This section develops a simple, but versatile, model for 1D currents and surface voltage as a function of time for parallel plate geometry experiments. The model allows for charge injection by a surface electrode or by surface, nonpenetrating or penetrating incident radiation. The injection currents can be continuous, pulsed, or periodic. Seven different types of conduction and displacement current densities are considered, each with specific time dependencies for HDIM. The basic voltage model is adapted to successively more realistic (and complex) charge dissipation models: (i) no dissipation, (ii) time-independent conductivity, (iii) dissipation with time-dependant diffusion and dissipation currents, and (iv) dissipation with additional displacement currents resulting from the evolution of the spatial charge distribution. Assumptions and approximations for the general case and for the specific experiments analyzed in this thesis are carefully identified and justified. The final outcomes for this section are time-dependant models of surface voltage and discharge currents for electron beam charge and discharge experiments.

4.2.1. Basic Model and Assumptions

Consider a simple macroscopic model for the time dependence of the surface voltage of an insulating material subject to incident charge flux. Assume a simple dielectric slab or parallel plate capacitor geometry with a dielectric material of thickness, D , above a grounded rear electrode, as shown in FIG. 4.5. Assume the lateral extent of the layers is much larger than D , so edge effects and fringing fields can be neglected. This leads to a 1D model of electric transport.

The model developed below is generalized so it can take into account the twelve experimental configurations identified by Sim (2012) for either continuous, pulsed, or periodic charge injection for injection either via a second upper electrode or by an electron beam. For electron beam injection, a charge beam of uniform current density, $J_o(t)$, is normally incident on the upper surface. Charge carriers, assumed to be only electrons (Sim, 2012), are injected at a depth $z=R \geq 0$ below the upper surface of the dielectric. The injected charge is initially modeled as a plane of charge at a fixed depth, with areal charge density Σ . Sim (2012) enumerates four types of charge injection based on the initial spatial distribution and source of the charge:

- (i) Charge injected by a surface electrode at $z=0$ with surface potential $V_{bias}(z=0)$.
- (ii) Beam charge injected as surface charge deposited at depth $z = R \gtrsim 0$.
- (iii) Beam charge injected as nonpenetrating radiation with charge and energy deposited in a depth range $0 < R < D$.
- (iv) Beam charge injected as penetrating radiation with a penetration depth $R > D$ that does not deposit charge in the dielectric, but deposits energy throughout the material.

The surface voltage probe configuration considered in this thesis uses pulsed non-penetrating electron beam injection with no bias electrode injection (Sim, 2012). The USU charge storage chamber is quite similar, using a pulsed low-energy electron beam that deposits charge on the floating upper surface with no bias electrode injection (Swaminathan, 2004). The USU RIC chamber uses a combination of charge injected by a biased surface electrode with

simultaneous injection by a pulsed penetrating electron beam (Gillespie, 2012). The USU constant voltage chamber (Brunson, 2010) and electrostatic discharge chamber (Sim *et al.*, 2010) configurations inject a continuous charge via a biased surface electrode with no electron beam injection (Sim, 2012).

The general model shown in FIG. 4.5 allows for three charge layers:

- (i) The first charge layer is in the grounded electrode, fixed at $z=D$.
- (ii) The second charge layer is in the upper surface fixed at $z=0$, which can either be floating (for electron beam injection) or held at a fixed potential V_{bias} (for electrode injection).
- (iii) The third charge layer (only for electron beam injection) with a centroid of charge at $z_d(t; E_b)$ that is initially injected at a depth $R(E_b)$, which depends on the injection beam energy E_b , but may move with time.

A fourth virtual charge layer on an external electrode at $z_{ext} < 0$ is used to set the external electric field in the region $0 < z < z_{ext}$.

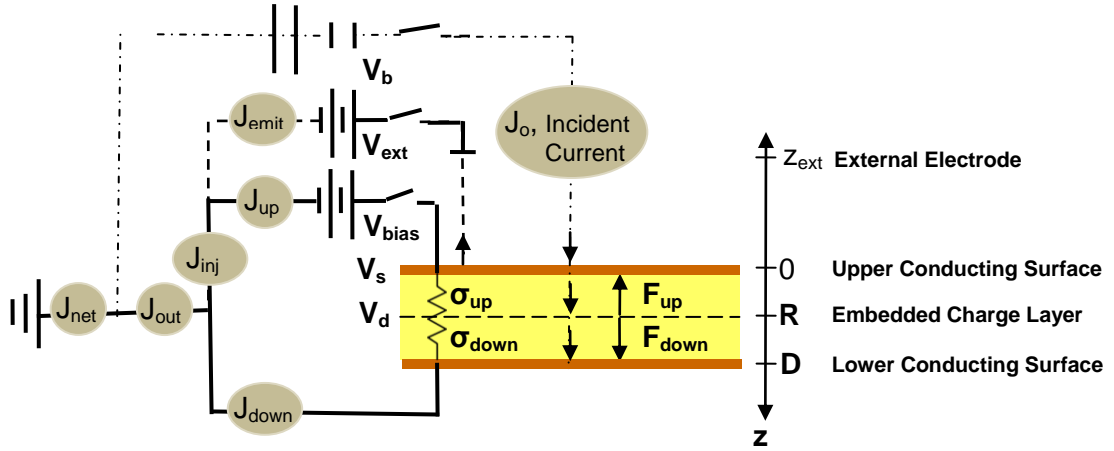


FIG. 4.5. Basic slab geometry of charge transport for an incident electron beam. Electron beam is incident on a dielectric slab with a grounded lower surface and grounded or floating upper surface. R —range or penetration depth; D —sample thickness; F_{up} and F_{down} —electric fields above and below embedded charge layer; J —current densities including injected beam current density, J_{in} , emitted current density, J_{emit} , current density through from upper surface, J_{up} , current density through lower grounded surface, J_{down} , injection current density, J_{inj} , and net total current density out of the dielectric, $J_{out}=J_{emit}+J_{up}+J_{down}$; V —voltages including deposited-layer voltage, V_d , surface voltage, V_s , bias voltage, V_{bias} , external electrode voltage, V_{ext} , and electron beam voltage, V_b .

Begin by considering the uniform electric field produced by a single charge layer (see FIG. 4.6 a) that extends in both directions normal to the 2D charge plane with a magnitude $\Sigma/2\epsilon_o\epsilon_r$ set solely by the charge density in the layer, Σ , and the permittivity of the material $\epsilon_o\epsilon_r$. A charge double layer is formed by two adjacent charge layers of equal and opposite charge density held at a separation L (see FIG. 4.6 b). Between the charge layers, the superposition of the fields from the two layers add constructively, yielding a uniform electric field $\vec{F} = [\Sigma/\epsilon_o\epsilon_r] \hat{z}$ and a potential difference between the layers of $\Delta V = -F \cdot L = -\Sigma L/\epsilon_o\epsilon_r$. Exterior to the charge double layer, superposition of the fields is destructive, yielding a zero net electric field. By setting the magnitudes of charge on these layers in this geometry and the position of the embedded charge layer, we can fully model a spatially constant field and linearly varying potential within the double layer at any depth inside the dielectric.

To model surface electrode charge injection, an electrode double layer is formed when charge density Σ_{bias} is added to the upper electrode at $z=0$ (characterized by a fixed potential $V_{bias} = -\Sigma_{bias} \cdot D/\epsilon_o\epsilon_r$). A charge layer of equal and opposite charge is induced on the grounded lower electrode, forming the double layer, which produces a field $\vec{F}_{bias} = -[V_{bias}/D] \hat{z}$ inside the dielectric for $0 < z < D$. Note, for a negative V_{bias} on the upper electrode, the field is in the $+\hat{z}$ direction.

In a similar manner, to model an electron beam injection layer, two double layers are formed, one between the embedded layer at depth R and the grounded lower electrode and a second between the embedded layer and (grounded or floating) upper electrode surface. The lower double layer produces a field $\vec{F}_{d\ down} = [\Sigma_d/\epsilon_o\epsilon_r] \hat{z}$ and a potential difference $V_{d\ down} = -F_{d\ down} \cdot (D-R) = -\Sigma_d(D-R)/\epsilon_o\epsilon_r$ from the embedded layer to the grounded lower electrode. The upper double layer produces a field $\vec{F}_{d\ up} = -[(V_d - V_{ext})/(z_d(t) - z_{ext})] \hat{z}$ in the opposite direction

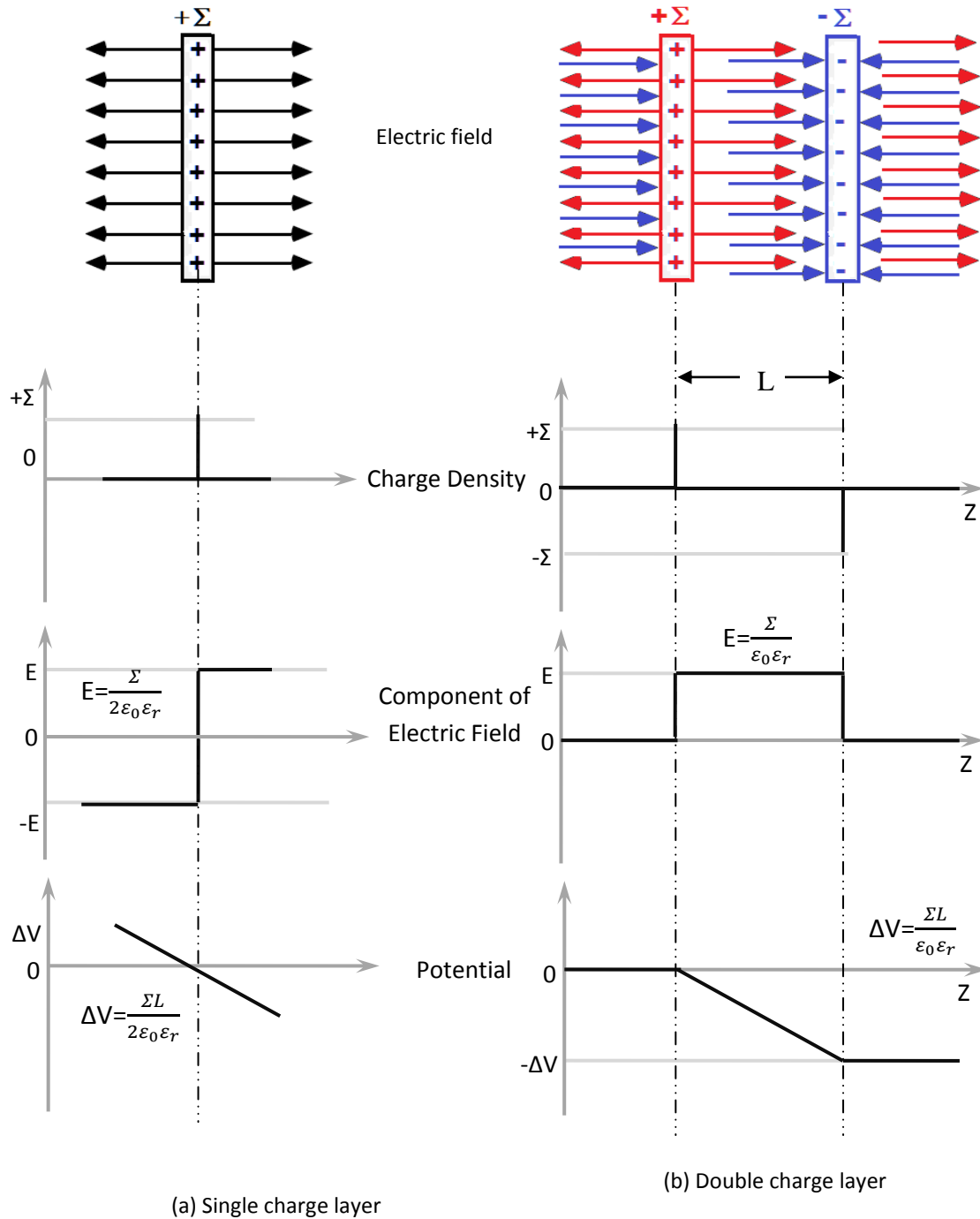


FIG. 4.6. Models of charge layer. (a) Single charge layer. (b) Double charge layer. From top to bottom, the figures show (i) the charge layer(s) and associated electric fields, (ii) the charge density as a function of depth, z , (iii) the magnitude of the electric field as a function of depth, and (iv) the change in electric potential as a function of depth.

and a potential difference between the virtual electrode at $z_{ext}=0$ held at potential V_{ext} and the embedded layer held at $V_d = -\Sigma_d[D - z_d(t)]/\epsilon_0\epsilon_r$. The centroid of the charge distribution is at $z_d(t)$, where $F(t, z_d)=0$. It is initially at the penetration depth $R(E_b)$. Note for a floating upper surface, the virtual electrode effectively retreats to $z_{ext} \rightarrow -\infty$ and $F_{d up} \rightarrow 0$.

Taken together, we find expressions for the electric field and electric potential everywhere inside the dielectric:

$$\vec{F}(z, t) = \begin{cases} 0 & ; z \leq z_{ext} \\ \vec{F}_{ext}(z, t) = \left[-\frac{V_{ext}}{z_d(t) - z_{ext}} \right] \hat{z} & ; 0 < z < z_{ext} \\ \vec{F}_{up}(z, t) = \left[-\frac{V_{bias}(t)}{D} - \frac{\Sigma_d(t)}{\epsilon_0\epsilon_r} - \frac{V_{ext}}{z_d(t) - z_{ext}} \right] \hat{z} & ; 0 \leq z < z_d(t) \\ \vec{F}_{down}(z, t) = \left[-\frac{V_{bias}(t)}{D} + \frac{\Sigma_d(t)}{\epsilon_0\epsilon_r} \right] \hat{z} & ; z_d(t) \leq z \leq D \\ 0 & ; z > D \end{cases} \quad (4.2)$$

and

$$V(z, t) = \begin{cases} V_{bias}(t) + V_{ext} & ; z \leq z_{ext} \\ V_{bias}(t) + V_{ext} - \left[V_{ext} + \frac{\Sigma_d(t)}{\epsilon_0\epsilon_r} \right] \left[\frac{(z - z_{ext})}{z_d(t) - z_{ext}} \right] & ; 0 < z < z_{ext} \\ V_s(t) = V_{bias}(t) + V_{ext} \left[\frac{D}{z_d(t) - z_{ext}} \right] + \frac{\Sigma_d(t)}{\epsilon_0\epsilon_r} \left[\frac{z_{ext}}{z_d(t) - z_{ext}} \right] & ; z = 0 \\ V_{bias}(t) \left[\frac{(D - z)}{D} \right] + V_{ext} - \left[V_{ext} + \frac{\Sigma_d(t)}{\epsilon_0\epsilon_r} \right] \left[\frac{(z - z_{ext})}{z_d(t) - z_{ext}} \right] & ; 0 \leq z < z_d(t) \\ V_{bias}(t) \left[\frac{(D - z_d(t))}{D} \right] - \frac{\Sigma_d(t)}{\epsilon_0\epsilon_r} [D - z_d(t)] & ; z = z_d(t) \\ V_{bias}(t) \left[\frac{(D - z)}{D} \right] - \frac{\Sigma_d(t)}{\epsilon_0\epsilon_r} [D - z] & ; z_d(t) \leq z \leq D \\ 0 & ; z > D \end{cases} \quad (4.3)$$

In this slab geometry from Gauss' Law, the surface voltage, $V_s(t)$, in terms of a deposited charge areal density, $\Sigma_d(z, t)$, is

$$V_s(t) = V_{bias}(t) + V_{ext} \left[\frac{D}{z_d(t) - z_{ext}} \right] + \frac{1}{\epsilon_0\epsilon_r} \left[\frac{z_{ext}}{z_d(t) - z_{ext}} \right] \int_0^D \Sigma_d(z, t) dz. \quad (4.4)$$

Alternately Eq. 4.4 can be written for an injected charge carrier (or space charge) density per unit volume, $n_t(t) = \Sigma_d(t)/q_e R$ for a beam that uniformly deposits charge over a depth $0 < z < R$, as

$$V_s(t) = V_{bias}(t) + V_{ext} \left[\frac{D}{z_d(t) - z_{ext}} \right] + \frac{q_e R}{\epsilon_0\epsilon_r} \left[\frac{z_{ext}}{z_d(t) - z_{ext}} \right] \int_0^D n_t(z, t) dz. \quad (4.5)$$

This model based on double layers, with a time varying position for the embedded layer, is essentially the dynamic double layer model (DDLm) proposed by Melchinger and Hofmann (1995), Cazaux (1999, 2003) and Meyza *et al.* (2003) [and employed and extended by Thomson (2001) and Hoffmann (2010) of the USU MPG] to describe the charge dependence of electron emission in HDIM in terms of charge distributions in the region $0 < z < R$. The DDLm adds two additional charge layers: one to compensate for secondary electron emission of magnitude $\frac{-\Sigma_d(t)}{\epsilon_0 \epsilon_r} [D - z_d(t)][1 - Y]$ at $z=0$, and another to account for secondary electrons reattracted to a positively charged dielectric of magnitude $\frac{+\Sigma_d(t)}{\epsilon_0 \epsilon_r} [D - z_d(t)]$ at a depth $\lambda_{SE}/2$, where λ_{SE} is equal to the average inelastic mean-free path of the secondary electrons. Refer to Hoffmann (2010) for further details.

The assumptions leading to the simplest model for this charge are:

1. A parallel plate geometry with a dielectric material above a grounded electrode, where the lateral extent of the layers is much larger than the thickness so edge effects and fringing fields can be neglected. This leads to a 1D model of electric transport.
2. The incident (or injected) charge carriers are electrons, with charge per electron $q_e < 0$. All charge transport mechanisms considered are only for electron transport. More complex models, not addressed here, allow for mobile recombination sites (holes) and for ionic conduction. Refer to Chapter 2 in Sim (2012) for a detailed discussion of this assumption.
3. The magnitude of the injected current density is approximated as the time-averaged incident beam current density, \bar{J}_0 , measured over the full deposited time; that is,

$$\bar{J}_0 \equiv \frac{\int_0^{t_{dep}} J_{inj}(t) dt}{\int_0^{t_{dep}} dt} \approx J_0 \frac{t_{on}}{t_{dep}} = J_0 \frac{N_{pulse} t_{pulse}}{t_{dep}} \quad (4.6)$$

for any time-dependant injection current, $J_{inj}(t)$, including pulsed and periodic signals. For the measurements in this thesis, this approximation assumes a pulsed, time-dependent

incident beam current density, $J_{inj}(t)$, extending for a full deposition time period t_{dep} , and comprised of a constant beam current, J_o , on for a time, $t_{on} \equiv N_{pulse}t_{pulse}$ for N_{pulse} pulses each of duration t_{pulse} . This is a reasonable approximation as long as the time the beam is off after each pulse, $\frac{t_{dep}}{N_{pulse}} - t_{pulse}$, is small compared to times for significant charge migration and dissipation or for changes in conductivity (*e.g.*, changes in RIC). This assumption is addressed for the Kapton HNTM charging data in Sec. 4.3.1, where t_{on} and t_{off} are not constant throughout the experiment. Refer to additional comments on RIC in Section 4.4 for further discussions. Note, when assumptions 4, 5, 6, or 7 are relaxed, assumption 3 must be reconsidered.

4. All charge from the beam is initially deposited at single penetration depth or range, $R(E_b)$, that depends on the incident beam energy, E_b , through the Bethe approximation for non-penetrating radiation (Bethe and Heitler, 1934; Hoffmann, 2010); that is,

$$\Sigma(z, t) = \begin{cases} \bar{J}_o t \delta[z - R(E_b)] & ; J_{inj}(t) = \bar{J}_o \text{ with assumption 3.} \\ \int_0^t J_{inj}(t') dt' \delta[z - R(E_b)] & ; J_{inj}(t) \neq \bar{J}_o \text{ without assumption 3.} \end{cases} \quad (4.7)$$

In fact, the range, shown for LDPE and Kapton HNTM in FIG. 4.3, will change as the landing energy of the incident radiation, $E_b - q_e V_s(t)$, decreases as charge accumulates. This approximation will modify the initial charge spatial distribution in the RIC region, $0 < z < R(E_b)$, but will not affect the equilibrium surface voltage. This point is discussed further in Section 4.3.2 below for Kapton HNTM charge decay data. The energy dependence of the range is discussed by Wilson and Dennison (2010).

5. Charge deposited in the region $0 < x < R$ quickly redistributes to a uniform volume charge distribution

$$n_t(z, t) = \begin{cases} \frac{\bar{J}_o t}{q_e R(E_b)} \Theta[z - R(E_b)] = \bar{n}_t(t) \Theta[z - R(E_b)]; \\ \quad \text{with } \bar{n}_t(t) \equiv \frac{\bar{J}_o t}{q_e R(E_b)} \\ \quad \text{for } J_{inj}(t) = \bar{J}_o \text{ with assumption 3,} \\ \quad \text{and with } R = R(E_b) \text{ with assumption 4.} \\ \frac{1}{q_e R(E_b)} \int_0^t J_{inj}(t') dt' \Theta[z - R(E_b)] = \bar{n}_t(t) \Theta[z - R(E_b)]; \\ \quad \text{with } \bar{n}_t(t) \equiv \frac{1}{q_e R(E_b)} \int_0^t J_{inj}(t') dt' \\ \quad \text{for } J_{inj}(t) \neq \bar{J}_o \text{ without assumption 3,} \\ \quad \text{but with } R = R(E_b) \text{ with assumption 4.} \\ \int_0^t \frac{J_{inj}(t')}{q_e R(E_b - q_e V_s(t'))} \Theta[z - R(E_b - q_e V_s(t'))] dt' \\ \quad \text{for } J_{inj}(t) \neq \bar{J}_o \text{ without assumption 3} \\ \quad \text{and } R = R[E_b - q_e V_s(t)] \text{ without assumption 4.} \end{cases} \quad (4.8)$$

$\Theta(z)$ is a Heavyside step function. Note, after such a redistribution, the center of charge $z_d(t)$ is at $\frac{1}{2}R(E_b)$ not $R(E_b)$.

6. There is no electron emission; that is, the total electron yield, $Y=0$. The effects of an energy-dependant total electron emission will be incorporated below through a model for the electron beam injection potential, first as a time-independent yield, $Y(E_b)$, and then as a time-dependant yield, $Y[E_b - q_e V_s(t; E_b)]$. For a time-dependant yield, assumptions 3, 4 and 5 must be reconsidered. Cornet *et al.* (2008) considers the effects of electron emission on charge accumulation further. Conversely, Hofmann (2010) and Thomson (2001) consider the effects of charging on electron emission.
7. There is no charge dissipation. In this approximation, the dielectric acts as a perfect charge integrator. Successive improvements to this approximation will consider (i) simple time-independent Ohmic conduction with constant conductivity σ_o , and more accurate (and more complex) time- and field-dependant charge transport models more appropriate for highly disordered insulating materials, with conductivity $\sigma(t, F)$, that incorporate (ii) displacement current densities from static charge distributions and (iii) displacement current densities from evolving charge distributions.

As noted, assumptions 3, 4, 5, 6 and 7 will be relaxed during subsequent discussions and data analysis in this chapter.

Taken together, using Eqs. 4.6, 4.7 and 4.8 in Eq. 4.3, these approximations lead to an expression for the surface voltage as a function of time,

$$V_s(t) \begin{cases} = \frac{\bar{J}_o t}{\epsilon_o \epsilon_r} \left[D \left(1 - \frac{R(E_b)}{D} \right) \right] = \frac{\Sigma(t; E_b)}{\epsilon_o \epsilon_r} \left[D \left(1 - \frac{R(E_b)}{D} \right) \right] = \frac{q_e \bar{n}_t(t) R(E_b)}{\epsilon_o \epsilon_r} \left[D \left(1 - \frac{R(E_b)}{2 D} \right) \right] \\ \equiv V_{inj}^{ne} \left(\frac{t}{\tau_o} \right) \end{cases} \quad (\text{no emission, no dissipation}), \quad (4.9)$$

where we have set the electrode injection voltage $V_{elec} \rightarrow 0$ and the external field voltage $V_{ext} \rightarrow 0$.

We have used the definition for a conductivity time constant, $\tau_o \equiv \frac{\epsilon_o \epsilon_r}{\sigma_o}$. Note in Eq. 4.9, all depth

and energy dependencies are accounted for in the range and all the time dependence is accounted for in the injection current (*i.e.*, in the explicit linear term, t , or the charge densities $\Sigma(t)$ or $\bar{n}_t(t)$).

There is no voltage dependence of any terms in Eq 4.9. This predicts a simple linear increase in surface voltage, as long as the incident beam is on.

4.2.2. Models Including Emission

To increase the accuracy of the charge accumulation model, one can include the effects of electron emission (assumption 6). Electron emission effectively reduces the electron beam incident current density by a factor of $(1-Y)$ for net charge added, where Y is the total electron yield of the material. That is, J_{in} is replaced by J_{inj} (see Fig. 4.4). The total yield depends on incident energy—or more correctly on the landing energy, $E_b - q_e V_s(t)$, for biased samples—as shown by the yield curve for Kapton HN™ FIG. 4.1 (Hoffmann, 2010) and LDPE FIG. 4.2 (Song *et al.*, 1997). As a first approximation, the voltage dependence of the total yield is neglected and the time-dependant yield $Y(t; V_s, E_b)$ is set equal to the static yield, $Y(E_b)$. Including static electron emission, Eq. 4.9 becomes

$$V_s(t) \begin{cases} = \frac{\bar{J}_o t}{\varepsilon_o \varepsilon_r} [1 - Y(E_b)] \left[D \left(1 - \frac{R(E_b)}{D} \right) \right] \\ \equiv V_{inj}^{se} \left(\frac{t}{\tau_o} \right) \end{cases} \quad (\text{static emission, no dissipation}). \quad (4.10)$$

Dynamic emission models provide models for surface voltage charging. A simple model for surface voltage (or time) dependence of the yield for negative charging for $E_b > E_2$, based on a charging capacitor with time constant, τ_Q , was proposed by Thomson (Thomson, 2001).

$$[1 - Y(t; E_b)] = [1 - Y(E_b)] e^{-(V_s(t)/V_{inj}^{se})} = [1 - Y(E_b)] e^{-(t/\tau_Q)} \text{ for } \theta \geq q_e V_s(t) \geq (E_2 - E_b), \quad (4.11)$$

τ_Q is a time constant for the exponential approach of the yield to unity, as charge is accumulated. Then, for a dynamic yield for negative charging with $E_b > E_2$, the injection current in Eq. 4.6 or Eq. 4.10 becomes

$$\begin{aligned} \bar{J}_o &\equiv \frac{\int_0^t J_{inj}(t') dt'}{\int_0^t dt'} = \left(\frac{J_o}{t} \right) \int_0^t \{1 - Y[E_b - q_e V_s(t')]\} dt' \\ &= \left(\frac{J_o}{t} \right) [1 - Y(E_b)] \int_0^t e^{-(t'/\tau_Q)} dt' = J_o [1 - Y(E_b)] \left(\frac{\tau_Q}{t} \right) [1 - e^{-(t/\tau_Q)}] \end{aligned}$$

(dynamic emission, no dissipation for $\theta \geq q_e V_s(t) \geq (E_2 - E_b)$). (4.12)

The injection current falls off exponentially with time as charge accumulates and the yield approaches unity. A similar model is applicable for negative charging for $E_b < E_1$, below the first crossover energy. Hoffmann (2010) and Thomson (2001) also proposed a time-dependant model for positive charging for $E_1 < E_b < E_2$; the explicit expression for $V_s(t)$ in this case is left for future work.

The effects of emission, as given by Eqs. 4.9, 4.10 and 4.11, can be incorporated into a generalized definition of the injection voltage through the time-dependant injection current as

$$V_s(t) = V_{inj}^{nd}(t) \left(\frac{t}{\tau_o} \right) \quad (\text{no dissipation}), \quad (4.13)$$

with

$$V_{inj}^{nd}(t) = \begin{cases} V_{inj}^{ne} = \frac{\bar{J}_0}{\sigma_0} \left[D \left(1 - \frac{R(E_b)}{D} \right) \right] & \text{(no emission).} \\ V_{inj}^{se} = \frac{\bar{J}_0}{\sigma_0} [1 - Y(E_b)] \left[D \left(1 - \frac{R(E_b)}{D} \right) \right] & \text{(static emission).} \\ V_{inj}^{de}(t) = \frac{\bar{J}_0}{\sigma_0} [1 - Y(E_b)] \left(\frac{\tau_Q}{t} \right) \left[D \left(1 - \frac{R(E_b)}{D} \right) \right] [1 - e^{-(t/\tau_Q)}] & \text{(dynamic emission)} \\ V_{inj}^{ge}(t) = \frac{\bar{J}_0}{\sigma_0} \left[D \left(1 - \frac{R(E_b)}{D} \right) \right] \left\{ \left(\frac{1}{t} \right) \int_0^t \{1 - Y[E_b - q_e V_s(t')]\} dt' \right\} & \text{(general emission).} \end{cases} \quad (0 \geq q_e V_s(t) \geq (E_2 - E_b)).$$

Similar expressions for $V_{inj}^{nd}(t)$ in terms of injected charge densities $\Sigma(z, t)$ and $n_t(z, t)$ can be written using the notation from Eq. 4.7 and Eq. 4.8, respectively.

4.2.3. Models Including Dissipation

To include charge dissipation (assumption 7), the time-averaged incident current density, \bar{J}_0 , (see Eqs. 4.6, 4.7, or 4.8) is replaced with the time-averaged net current, $J_{net}(t)$. The net current density includes three terms in the dissipation current, J_{out} , (see FIG. 4.5) for (i) the electron emission current, J_{emit} , and the currents from the deposited charge layer dissipated through the (ii) upper and (iii) lower material surfaces to ground, J_{up} and J_{down} , respectively:

$$J_{net}(t) = \bar{J}_0 - J_{out}(t) = \bar{J}_0 - [J_{emit}(t) + J_{up}(t) + J_{down}(t)] = \bar{J}_0 - \left[Y(E_b) \bar{J}_0 + \frac{\sigma_{up} |\Delta V_{up}|}{R(E_b)} + \frac{\sigma_{down} |\Delta V_{down}|}{(D - R(E_b))} \right]. \quad (4.14)$$

To incorporate dissipation through a potentially time-dependant expression for the conductivities above ($0 < z < R$) and below ($R < z < D$) the embedded charge layer ($\sigma_{up}(t)$ and $\sigma_{down}(t)$, respectively), the current densities J_{up} and J_{down} are written in terms of general conductivities σ_{up} and σ_{down} as

$$J_{(down)}^{up} = \sigma_{(down)}^{up} F_{(down)}^{up} = \frac{\sigma_{(down)}^{up} \Delta V_{(down)}^{up}}{\left(\frac{R(E_b)}{D - R(E_b)} \right)} \hat{z}. \quad (4.15)$$

Since there is initially no charge distribution in the region below $R(E_b)$ (assumptions 4 and 5), $\Delta V_{down} = -V_d$. If there is a grounded upper surface layer, $\Delta V_{up} = V_d$. For upper and lower grounded surfaces with $\Delta V_{up} = -\Delta V_{down} = V_d$, insertion of J_{net} from Eq 4.21 into Eq. 4.13 yields an expression with V_d on both sides of the equation:

$$V_d(t) = \left\{ \bar{J}_o [1 - Y(E_b)] - \frac{\sigma_{up} V_d(t)}{R(E_b)} - \frac{\sigma_{down} V_d(t)}{[D - R(E_b)]} \right\} \left[\frac{t}{\varepsilon_o \varepsilon_r} \right] \left[D \left(1 - \frac{R(E_b)}{D} \right) \right]. \quad (4.16)$$

Solving explicitly for the time-dependent surface potential yields

$$V_b(t) = \left\{ \frac{\bar{J}_o t}{\varepsilon_o \varepsilon_r} [1 - Y(E_b)] D \left[1 - \frac{R(E_b)}{D} \right] \right\} \left\{ 1 + \left[\frac{\sigma_{up}}{\varepsilon_o \varepsilon_r} \left(\frac{D - R(E_b)}{R(E_b)} \right) + \frac{\sigma_{down}}{\varepsilon_o \varepsilon_r} \right] t \right\}^{-1}$$

(static emission, dissipation, upper and lower grounded surfaces). (4.17)

If the upper surface layer is not grounded and $\sigma_{up} \rightarrow 0$, then the J_{up} term drops out after charge redistribution is complete (assumption 5) and Eq. 4.17 reduces to

$$V_d(t) = \left\{ \frac{\bar{J}_o t}{\varepsilon_o \varepsilon_r} [1 - Y(E_b)] D \left[1 - \frac{R(E_b)}{D} \right] \right\} \left\{ 1 + \left[\frac{\sigma_{down}}{\varepsilon_o \varepsilon_r} \right] t \right\}^{-1}$$

(static emission, dissipation, lower grounded surface), (4.18)

where we assume $V_s \rightarrow V_d$ for a floating surface potential. Then, from Eq. 4.18,

$$V_d(t \rightarrow \infty) = V(t \rightarrow \infty) \equiv V_{inj}^{wd}. \quad (4.19)$$

Combining Eqs 4.18 and 4.19, we have

$$V_d(t) = V_{inj}^{wd}(t) \left(\frac{t}{\tau_o} \right) \left\{ 1 + \left[\frac{\sigma_{up}(t)}{\varepsilon_o \varepsilon_r} \left(\frac{D - R(E_b)}{R} \right) + \frac{\sigma_{down}(t)}{\varepsilon_o \varepsilon_r} \right] t \right\}^{-1}$$

(upper and lower grounded surfaces), (4.20)

$$V_s(t) = V_{inj}^{wd}(t) \left(\frac{t}{\tau_o} \right) \left\{ 1 + \left[\frac{\sigma_{down}(t)}{\varepsilon_o \varepsilon_r} \right] t \right\}^{-1} \quad \text{(lower grounded surface)} \quad (4.21)$$

with the expression Eq. 4.13 for $V_{inj}^{nd}(t)$ modified to include dissipation as

$$V_{inj}^{wd}(t) = \begin{cases} V_{inj}^{ne} = \frac{\bar{J}_o}{\sigma_o} \left[D \left(1 - \frac{R(E_b)}{D} \right) \right] & \text{(no emission).} \\ V_{inj}^{se} = \frac{\bar{J}_o}{\sigma_o} [1 - Y(E_b)] \left[D \left(1 - \frac{R(E_b)}{D} \right) \right] & \text{(static emission).} \\ V_{inj}^{de}(t) = \frac{\bar{J}_o}{\sigma_o} [1 - Y(E_b)] \left[D \left(1 - \frac{R(E_b)}{D} \right) \right] \left(\frac{\tau_Q}{t} \right) \left[1 - e^{-\left(\frac{t}{\tau_Q} \right) \left\{ 1 + \left[\frac{\sigma_{up}(t)}{\varepsilon_o \varepsilon_r} \left(\frac{D - R(E_b)}{R} \right) + \frac{\sigma_{down}(t)}{\varepsilon_o \varepsilon_r} \right] t \right\}^{-1}} \right] & \text{(dynamic emission)} \\ V_{inj}^{ge}(t) = \frac{\bar{J}_o}{\sigma_o} \left[D \left(1 - \frac{R(E_b)}{D} \right) \right] \left\{ \left(\frac{1}{t} \right) \int_0^t \{ 1 - Y[E_b - q_e V_s(t')] \} dt' \right\} & \text{(general emission).} \end{cases}$$

(with dissipation) (4.22)

Note we have assumed the term in curly brackets in the exponent for $V_{inj}^{de}(t)$ is nearly unity or varies slowly with time (*i.e.*, $t < \tau_Q$) to solve the time integral analytically; since τ_Q is a measure of time to accumulated charge, this assumption is related to Walden's assumption that $f(F)$ varies slowly with F as compared to the exponential function $\exp[f(F)]$ (Walden, 1972).

In the long-time equilibrium limit, one can assume that $\sigma_{up}(t \rightarrow \infty) = \sigma_{down}(t \rightarrow \infty) \rightarrow \sigma_o$. As discussed below, for electrode injection with an infinite reservoir of charge carriers available $\sigma_o \rightarrow \sigma_{DC}$, where σ_{DC} is the long-time equilibrium conductivity of the material (often referred to as the dark current conductivity in reference to the fact that the incident radiation is turned off after a time t_{on}). Under these conditions, V_{inj}^{wd} and σ_{DC} are proportional to the total number of trap states and provide a direct measurement of N_t . This is a fundamental difference between Constant Voltage (CVC) and Charge Storage (CSC) Chamber measurement techniques.

Four cases are considered below for successively more complex (and realistic) models of $\sigma_{up}(t)$ and $\sigma_{down}(t)$ to include dissipation in Eqs. 4.20 and 4.21:

- (i) No dissipation (electron transport), $\sigma_{up}(t) = \sigma_{down}(t) \rightarrow 0$.
- (ii) Static-charge dissipation with time-independent conductivity, $\sigma_{up}(t) = \sigma_{down}(t) \xrightarrow{t \gg \tau_{transit}} \sigma_o$. This allows time-dependant change of the magnitude of the charge distributions, but not in the spatial distribution of the charges. Drift or dark current (σ_{DC}), AC ($\sigma_{AC}(\nu)$), and static RIC (σ_{RIC}^o for $0 < R$ only) conductivities are included. Note, if we assume a static dissipation without allowing the system to come to equilibrium, then $\sigma(t) \rightarrow \sigma_o$ with the quasi-equilibrium conductivity $\sigma_o \geq \sigma_{DC}$.
- (iii) Dynamic-charge dissipation with time-dependent conductivity, $\sigma(t)$. This allows for the additional possibility of the motion of the embedded charge layer (or equivalently, of the center of the charge distribution, $z_d(t)$). Polarization ($\sigma_{pol}(t)$), diffusion ($\sigma_{diffusion}(t)$), and dynamic RIC ($\sigma_{RIC}(t)$ for $0 < R$ only) conductivities are added.

- (iv) Dynamic charge dissipation with more general time-dependant conduction that allows for the evolution of the spatial distribution of the embedded charge. Dispersion ($\sigma_{dispersion}(t < \tau_{transit})$) and transit ($\sigma_{dispersion}(t > \tau_{transit})$) conductivities are added.

For a model with no dissipation, refer to Eq. 4.9, which predicts a surface voltage that increases linearly with time.

For the simplest static dissipation model, we assume a time-independent conductivity

$$\sigma_{up}(t) = \sigma_{down}(t) \xrightarrow{t \gg \tau_{transit}} \sigma_o \quad (\text{static dissipation}) \quad (4.23)$$

set equal to the dark current conductivity limit in Eqs. 4.20, 4.21 and 4.22 for consistency. The expression for $V_d(t)$, $V_s(t)$, and $V_{inj}^{wd}(t)$ are given by Eqs. 4.20, 4.21, and 4.22, respectively. A somewhat more general expression maintains a time-independent bulk conductivity, but includes a time-independent static RIC term.

$$\sigma_{up}(t) \xrightarrow{t \gg \tau_{transit}} \sigma_o + \sigma_{RIC}^o \quad (\text{static dissipation with RIC}). \quad (4.24)$$

$$\sigma_{down}(t) \xrightarrow{t \gg \tau_{transit}} \sigma_o \quad (\text{static dissipation}). \quad (4.25)$$

σ_{down} does not include a RIC term, since (by assumption 4) there is no radiation below the penetration depth. $\sigma_{AC}(\nu)$ would need to be included here for periodic applied fields.

A more complete model of charge dissipation extends the transport of charge through the highly disordered insulating materials to include nonohmic and time-dependant conduction. The Ampere-Maxwell equation,

$$\vec{\nabla} \times \vec{H} = J_c + \frac{\partial}{\partial t}(\epsilon_o \epsilon_r F) \equiv J_c + J_{displacement}, \quad (4.26)$$

separates the response current densities into two types, the free charge transport current density, J_c , and the charge displacement current density, $J_{displacement}$. Note for a 1D model (assumption 1), the total current density must be independent of z to satisfy charge conservation, so the charge transport and displacement current densities are complementary.

The free-charge transport current density, $J_c = J_{cond} + J_{diffusion}$ (also called the convection or carrier particle current density), is the sum of the conduction and diffusion current densities. The conduction current density, $J_{cond} = \sigma_{cond} F$, is a response of free carriers to the applied field, F , and is characterized by the conductivity, σ_{cond} . The additive contributions to σ_{cond} considered here include the steady-state conductivities σ_{DC} , σ_{RIC}^0 , and $\sigma_{AC}(\nu)$, as described in Wilson and Dennison (2010). These conductivities assume a homogeneous (free) space charge distribution.

The diffusion current, $J_{diffusion} \sim [\partial n(z, t) / \partial z] [\partial z_d(t) / \partial t]$, results from the evolution of the electric field produced by the motion of a spatial gradient in the free carrier (space charge) distribution as the center of the charge distribution, $z_d(t)$, progresses (diffuses or hops for HDIM) towards a uniform distribution of space charge across the dielectric (*e.g.*, $[\partial n(z, t \rightarrow \infty) / \partial z] \rightarrow 0$). $J_{diffusion}$ is usually written in terms of a diffusivity or diffusion constant, D_o , as $J_{diffusion}(t) = -q_e D_o [\partial n(z, t) / \partial z]$, where $D_o \equiv \frac{1}{3} v_{diff} \tau_{diff}$ is proportional to the velocity $v_{diff} = \partial z_d(t) / \partial t$ and relaxation time τ_{diff} of the diffusing carriers.

The dispersive (for $t < \tau_{transit}$) and transit (for $t > \tau_{transit}$) conductivities are two parts of a contribution that results from the broadening of the spatial distribution of the space charge, $J_{dispersive}^{transit} \sim \left[\frac{\partial}{\partial t} (\partial n(z) / dz) \right]$, which ultimately trace to a distribution of trap filling and retention times (or equivalently a distribution of trap energies). Dispersion results from a non-zero relaxation time (or distribution of relaxation times) associated with the response of the space charge distribution to a changing electric field; hence, $J_{dispersive}(t)$ and $J_{transit}(t)$ are considered displacement currents. For dispersive and transit contributions, the space charge distribution is broadening in time, progressing towards a uniform distribution of space charge across the dielectric (*e.g.*, $[\partial n(z, t \rightarrow \infty) / \partial z] \rightarrow 0$, so that $\left[\frac{\partial}{\partial t} (\partial n(z, t \rightarrow \infty) / dz) \right] \rightarrow 0$). The transition from dispersive to transit behavior, and the concomitant drop in the displacement current, occurs at a time $\tau_{transit}$ at which the first of the injected charge carriers have traversed

across the sample, thereby reducing the magnitude of the charge distribution that can further disperse (Scher and Montroll, 1975; Zallen and Scher, 1971). Obviously, $\tau_{transit}$ is directly related to trap filling and relaxation times.

The final current density considered here, $\sigma_{RIC}(t; \tau_{RIC}^1, \tau_{RIC}^2)$, is also controlled by the trap filling rate, ν_{et} , and release rate, ν_{te} (or equivalently trap energies), for electrons excited from the valence band to conduction band by energy deposition from incident radiation. One can consider RIC as the transport of bound charge, which has been converted for a finite time to free charge by the external influence of incident radiation.

A general form of conductivity in HDIM with explicit time dependence for HDIM takes the form

$$\sigma(t) = \sigma_{DC} \left[\frac{1 + \frac{\sigma_{AC}(\nu)}{\sigma_{DC}} + \frac{\sigma_{pol}^0}{\sigma_{DC}} e^{\frac{-t}{\tau_{pol}}} + \frac{\sigma_{diffusion}^0}{\sigma_{DC}} t^{-1} + \frac{\sigma_{dispersive}^0}{\sigma_{DC}} t^{-(1-\alpha)} + \frac{\sigma_{transit}^0}{\sigma_{DC}} t^{-(1+\alpha)} + \frac{\sigma_{RIC}^0}{\sigma_{DC}} \left(1 - e^{-\tau_{RIC}^1/(t-t_{on})} \right) (1 + (t - t_{off})/\tau_{RIC}^2)^{-1}} \right], \quad (4.27)$$

as outlined in Wintle (1983) and Dennison *et al.* (2009) and described in detail by Sim (2012) and the extensive references therein. Here the conductivity terms are:

- $\sigma_{DC} \equiv q_e n_e \mu_e$ is the very long timescale equilibrium conductivity without radiation-induced contributions, sometimes referred to as dark current or drift conduction.
- $\sigma_{AC}(\nu)$ is a frequency-dependant AC conduction, which is a measure of the dielectric response to a periodic applied electric field and is only active for periodic charge injection (Wintle, 1983).
- $\sigma_{pol}(t) \equiv \sigma_{pol}^0 \cdot e^{\frac{-t}{\tau_{pol}}}$ is an exponentially decaying conduction due to polarization of the material as the internal bound charge of the dielectric material rearranges in response to an applied electric field on a time scale τ_{pol} .

- $\sigma_{diffusion}(t) \equiv \sigma_{diffusion}^0 \cdot t^{-1}$ is an inverse power law, diffusion-like conductivity resulting from the gradient of the space charge spatial distribution.
- $\sigma_{dispersive}(t) \equiv \sigma_{dispersive}^0 \cdot t^{-(1-\alpha)}$ (for $t < \tau_{transit}$) and $\sigma_{transit}(t) \equiv \sigma_{transit}^0 \cdot t^{-(1+\alpha)}$ (for $t > \tau_{transit}$) are two parts of a contribution that result from the broadening of the spatial distribution of the space charge participating in transport through a coupling with the energy distribution of trap states.
- $\sigma_{RIC}(t; \dot{D}, \tau_{RIC}^1, \tau_{RIC}^2) \equiv \sigma_{RIC}^0(\dot{D}(t)) \left(1 - e^{-\tau_{RIC}^1/(t-t_{on})}\right) \left(1 + (t - t_{off})/\tau_{RIC}^2\right)^{-1}$ is a radiation-induced conductivity term resulting from energy deposition within the material, and is only active for radiation charge injection. $\sigma_{RIC}(t)$ depends on the energy deposition rate, $\dot{D}(t)$, through the electron beam or injected-current time dependence. It also has time dependence due to the rates of response of the materials as characterized by τ_{RIC}^1 and τ_{RIC}^2 , which are closely related to the trap filling and release rates. $\sigma_{RIC}(t)$ is discussed further in Section 4.3.

4.2.4. Surface Voltage Probe Charging and Discharge Models with Dissipation

Following the arguments detailed in Sim (2012), this general conductivity formula for HDIM Eq. 4.27 and the surface voltage formulas Eqs. 4.20-22 can be simplified for the surface voltage probe applications here for charging and discharging of a material using a nonpenetrating electron-beam-charged pulse injection with a floating upper surface. We make three approximations based on the timescale for data acquisition times, $t_0 < t < t_{max} < \tau_{transit}$:

- The polarization term, $\sigma_{pol}(t)$, can be neglected. For most polymeric insulators (including LDPE and Kapton HNTM), the polarization time constant, $\tau_{pol} < 10$ s, is shorter than the time before the first surface voltage measurement for experiments considered here (typically $\gtrsim 100$ s). Higher frequency AC conductivity is also neglected in all cases for the pulsed injection.

- (b) The measurements described in this thesis do not extend to times greater than the transit time, τ_{transit} . Hence, the transition from $\sigma_{\text{dispersive}}$ to σ_{transit} can typically be neglected, except as specifically noted. An exception for long-duration discharge measurements for Kapton HNTM is discussed in Section 4.3.2. Since the experiments typically run for durations $t_{\text{max}} < \tau_{\text{transit}}$, the conductivity does not reach equilibrium at σ_{DC} , but rather approaches quasi-equilibrium at $\sigma_{0>}$ σ_{DC} .
- (c) Time-averaged RIC during charging is approximately $\langle \sigma_{\text{RIC}}(t; \dot{D}, \tau_{\text{RIC}}^1, \tau_{\text{RIC}}^2) \rangle_t = \sigma_{\text{RIC}}^0(\dot{D})$. The beam pulse and repetition rates used are such that lower $\sigma_{\text{RIC}}(t)$ due the rise time governed by τ_{RIC}^1 is approximately compensated for by the persistent RIC governed by τ_{RIC}^2 after the beam is turned off. This assumption is discussed further in Section 4.4 on the charge diffusion measurements. RIC is assumed to not be active during discharge experiments. The only exception would be for situations where data are acquired soon after the beam is turned off on timescales $t_{\text{off}} < \tau_{\text{RIC}}^2$, in which case a decaying persistent RIC term, $\sigma_{\text{RIC}}(t; \dot{D}, \tau_{\text{RIC}}^2) \equiv \sigma_{\text{RIC}}^0(\dot{D}(t)) (1 + (t - t_{\text{off}})/\tau_{\text{RIC}}^2)^{-1}$ would be included.

We make five additional approximations related to the beam energy, $E_b=5$ keV, assuming:

- (d) A nonpenetrating beam of energy that injects charge at $R(E_b) < D$ so that σ_{RIC} is nonzero only up to a depth $R(E_b)$ in the RIC region. From Eq. 4.22, the surface voltage scales as $[D - R(E_b - q_e V_s)]$; however, $R \ll D$ (here typically, $R < 0.6 \mu\text{m}$ and $D \sim 25 \mu\text{m}$ with $(R/D) \lesssim 2\%$), so changes in R and the extent of the RIC region with landing energy have minimal effect. For LDPE, this surface voltage term increases as the sample charges to V_s^{max} by $\sim 1\%$, as $R(E_b=5000 \text{ eV}) \sim 0.60 \mu\text{m}$ decreases to $R(E_b - q_e V_s^{\text{max}} \sim 3800 \text{ eV}) \sim 0.32 \mu\text{m}$ at $V_s^{\text{max}} \sim 1200$ V. For Kapton HNTM, the surface voltage term also increases by $\sim 1\%$ as the sample charges to V_s^{max} , as $R(E_b=5000 \text{ eV}) \sim 0.50 \mu\text{m}$ decreases to $R(E_b - q_e V_s^{\text{max}} \sim 2200 \text{ eV}) \sim 0.15 \mu\text{m}$ at $V_s^{\text{max}} \sim 2800$ V. The average change in current due to this term will be approximately half of this change in surface voltage. Hence, we can typically neglect this $\lesssim 1/2\%$ change in

electrode current due to the energy dependence of the range; *i.e.*, $[D - R(E_b - q_e V_s)] \approx [D - R(E_b)]$. For discharge experiments, there is no time-dependant injection source. An initial space-charge distribution with a uniform distribution in the RIC region $0 < z < R(E_b)$ is assumed (see Eq. 4.8).

- (e) The electron beam energy, $E_b > E_2$, leads to negative charging. Electron emission effectively reduces the incident current density and equilibrium surface voltage by a factor of

$$\left[\frac{\int_0^t \{1 - Y[E_b - q_e V_s(t')]\} dt'}{\int_0^t dt'} \right] / [1 - Y(E_b)] \quad (\text{see Eq. 4.12}), \text{ where } Y(t; V_s(t), E_b) \text{ is the time-}$$

dependant (or equivalently the charge-dependant) total electron yield of the material. For the surface voltage probe experiments, the total yield depends significantly on incident energy, or more correctly on the landing energy, $E_b - q_e V_s(t)$, for biased samples, as predicted by the yield curves in Section 4.1. For the LDPE experiments V_{inj} decreases by $\sim 10\%$, where $[1 - Y(E_b = 5000 \text{ eV})] \sim 0.50$ decreases to $[1 - Y(E_b - q_e V_s^{max} \sim 3800 \text{ eV})] \sim 0.45$ at $V_s^{max} \sim 1200 \text{ V}$. For Kapton HNTM V_{inj} decreases by $\sim 27\%$, where $[1 - Y(E_b = 5000 \text{ eV})] \sim 0.68$ decreases to $[1 - Y(E_b - q_e V_s^{max} \sim 2200 \text{ eV})] \sim 0.50$ at $V_s^{max} \sim 2800 \text{ V}$. From these arguments and data, we see that, as expected from physical arguments, assuming a static emission model is incorrect, and will lead to a 10-25% overestimation of the equilibrium surface voltage. Here, E_b (5000 eV) is greater than the second crossover energy E_2 ($\sim 1750 \text{ eV}$ and $\sim 900 \text{ eV}$ for LDPE and Kapton HNTM, respectively; see Section 4.1). Therefore, for $E_b > E_2$ in the negative charging regime, as the samples charge, the landing energy decreases from E_b toward a lowest possible value at E_2 . We therefore adopt a model with dynamic emission, with $0 \geq q_e V_s(t) \geq (E_2 - E_b)$ for $V_{inj}^{de}(t)$ given by Eq. 4.13. This is discussed further in Section 4.3 for Kapton HNTM charging data.

- (f) An ungrounded (floating) upper surface, so that no charge leaves the RIC region and the only current contributing to J_{up} are the RIC current driven by the charge gradient in the RIC region

and a displacement current resulting from charge redistribution within the RIC region. If assumption c is evoked, $\langle \sigma_{RIC}(t; \dot{D}, \tau_{RIC}^1, \tau_{RIC}^2) \rangle_t = \sigma_{RIC}^0(\dot{D})$, eliminating the time-dependant RIC. To model a floating upper surface for the general model in Eqs. 4.2 and 4.3, $z_{ext} \rightarrow -\infty$ with $V_{ext} \rightarrow 0$ and $F_{ext} \rightarrow 0$. There is no electrode injection current for data analyzed here, so $V_{ext} = 0$.

- (g) The contribution to V_s from redistribution of charge in the RIC region is neglected and $V_s \rightarrow V_d$, in almost every case considered below. These displacement current densities, which scale as $[(\Sigma/R) \cdot (\Delta z / \Delta \tau)]$ are small, since (i) $R(E_b) \ll D$ and (ii) the charge in the RIC region redistributes a distance $\Delta z \lesssim R/2$ on a timescale, $\Delta \tau$, which are much faster than timescales $\tau_{transit}$ for charge transport through the lower field region ($R > z > D$) (i.e., $\sigma_{up} \gtrsim \sigma_{RIC}^0 \gg \sigma_{DC} \lesssim \sigma_{down}$). Therefore, except where noted below, we assume a uniform injected charge carrier density per unit volume, $\bar{n}_t(t)$, given by Eq. 4.8 through assumption 5, for an initially uniform charge distribution in the RIC region $0 < z < R(E_b)$ with a charge centroid at $z_d(t) = 1/2 R(E_b)$ and $\sigma_{up} \rightarrow 0$ after time $\Delta \tau \ll \tau_{transit}$.
- (h) Maximum charging for a given experiment does not reach full equilibrium, but rather occurs at $V_s^{max} \leq (E_2 - E_b)$ where $\bar{n}_t(t) \rightarrow n_t^{max} \leq N_t$. Note, upper bound on charging for electron beam injection can occur in two ways: (i) all available traps in the RIC region are filled and $n_t^{max} = N_t$, or (ii) $V_s^{max} = (E_2 - E_b)$ where the yield reaches $Y=1$ and no further net charge injection occurs, with $n_t^{max} < N_t$. As noted above, in our experiments $V_s^{max} \leq 30\% \cdot (E_2 - E_b)$.

Taken together, these restrictions for the typical experimental condition considered in charging and discharge experiments like those presented in this chapter, reduce the time-dependent expression for nonohmic conductivity in HDIM given by Eq 4.27 to

$$\sigma_{up}(t) \approx \sigma_0 \left\{ \left[\frac{\sigma_{RIC}^0(\dot{D})}{\sigma_0} \right] + \left[\frac{\sigma_{diffusion}^0}{\sigma_0} \right] t^{-1} + \left[\frac{\sigma_{dispersive}^0}{\sigma_0} \right] t^{-(1-\alpha)} \right\} \xrightarrow{t > \Delta \tau} \sigma_{RIC}^0(\dot{D}) \xrightarrow{g} 0 \quad ; \quad 0 < z < R(E_b), \quad (4.28)$$

which goes to zero under assumption g, and

$$\sigma_{\text{down}}(t) \approx \sigma_0 \left\{ 1 + \left[\frac{\sigma_{\text{diffusion}}^0}{\sigma_0} \right] t^{-1} + \left[\frac{\sigma_{\text{dispersive}}^0}{\sigma_0} \right] t^{-(1-\alpha)} \right\} \quad ; R(E_b) < z < D. \quad (4.29)$$

To find expressions for the surface voltage $V_s(t)$, given approximations (a) through (h) above, one must insert Eq. 4.28 for $\sigma_{\text{up}}(t)$ and Eq. 4.29 for $\sigma_{\text{down}}(t)$ into Eqs. 4.20 and 4.21 and simplify; this yields

$$V_d(t) = V_{\text{inj}}^{\text{de}}(t) \left(\frac{t \sigma_0}{\epsilon_0 \epsilon_r} \right) \left\{ 1 + \left(\frac{t \sigma_0}{\epsilon_0 \epsilon_r} \right) \cdot \left[1 + \frac{\sigma_{\text{RIC}}^0(D)}{\sigma_0} \left(\frac{D - R(E_b)}{R(E_b)} \right) + \frac{\sigma_{\text{diffusion}}^0}{\sigma_0} (t^{-1}) + \frac{\sigma_{\text{dispersive}}^0}{\sigma_0} (t^{-(1-\alpha)}) \right] \right\}^{-1}. \quad (4.30)$$

for a lower grounded surface with displacement currents for the RIC region (that is without assumption g) and

$$V_s(t) = V_{\text{inj}}^{\text{de}} \left(\frac{t \sigma_0}{\epsilon_0 \epsilon_r} \right) \left\{ 1 + \left(\frac{t \sigma_0}{\epsilon_0 \epsilon_r} \right) \cdot \left[1 + \frac{\sigma_{\text{diffusion}}^0}{\sigma_0} (t^{-1}) + \frac{\sigma_{\text{dispersive}}^0}{\sigma_0} (t^{-(1-\alpha)}) \right] \right\}^{-1}. \quad (4.31)$$

Here the dynamic injection current in the negative charging regime from Eq. 4.29, written in terms of uniform charge density n_t^{max} in the RIC region (see Eq. 4.9 and assumption h) is

$$V_{\text{inj}}^{\text{de}} = \left[\frac{q_e n_t^{\text{max}}}{\epsilon_0 \epsilon_r} [1 - Y(E_b)] \right] \left[R(E_b) D \left(1 - \frac{R(E_b)}{2D} \right) \right] \left[\frac{\tau_Q}{\tau_0} \right] \left[1 - e^{-\left(\frac{t}{\tau_Q} \right) \left\{ 1 + \left(\frac{t \sigma_0}{\epsilon_0 \epsilon_r} \right) \left[1 + \frac{\sigma_{\text{diffusion}}^0}{\sigma_0} (t^{-1}) + \frac{\sigma_{\text{dispersive}}^0}{\sigma_0} (t^{-(1-\alpha)}) \right] \right\}^{-1}} \right]$$

(dynamic emission with negative charging for $0 \geq q_e V_s(t) \geq (E_2 - E_b)$, with dissipation). (4.32)

Finally, combining Eqs. 4.31 and 4.32 into a single expression for dynamic emission with negative charging and dissipation using assumptions a through h, we arrive at

$$V_s(t) = \frac{\left[\frac{q_e n_t}{\epsilon_0 \epsilon_r} [1 - Y(E_b)] \right] \left[R(E_b) D \left(1 - \frac{R(E_b)}{2D} \right) \right] \left[\frac{\tau_Q}{\tau_0} \right] \left[1 - e^{-\left(\frac{t}{\tau_Q} \right) \left\{ 1 + \left(\frac{t \sigma_0}{\epsilon_0 \epsilon_r} \right) \left[1 + \frac{\sigma_{\text{diffusion}}^0}{\sigma_0} (t^{-1}) + \frac{\sigma_{\text{dispersive}}^0}{\sigma_0} (t^{-(1-\alpha)}) \right] \right\}^{-1}} \right]}{\left\{ 1 + \left(\frac{t \sigma_0}{\epsilon_0 \epsilon_r} \right) \cdot \left[1 + \frac{\sigma_{\text{diffusion}}^0}{\sigma_0} (t^{-1}) + \frac{\sigma_{\text{dispersive}}^0}{\sigma_0} (t^{-(1-\alpha)}) \right] \right\}}. \quad (4.33)$$

4.2.5. Charge Decay Models

A simple form of the voltage relation follows from a decaying capacitor model, with time-dependant conductivity

$$V(t) = V_0 e^{-t \sigma_{\text{down}}(t) / \epsilon_0 \epsilon_r}. \quad (4.34)$$

For times less than the transit time or $t < (\epsilon_o \epsilon_r / \sigma_{DC})$, the exponent can be expanded as

$$V(t) \approx V_o \left[1 - \left(\frac{\sigma_{down}(t)t}{\epsilon_o \epsilon_r} \right) \right] = V_o \left[1 - \left(\frac{\sigma_o t}{\epsilon_o \epsilon_r} \right) \left\{ 1 + \left[\frac{\sigma_{diffusion}^o}{\sigma_o} \right] t^{-1} + \left[\frac{\sigma_{dispersive}^o}{\sigma_o} \right] t^{-(1-\alpha)} \right\} \right], \quad (4.35)$$

where the restrictions for the typical experimental condition considered above for charging and discharge experiments, like those presented in this chapter, reduce the time-dependent expression for nonohmic conductivity in HDIM given by Eq 4.25 to

$$\sigma_{down}(t) \approx \sigma_o \left\{ 1 + \left[\frac{\sigma_{diffusion}^o}{\sigma_o} \right] t^{-1} + \left[\frac{\sigma_{dispersive}^o}{\sigma_o} \right] t^{-(1-\alpha)} \right\} \quad ; R(E_b) < z < D. \quad (436)$$

4.3. Fits to Charge Accumulation and Charge Dissipation Data

The data were fit to both the higher order charging and discharging models. Keeping the common parameters (σ_o , σ_{diff} , σ_{disp} , α) amongst the two models consistent and varying the unique parameters (τ_Q , V_o , N_t), fits were determined (FIG. 4.7 and FIG. 4.8). The fits was made assuming σ_o was close to that of the DC conductivity of literature values. All the other parameters were adjusted until a reasonable fit of the data and parameters were achieved. The resulting parameters can be seen in Table 4.2. The explanation of these parameters can be found in the subsequent sections.

TABLE 4.2. Fitting parameters for charging and discharging fits.

Material	σ_o ($\Omega\text{-cm}$) ⁻¹	σ_{diff} ($\Omega\text{-cm}$) ⁻¹	σ_{disp} ($\Omega\text{-cm}$) ⁻¹	α	V_o (V)	τ_Q (1/s)	N_t (traps/cm ³)
LDPE	1.45×10^{-18}	1.45×10^{-18}	1.9×10^{-15}	0.50	1204	1050	6.1×10^{18}
Kapton HN™	5.0×10^{-20}	6.8×10^{-15}	8.0×10^{-17}	0.55	2820	675	6.2×10^{20}

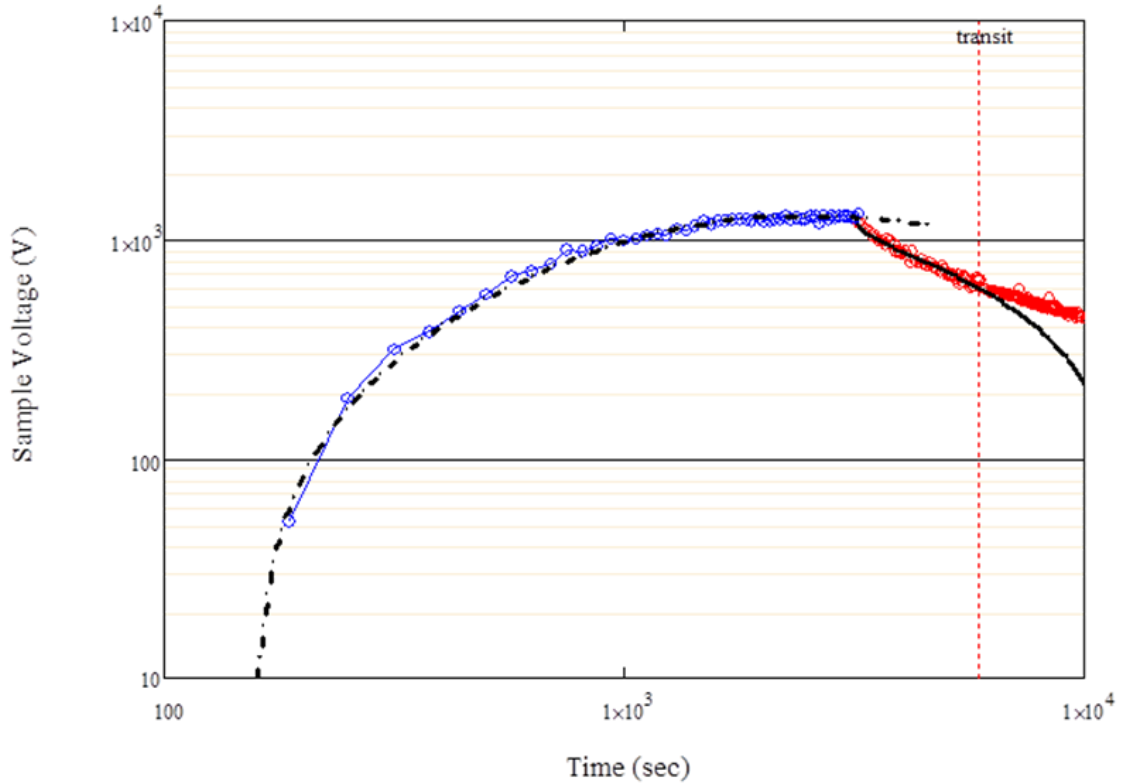


FIG. 4.7. Charging and discharge data of LDPE with fits to include emission and nonohmic conductivity. Blue data points represent charge up and red data represents decay. Fits to the charging data (Eq. 4.33) is represented by the dashed black line. Fits to the decay (Eq. 35) is represented by the solid black line. Vertical red line represents the estimated transit time of 6100 s from initiation of charging.

4.3.1. Charge Accumulation

Four electron beam charging models discussed above are considered and fit to LDPE and Kapton HN™ data, shown in FIG. 4.9 and FIG. 4.10, respectively. These models correspond to the following cases where the upper surface is left ungrounded with:

- i. no dissipation of charge, neglecting the effects of electron emission (Eq. 4.9),
- ii. no dissipation of charge, including electron emission (Eq. 4.10),
- iii. ohmic charge dissipation, including electron emission (Eq. 4.22), and
- iv. nonohmic charge dissipation, including electron emission (Eq. 4.33).

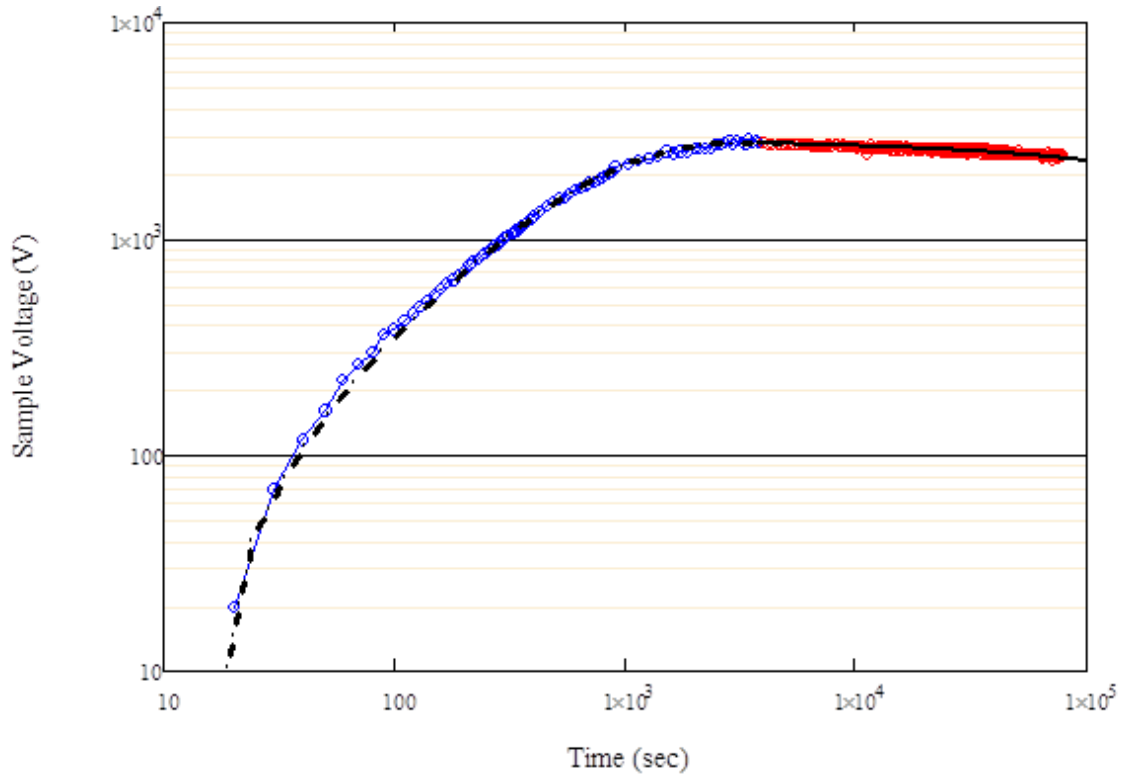


FIG. 4.8. Charging and discharge data for Kapton HN™ with fits to include emission and nonohmic conductivity. Blue data points represent charge up and red data represents decay. Fits to the charge up (Eq. 4.33) is represented by the dashed black line. Fits to the decay (Eq. 4.36) is represented by the solid black line.

The curves corresponding to each of the models show a different level of accuracy as different emission and dissipation methods are included. The benefit of viewing the data with a succession of dissipation mechanisms is that it highlights which mechanisms drive the charge accumulation of the material. The fits to LDPE and Kapton HN™ show without any dissipation, (fuchsia curve in FIG. 4.9 and 4.10) the charge rapidly increases linearly beyond what was experimentally measured. Adding static emission simply decreases the rate of charge by a multiplicative factor of $(1-Y)$ (blue curve in FIG. 4.9 and 4.10). As simple Ohmic charge dissipation is added, the fits initially match the data better (green curve in FIG. 4.9 and 4.10); however, the experimental data appears to level off much quicker than simple ohmic dissipation

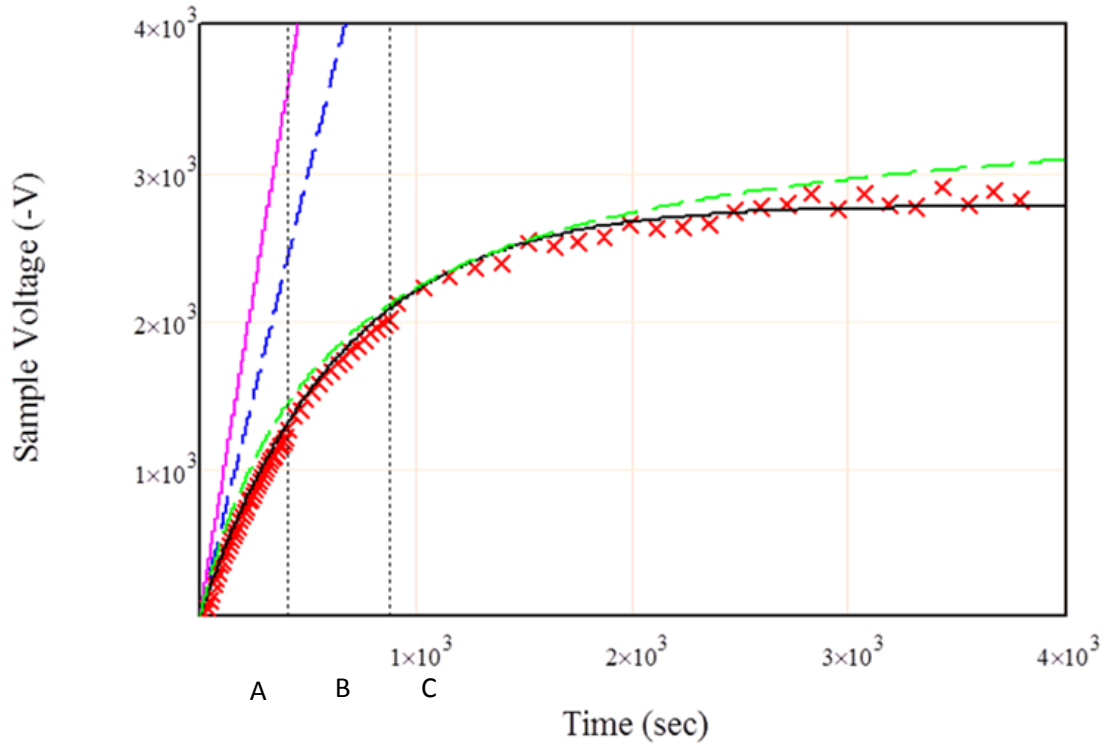


FIG. 4.9. Fits of charge accumulation data for Kapton HN™ plotted versus beam on time. Fuchsia (Eq. 4.9; no dissipation, no emission), blue (Eq. 4.10; no dissipation, static emission), green (Eq. 4.22, ohmic dissipation using conductivity down as a fitting parameter, static emission), and black (Eq. 4.33, nonohmic dissipation, static emission). Regions A, B, and C have t_{on} equal to 10 s, 30 s, and 120 s, respectively.

predicts. By adding the effects of nonohmic charge dissipation, the fits became the most representative of the data (black curve in FIG 4.9 and 4.10).

The number of traps for LDPE determined from the best fit agrees with CVC results reported by Brunson (2010). For Kapton HN™, the number of traps from the best fit are two orders of magnitude higher than what Weingart *et al.* (1972) report. This discrepancy could be caused by the different charging scenarios in the test matrix (Table 4.3), or the way the data were analyzed. These data were taken with three different charge pulse times (10 s, 30 s, and 120 s). The first set of pulses taken at 10 s had ~70 s measurement times. After ~3600 s of charging time the pulse was changed to ~30 s with ~70 s measurement time for 1600 s. Finally, the charge was

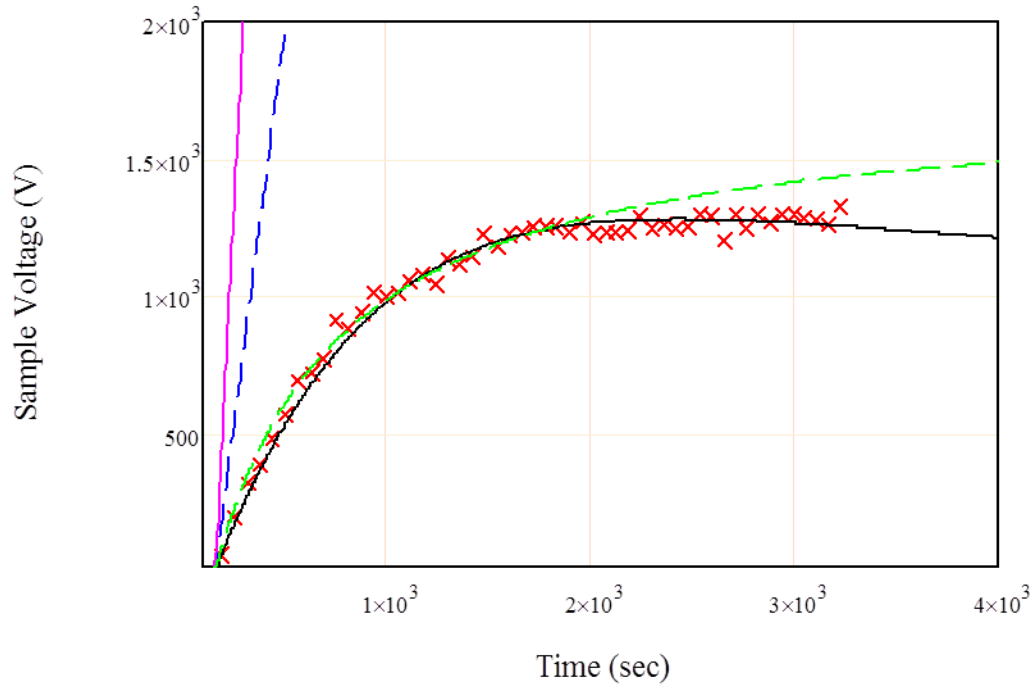


FIG. 4.10. Fits of charge accumulation data for LDPE . Fuchsia (Eq. 4.9, no dissipation, static emission), blue (Eq. 4.10; no dissipation, static emission), green (Eq. 4.22, ohmic dissipation with the conductivity down as a fitting parameter, static emission), and black (Eq. 4.33, nonohmic dissipation, static emission).

TABLE 4.3. Timing scenarios of beam charging runs on Kapton HN™ accumulation. The decrease in the normalized percentages between the fraction of charging times and filled traps suggest a saturation point may have been met.

Beam on Time per pulse (s)	Average total time per pulse (s)	Number of Pulses	Running time (s)	Fraction of Charging Times		Filled Traps	
				Ratio	Normalized	N_r Traps/cm ³	Normalized
10	79	40	3400	0.13	100%	0.85×10^{20}	100%
30	100	17	5000	0.30	230%	1.77×10^{20}	210%
120	186	24	9470	0.65	485%	1.95×10^{20}	230%

allowed to come to equilibrium by charging it with ~120 s pulses with ~70 measurement time. All together, this took ~4500 s. To analyze this set of data, in FIG. 4.9, we took the beam on time as the running time, ignoring the time it took to make measurements. It is believed this method of analyzing the data will skew the number of traps in the system used as fitting parameters. Figure 4.11 shows the data plotted against the actual running time. Three fits were made for each of the

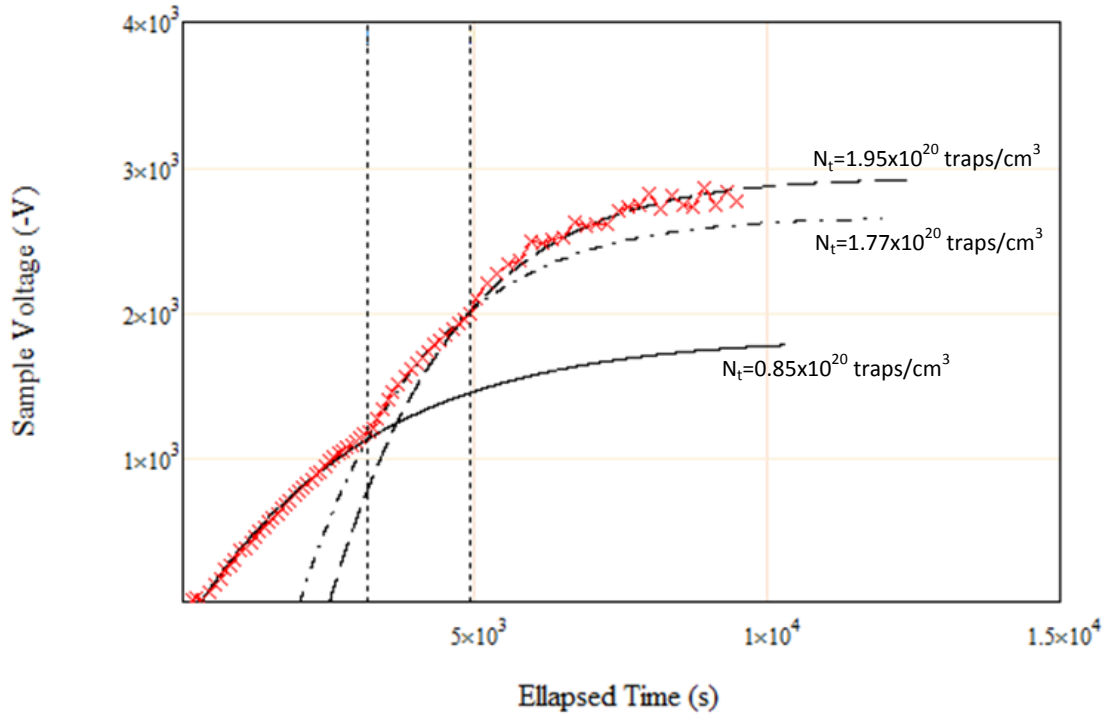


FIG. 4.11. Fits of charge accumulation data (Eq. 4.33) vs. elapsed time for Kapton HNTM. Data (red) is total elapsed time. Solid line fits the data with a 10 s charge up time, dots fit the data with a 30 s charge up time, and the dashed line fits the data with a 120 s charge up time. All parameters were held constant with the exception of number of traps.

different pulse times. The fitting parameters were held constant with the exception of the number of traps. As the ratio of beam time to total time increases, so does the number of traps. Higher levels of filled trap states should be expected for higher ratios of beam time to total time, as there is less time for charge to dissipate.

For Kapton HNTM we found the equilibrium conductivity to be $\sigma_0 \sim 5.0 \cdot 10^{-20} (\Omega\text{-cm})^{-1}$, which is close to independent room temperature dark current conductivity of $1 \times 10^{-20} (\Omega\text{-cm})^{-1}$ provided by Weingart *et al.* (1972) and $1.7 \times 10^{-19} (\Omega\text{-cm})^{-1}$ measured with a charge storage method. For LDPE we found σ_0 to be $1.45 \times 10^{-18} (\Omega\text{-cm})^{-1}$, which shows great agreement with the time independent room temperature dark current conductivity measured by Brunson of $1.38 \times 10^{-18} (\Omega\text{-cm})^{-1}$ (Brunson, 2010). The dispersion and diffusion parameters are not commonly

found in the literature, which lists a wide range of values covering a wide spectrum of possibilities. These experimental values fall within these ranges; however, not much information can be extracted from these results. However, a relative comparison of the parameters provides useful information. For example LDPE is not as diffusive in nature, whereas Kapton HN is less dispersive.

The results for both LDPE and Kapton HNTM are very encouraging and suggest a complete description of electron beam charging of polymeric materials may soon be achieved. Future experiments will address the wide range of reported results of the dispersion and diffusion parameters, as well as look into the discrepancy of the reported number of traps.

4.3.2. Charge Diffusion

Equation (4.56) was used to fit the data taken for both Kapton HNTM (FIG. 4.12) and LDPE (FIG. 4.13), again using the same fitting parameters as the charge accumulation models. Assumption b) states the fits are not valid past the transit time. The measurements taken for both LDPE and Kapton HNTM extended past the transit time. We can estimate this transit time to be the point at which the fit is no longer valid and compare values with those found in literature. For LDPE the decay fit fails at ~5000 s (this is total time including the charging run). Literature results show the transit time is approximated as $\frac{\sigma_{disp}}{\epsilon_0 \epsilon_r} < \frac{1}{t_{transit}} < \frac{\sigma_{DC}}{\epsilon_0 \epsilon_r}$. For LDPE this gives a range of transit times of 70 s to 2×10^5 s. Results from Toomer estimate the transit time on LDPE as ~1900 s. (Toomer and Lewis, 1980). For Kapton HNTM the transit time is estimated from the fit as 2×10^5 s where the range of transit times can be from 700 s to 3×10^6 s. This is about a factor of 50 higher than LDPE, which is expected from a similar magnitude difference in dark current conductivities.

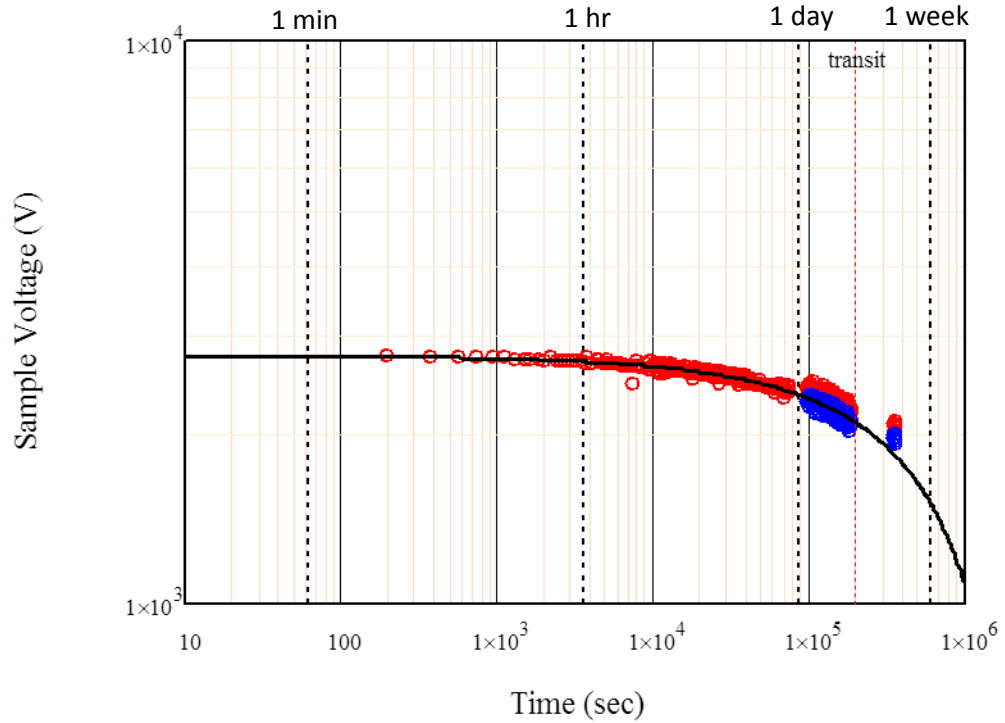


FIG. 4.12. Fit of charge decay data for Kapton HN™ with nonohmic conductivity (Eq. 4.35). Red line is the data collected during decay measurements, blue data represents data shifted for misalignment of the stage and the HGRFA, black line is the fit produced using Eq. 4.35, and vertical dashed red line is the point at which the fit becomes unstable. This is estimated as the transit time and is 2×10^5 s (this value includes the charge up time).

The Kapton HN™ (FIG. 4.12.) run shows a possible error due to position misalignment when returning to a sample. The experiment consisted of moving the HGRFA off the sample and later returning to continue surface voltage measurements. In Chapter 2, it is estimated the centering of the carousel could be off by 1 mm from the center of the sample. Section 4.5 goes into a radial profile of the sample charge based off positioning of the probe and shows a 1mm change in sample location can result in as much as a 10% change in charge. The fit for the Kapton HN™ suggests when returning to the sample to continue measurements, the sample is not positioned at the same location, thus resulting in a 5% increase in sample voltage (4% change shown in blue). Improvements could be made to the sample carousel mounting system to decrease this uncertainty if this 5% error is unacceptable.

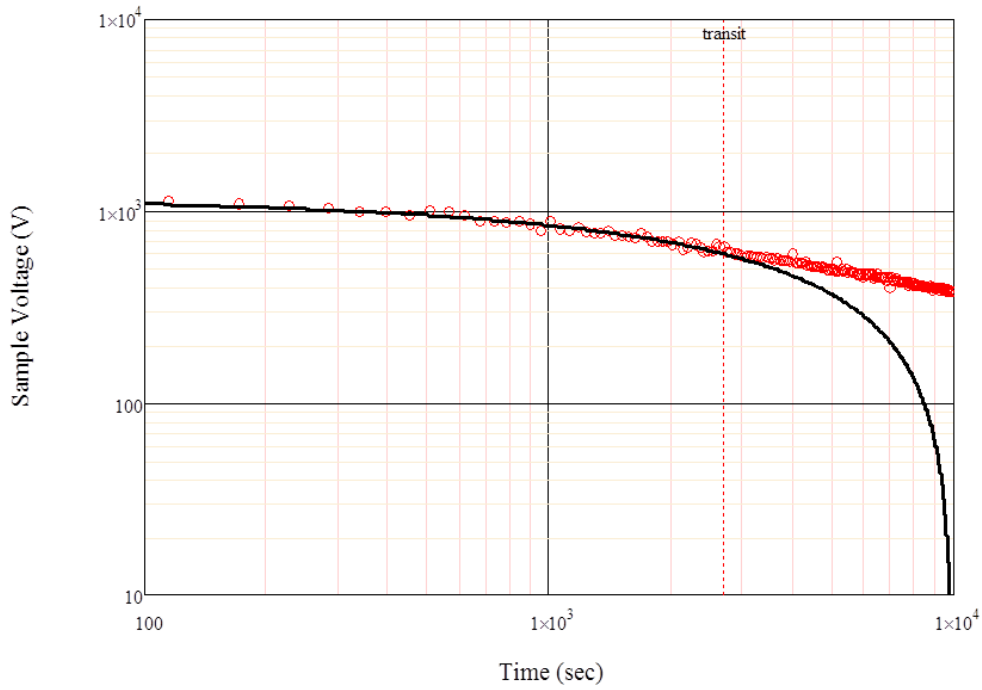


FIG. 4.13. Fit of charge decay data for LDPE with nonohmic conductivity (Eq. 4.35). Red line is the data collected during decay measurements, black line is the fit produced using Eq. 4.35, and vertical dashed red line is the point at which the fit becomes unstable. This is estimated as the transit time and is ~ 5000 s (including the charge up time).

4.3.3. Fits to Electrostatic Discharge Observations

An alternate mechanism that acts to limit the potential a material can achieve is electrostatic breakdown. If the adopted potential is greater than the dielectric breakdown strength of the material, electrons will arc to some adjacent element or burn through the bulk of the material. This results in irreparable structural damage to the material and can greatly reduce the ability for it to store charge. The reduced ability to store charge is seen in FIG. 4.14. Continuous charging of a material resulted in an electrostatic discharge of the material. This discharge was seen as a sharp spike in voltage measured by the SVP at ~ 1400 s. A confirmed breakdown was present when continued charging resulted in no sustainable voltage and no net gain of charge beyond ~ 1700 s. The LDPE sample tested broke down at much lower values ($\sim 50\times$) than measured by the ESD chamber (Sim *et al.*, 2010). However, measurements in the electrostatic

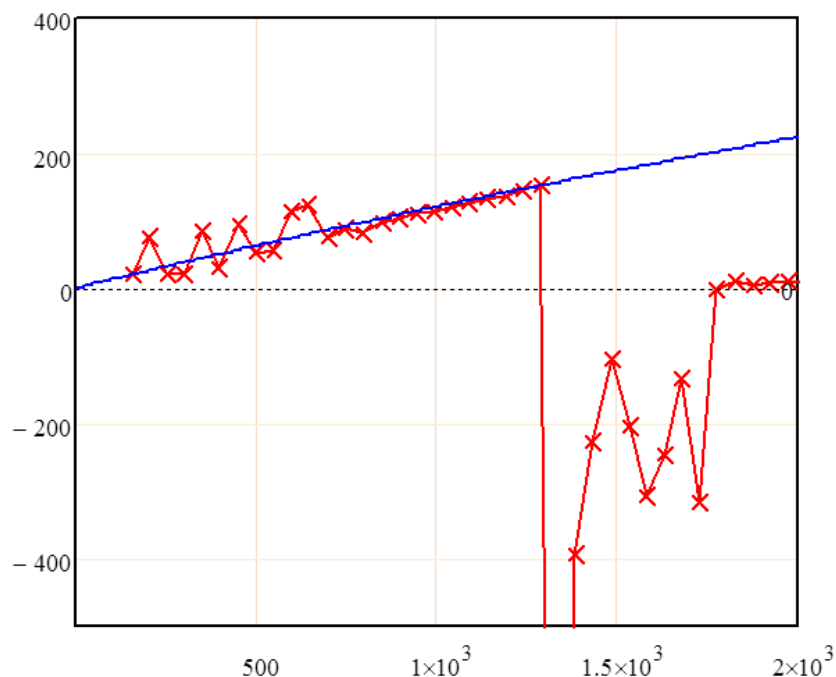


FIG. 4.14. Charge accumulation and subsequent breakdown of an LDPE sample. Blue line shows the expected charging profile and red data shows a large spike in voltage at ~ 1200 s. Continuous charging was attempted until ~ 1700 s. When charging was halted the sample voltage measured was 0 V. Red data points show a possible problem in positioning during the first 10 measurements see Section 4.4.

discharge chamber have shown materials can break down at very low potentials; these samples tend to have flaws or other abnormalities that cause a shorter discharge path (Sim *et al.*, 2010). The result here shows how the SVP reacts to ESD events, and that these events are clearly identifiable with the SVP.

4.4. Fits to Radial Charge Diffusion Data

An experiment was performed to measure the time evolution of the radial charge profile of a sample irradiated with an electron beam. An evolution of the shape of the charge profile would be indicative of radial diffusion of the charge laterally across the sample surface. A constant radial charge profile with decreasing amplitude similar to that measured in Section 4.2 would indicate the charge dissipation through the sample was the dominate process.

Figure 4.15 shows the decay of the peak voltage of each radial profile measurement. After ~60 s of cumulative irradiation, the sample charge reached a peak voltage of $-(1456 \pm 5)$ V. The peak voltage values decayed over the following 24-hr period. The technique discussed in Section 4.2 was used to fit the data with results shown in TABLE 4.4. The peak values of each radial profile were extracted and plotted on a voltage vs time graph, then fit using the method discussed in Section 4.2 (FIG. 4.15). These results are compared to those of Section 4.3.2 and show the radial decay collection method is a valid method, which produces expected results.

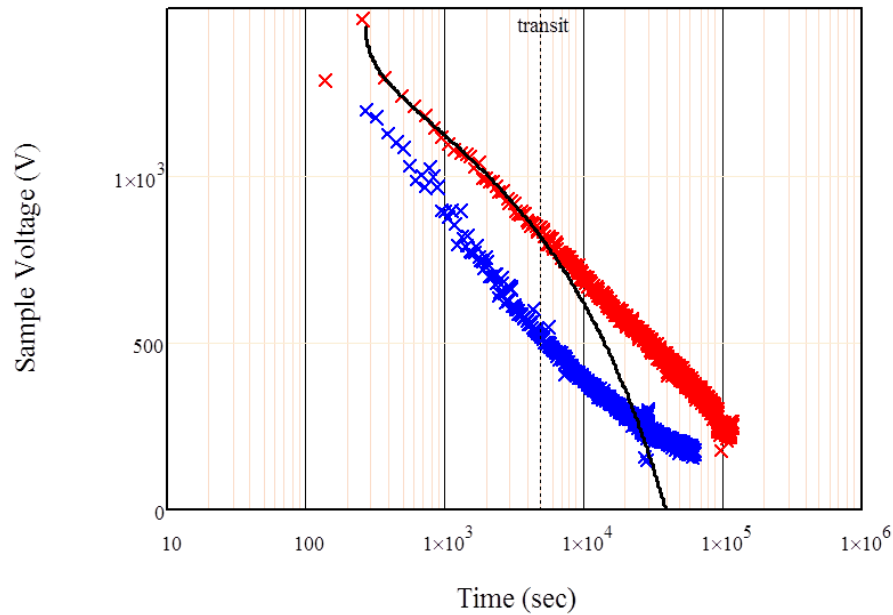


FIG. 4.15. Decay of the peak voltage during radial profile measurements on LDPE (red) with nonohmic dissipation fit (black). Data (red) of the peak voltage during a radial profile measurement was fit using Eq. (4.36). Data from charge decay methods outlined in Section 4.3.2 (blue) is plotted as a comparison of the two measurements.

TABLE 4.4. Comparison of decay measurements for peak radial decay and voltage decay curves on Kapton HN™.

Material Type	σ_0 ($\Omega\text{-cm}$) ⁻¹	σ_{diff} ($\Omega\text{-cm}$) ⁻¹	σ_{disp} ($\Omega\text{-cm}$) ⁻¹	α	V_0 (V)
LDPE	1.45×10^{-18}	1.45×10^{-18}	1.9×10^{-15}	0.5	1204
LDPE (radial)	1.45×10^{-18}	1.45×10^{-18}	1.05×10^{-14}	0.3	1468

With confidence, the method of measuring the radial profile did not affect the charge diffusion through the sample, and analysis of the rate at which the charge decayed radially could be investigated. Recall from Section 3.6 the expected radial profile was a convolution produced by sweeping a radial step function, representing the electrode, across another radial step function, representing the conducting sample. In a similar manner, a Gaussian profile caused by the electron beam was convoluted with the step function representing the electrode. The beam profile from the USU MPG electron gun has been carefully measured and characterized by Hoffmann (2010); for the given beam parameters used in this experiment, the beam has a measured full width at half maximum of 5.6 mm. Using this beam profile, a plot comparing the measured profile versus the calculated surface voltage profile can be made. Figure 4.16 shows the normalized radial profiles of the surface voltage at four times [FIG. 4.16 (a) 265 s, (b) 1170 s, (c) 5630 s, (d) 7.93×10^4 s].

The measured voltage profile was equal to a Gaussian profile with a FWHM of 6.7 mm, approximately 1.1 mm wider than the incident electron beams measured FWHM. Over time this profile did not change, indicating there was no measurable radial diffusion over the course of the measurement after the initial profile was measured 265 s from when the charge deposition began. This result suggests if diffusion occurred, the majority of the radial diffusion happened during the 265 s when the charging of the material was taking place. During this period, conductivity in the region between the surface and the finite depth of the deposited charge, at range R , becomes enhanced; this is known as the radiation induced conductivity (RIC) enhanced region. The enhancement of the conductivity, σ_{RIC} , due to the RIC region allows the radial expansion of the charge and in turn the surface voltage charge profile as given in Hoffmann (2010). To model the effects of RIC on radial transport in this initial time period, we must digress to summarize the magnitude and time evolution of RIC in LDPE. RIC is typically expressed as a power law of dose rate, with temperature dependent material parameters $k_{ric}(T)$ and $\Delta(t)$ (Corbridge *et al.*, 2008).

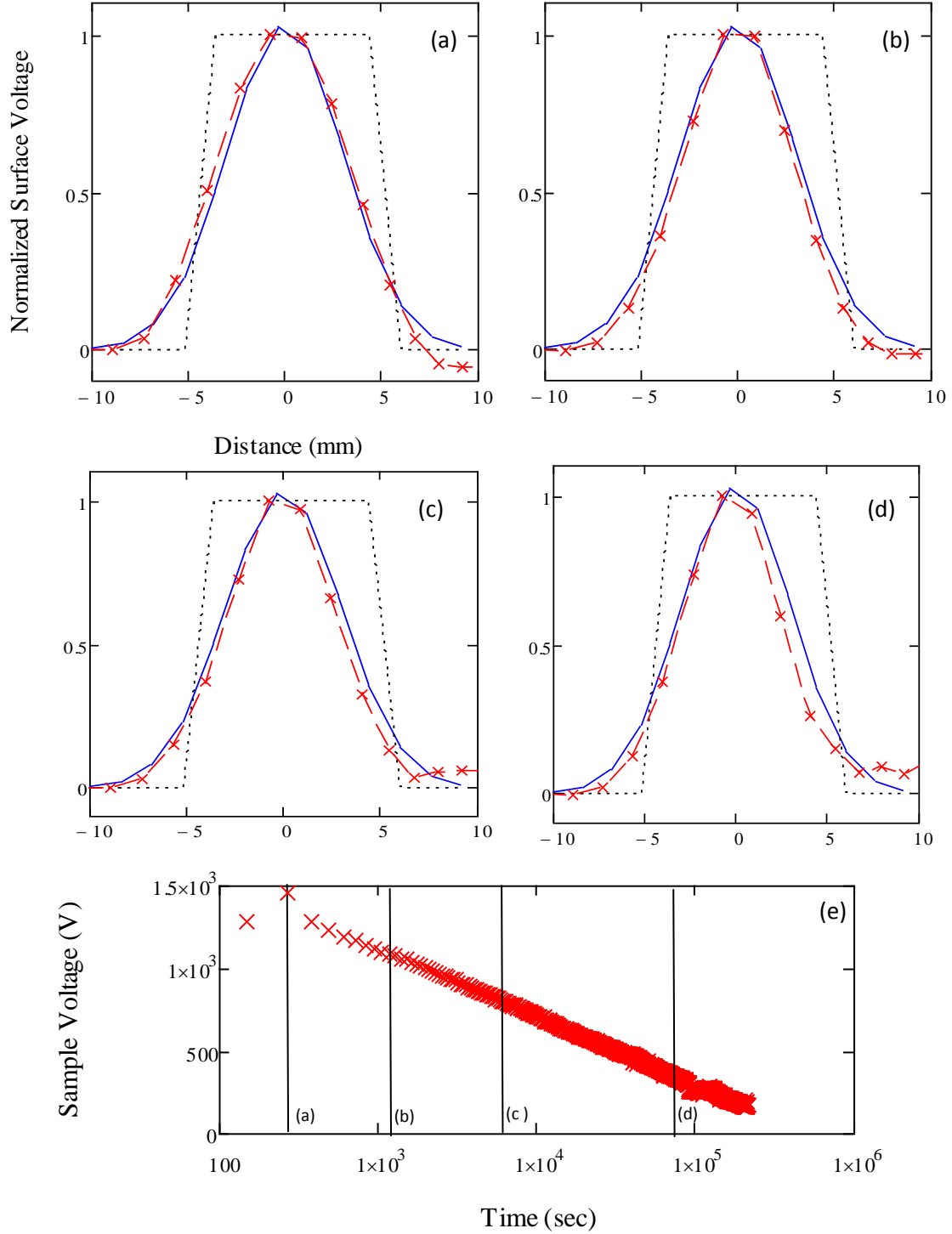


FIG. 4.16. Radial profile vs. position at several times during decay measurements of LDPE. (a)-(d) black line represents sample diameter, blue line represents normalized expected voltage profile of gaussian beam measured by the SVP, and red line represents normalized measured data at given times (a) 265 s, (b) 1170 s, (c) 5630, (d) 7.93×10^4 s. (e) Peak voltage decay with vertical markers showing the points of radial profile.

$$\sigma_{RIC}(\dot{D}) = k_{RIC}(t)\dot{D}^{\Delta(t)}. \quad (4.37)$$

The dose rate due to irradiation goes as

$$\dot{D} = \frac{E_b J_o}{R_{qe} \rho_m}. \quad (4.38)$$

The dose rate is $9.96 \times 10^3 \frac{\text{rad}}{\text{s}}$ for the 5 keV, 1.1 nA/cm² beam used with a range of 0.6 μm FIG. 4.3 (Wilson and Dennison, 2010). For LDPE, from studies done by the USU MPG at the Idaho Accelerator Center, k_{ric} is given to be $1.5 \times 10^{-16} \left(\frac{\text{rad}}{\text{s}} \Omega - \text{cm} \right)^{-1}$ and $\Delta(t)$ is 0.85 (Corbridge *et al.*, 2008). Therefore, the enhanced conductivity due to RIC is $\sigma_{RIC} \cong 3.8 \times 10^{-13} (\Omega - \text{cm})^{-1}$, which is $\sim 3 \times 10^5$ times greater than the measured dark conductivity from Section 4.2.

It is possible to determine a rough estimate of how the charge will move radially through the sample. Taking the transit time from the dark conductivity measured in Section 4.2, one can find an estimated drift velocity of the charge moving through the material of thickness D ; $V_d = \frac{D}{\tau_d} \approx \frac{D \sigma_{DC}}{\epsilon_o \epsilon_r}$ is 0.129 nm/s. Since the conductivity of the RIC enhanced region is $\sim 3 \times 10^5$ times greater than the dark conductivity region, it can be estimated the charge can move radially through the sample at a speed of 39 $\mu\text{m/s}$ in this region. At this speed it is expected the charge over the 265 s (the time until the first radial profile decay measurement) would expand to approximately ~ 34.2 mm, which is well beyond the edge of the sample. However, the RIC enhanced region will not have its full effect over the entire time. To calculate the average enhanced conductivity σ_{RIC} during the two charging pulses we must estimate the natural rise of conductivity during charging and its decay when the beam is turned off. Data for LDPE, taken at the Idaho Accelerator Center, show two methods of charging and decays of σ_{RIC} , a fast and a slow decay (FIG. 4.17) can be seen (Corbridge *et al.*, 2008). The fast decay has a quick initial drop

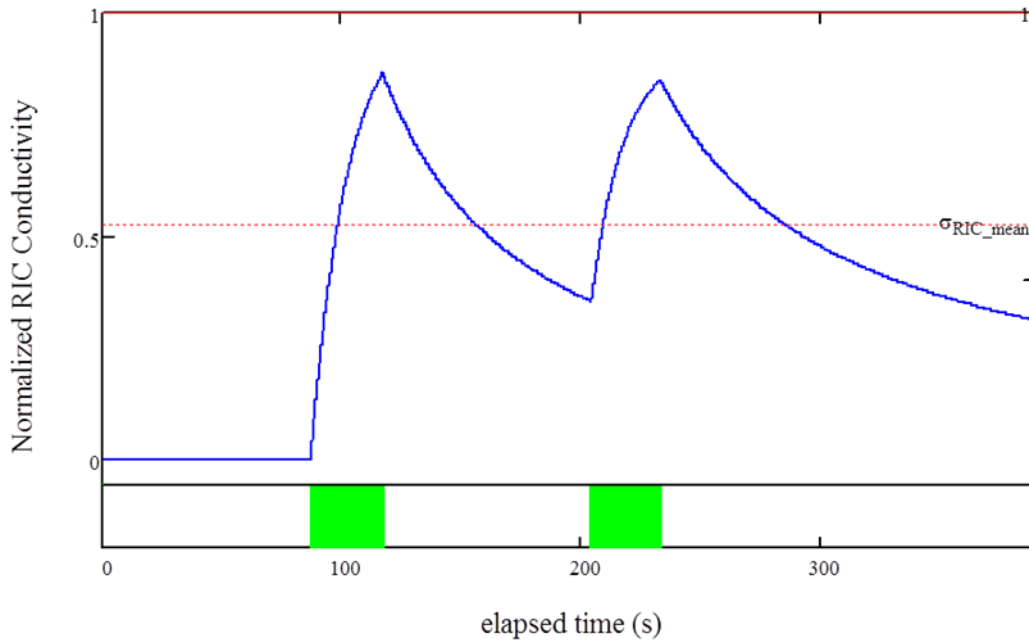


FIG. 4.17. Estimated change in conductivity during radial profile measurements. Green bars represent beam on time, Blue line is representative of the estimated RIC conductivity during charging measurements, and the red line represents the average conductivity over the course of the measurements.

$\ll 10$ s. This is an abrupt drop and is estimated at about 30%, the peak conductivity. The second decay has a much longer hyperbolic decay. Fits from Sim and Corbridge show a time constant of ~ 220 s. Figure 4.17 shows the estimated profile of the normalized conductivity; simply integrating over this curve and dividing by total time give a mean value for σ_{RIC} (Eq. 4.39).

$$\sigma_{RIC\text{mean}} = \frac{\int_{t_{on}}^{t_{max}} \sigma_{RIC}(t) dt}{\int_{t_{on}}^{t_{max}} dt}. \quad (4.39)$$

This result says the expected charge will move 0.53 times slower than the maximum velocity of $39 \mu\text{m/s}$. This result gives the spread of charge to be 18.1 mm , still beyond the diameter of the sample, so no change in spatial profile should have been expected. The agreement based on, what is at best a first order analysis, does not confirm what is physically occurring; it

merely adds strength to the argument. Further testing is required to determine how the charge moves radially and whether the ideas behind this analysis are what occur physically.

The final calculation that can be made from these measurements is an expected maximum initial voltage based on the charging of the material. Assuming a perfect charge integrator in a parallel plate capacitor configuration, the maximum attainable surface voltage, excluding both electron emission and charge dissipation, is 868 V (see Section 4.1 EQ 4.4). Ignoring electron emission and charge dissipation, which in this case both help to reduce the total charge on the sample, the sample in this experiment appears to charge significantly more than expected. This should be of concern as, for an unknown reason, LDPE charged approximately two times greater than was to be expected.

One explanation for the higher than expected charge profile could be in conjunction with the tail on the right side of the voltage spatial profile [FIG. 4.16 (d) and FIG. 4.18]. After experimentation, it was found the inner grid became ungrounded during measurements, thus creating a floating conductor around the entire probe. It is expected the large effect of this floating conductor is not seen on the left side of the measurement because the large electrode is the furthest electrode from the inner grid at that point. This problem has since been fixed and could very well be a factor in the reason the sample appears to have charged much higher than expected.

Another lesson, which became largely visible in FIG. 4.18, is neglecting the voltage drifts that are discussed in Section 3.4 can be detrimental to the radial profile. For higher voltages, there are large impacts in radial profile measurements. For radial measurements a simple voltage correction is difficult, as the voltage varies as the probe moves over the sample. A more detailed algorithm is needed in order to properly correct for the voltage drift. These errors can be seen in the first few measurements of FIG. 4.18 when the voltage is large (larger voltage drifts) making the tailing end of the measurement not return to 0 V when expected.

A few of these errors are of concern, but an initial pass of the experimental system looks good. Simply overlooking the value at which the beam was charged to or missing a charge up run time can swing the numbers drastically in the favor of the experimenter. Further experimentation is required to determine experimental feasibility.

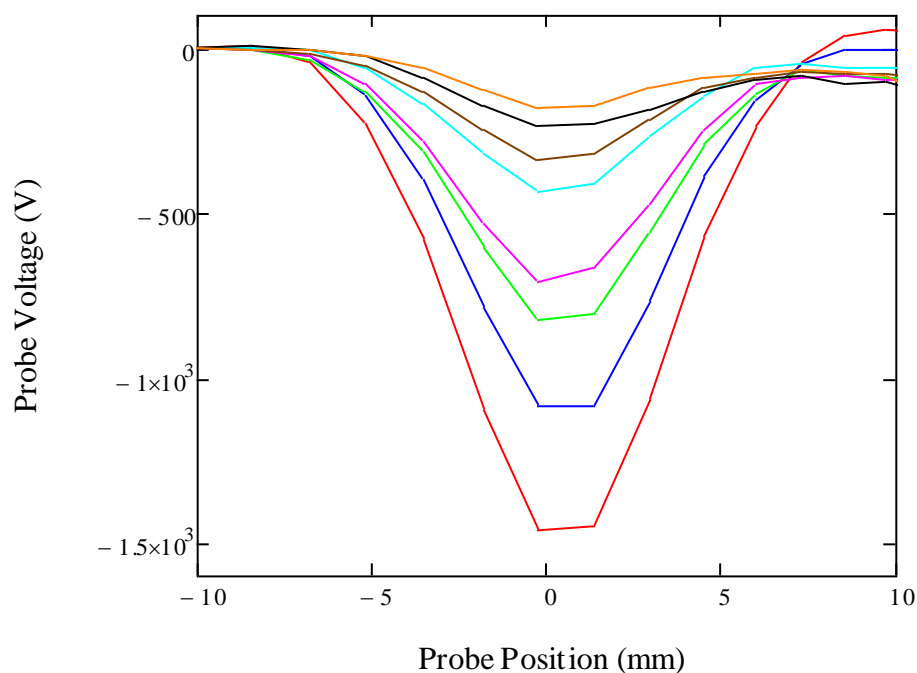


FIG. 4.18. Radial profile of LDPE at several times. The red and blue curves have higher peak voltages. A discrepancy can be seen when the probe position reaches 5mm. Since the voltage was not corrected for voltage drifts, the larger peak voltages experienced a greater drift causing the tail end of the measurements to be slightly shifted. (Red) 145 s, (blue) 1170 s, (green) 5.6×10^4 s, (pink) 1.1×10^4 s, (cyan) 4.6×10^4 s, (brown) 7.9×10^4 s, (black) 1.41×10^5 s, (orange) 2.14×10^5 s.

CHAPTER 5

CONCLUSIONS AND FUTURE WORK

5.1. Conclusions

This thesis presents the design, implementation, and testing of a surface voltage probe with capabilities that extend far beyond the initial scope of the project. An instrument, described in detail in Chapter 2, was designed and built to measure the surface voltage *in situ* in an ultrahigh vacuum chamber. The new instrument is compact enough to fit inside the primary electron detector HGRFA assembly without inhibiting its capabilities. This combination has allowed for simultaneous high-precision and high-accuracy measurements of incident, emitted, dissipated, and stored electrons. This capability opens the possibility for a myriad of tests of critical spacecraft charging applications and fundamental studies of material properties, electron transport, and emission phenomena.

Detailed characterization and calibration measurements presented in Chapter 3 have established the capabilities of the system. The maximum voltage range of the large electrode, >10 kV, allows testing of surface voltages in thin film samples of up to $\sim 10^{-4}$ m at typical electrostatic breakdown fields of $\sim 10^8$ V/m. The small electrode extends this maximum surface voltage range more than an order of magnitude to $\sim 1.5 \times 10^5$ V or a sample thickness of >1 mm at typical breakdown voltages. It is expected the actual maximum surface voltage will be limited to <30 kV due to discharge from the sample to the sample holder or similar effects. Additional work is required to refine the calibration of the small electrode.

The voltage resolution of the large electrode is ~ 0.2 V with a minimum voltage measurement of ~ 1.1 V, these voltages are approximately two orders of magnitude lower than other systems used to measure surface voltages for spacecraft charging applications (Swaminathan, 2004). This allows high-precision measurements even at relatively low surface voltages. The small electrode has voltage resolutions of ~ 3 V with a low-voltage range of ~ 15 V,

due to its decreased voltage sensitivity. The resolution was determined and minimized through a detailed set of measurements outlined in Chapter 3. At higher sample voltages, above 5 kV, the absolute resolution was limited to $\sim 0.5\%$, driven primarily by uncertainties in the reproducibility of the calibration factor that determines the linear response of the surface voltage probe to a given sample surface voltage.

Additional uncertainties due to the electrostatic field probe electronics, temporal drift of the transfer probe ground due to charge accumulation, and temporal drift of the transfer probe, voltage due to the response of the polarization and dissipation of charge on the transfer probe were investigated. The primary sources of uncertainty were observed in the offset voltage and temporal drifts of the transfer probe. An automated procedure was established to perform *in situ* calibration of the transfer probe offset, ground drift rate, and ground drift decay time. By performing these *in situ* calibrations, it was determined for time intervals of less than ~ 200 s, the instrument resolution for low voltages was 0.2 V for the large electrode, and 3.0 V for the small electrode.

The primary factors in these offsets and drifts were determined to be through the capacitance of the transfer probe connector wires and the vacuum feedthrough, as well as the resistance across the air gap between the EFP and the witness plates, the isolation resistance through the sapphire spheres, and the isolation resistance of the vacuum feedthrough. The magnitude and relative importance of these factors were confirmed through the calibration measurements. To further reduce the uncertainties associated with a single low-voltage measurement, a computer-controlled algorithm was developed to acquire multiple voltage measurements and determine a mean value and a standard deviation of the mean. Taken together, all these error reduction procedures reduced the low-voltage uncertainty of the SVP to 0.2 mV, a value limited largely by the inherent voltage resolution and response time of the SVP, and by the voltage resolution of the 16-bit DAQ card used for data acquisition.

The response time of the instrument met the set design goals. These were set from a practical point of view as the shortest time for significant changes to take place on spacecraft surfaces in response to temporal changes in the space environment. A minimum spacecraft response time was estimated to be on the order of a few seconds due to satellite rotations, or to transit of a shadow across a spacecraft surface. Such times correspond to charge decay times of typical dielectric materials with conductivities as low as $10^{-12} (\Omega\text{-cm})^{-1}$ to $10^{-13} (\Omega\text{-cm})^{-1}$, materials that are no longer classified as good insulators. The response time for a single voltage measurement is set by the response time of the EFP, ~50 ms. The time to acquire a set of surface voltage measurements for statistical analysis is at present 1 s. Thus, if required, a tradeoff between ~100 ms and 1000 ms could be chosen to match applications requiring rapid data acquisition.

Another critical response time is the time required to make the initial surface voltage measurement. This is limited to ~7 s, the time required to perform an *in situ* drift calibration over an adjacent grounded surface and then move over the sample. The measurement of ground drift calibration data and the motion of the probe contribute to this wait time. This time can be reduced for certain applications where rapid data acquisition is required; however, the consequence of this is to increase in uncertainty of the ground drift measurements. In addition, these *in situ* drift calibrations need to be performed at <200 s intervals, limiting the maximum long-term data collection coverage to 94% of the time the charge is on the sample. While the current instrument capabilities meet the response time requirements for spacecraft applications, reduced response times would extend studies of basic material properties, such as the polarization response time or response to more discrete charge deposition pulses. Efforts continue to reduce the response time; reduction by a factor of 2-3 seems plausible.

Through a combination of low-resolution and automated *in situ* drift calibration, the instrument has fully met any reasonable design goal for long-term stability. The desired stability

was set by need to measure decay times for very good spacecraft insulators; for measurements of ~10% voltage decay of a typical dielectric with an extremely low conductivity of $10^{-20} (\Omega\text{-cm})^{-1}$, this requires stable measurements on the order of one month. Continuous measurements were successfully conducted on a single sample for ~one day, with periodic automated *in situ* drift calibrations at ~100-s intervals. Furthermore, it was shown that the SVP and HGRFA could be moved off a specific sample and later returned to that sample several days later to continue surface voltage measurements after another *in situ* drift calibration. From a practical point of view this means surface voltage measurements can be performed simultaneously on a set of ~10 samples in the sample carousel for as long as it is practical to dedicate the electron emission chamber to such measurements.

Precision motion of the SVP *in vacu* has been demonstrated using the UHV compatible compact stepper motor mounted on the HGRFA detector face plate. The resolution of the positioning probe is $\pm 25 \mu\text{m}$. Some limited problems of reproducibility of the absolute position of the probe, most likely due to insufficiencies in the software feedback, have been identified and are currently being addressed.

Useful measurements of lateral variations of surface charge distributions from a sample charged with an electron beam that has a Gaussian beam profile are possible. Measurements have shown the maximum radial spatial resolution is $\pm 3 \text{ mm}$ for the large electrode and $\pm 1.5 \text{ mm}$ for the small electrode. Work continues on better calibration measurements and with better signal deconvolution algorithms to improve the spatial resolution of the system. These tests should show improvements on the spatial resolution with a decrease in the maximum resolution expected to be by a factor of at least three.

Three types of experiments were conducted using the new instrumentation to illustrate the research capabilities of the system. These were measurements of charge accumulation induced by an incident electron beam, charge dissipation through a thin film, and radial profiles

of surface charge layers. The experiments were made on thin films of two prototypical polymeric spacecraft materials, low-density polyethylene (LDPE) and polyamide (KaptonTM HN). Section 5.2 provides brief outlines of numerous extensions to these measurements designed to further extend the instrument's capabilities and to explore additional materials and physical processes related to charge storage, electron transport, and electron emission.

The charge accumulation data presented in Section 4.3.1 demonstrated the probe can measure small increases in surface voltage due to a charged electron beam. Charge was accumulated on the sample using pulsed and continuous monoenergetic electron beams with a range of pulse amplitudes, widths, and duty cycles. Instrumental resolution allowed measurement of charge densities as low as 10 to 100 pC/cm² (10^7 to 10^8 electrons/cm²) for LDPE and Kapton HNTM samples, respectively. The charge accumulation was measured on three samples. These samples charged up according to models presented in section 4.2. And similar to models developed by (Gross *et al.*, 2003; Liufu *et al.*, 1998; Montanari *et al.*, 2001; Sessler *et al.*, 2004; Wintle, 1977). The fitting parameters for the charging models of LDPE lead to predictions for the dark current conductivity, as well as information regarding diffusion and dispersion rates. The conductivity values are within the range of values reported in the literature, and the dispersion and diffusion information agrees with what is expected from the materials. Measurements of LDPE showed the signature of an electrostatic breakdown demonstrating the potential utility of the SVP during induced electrostatic breakdown measurements.

The charge decay data presented in Section 4.2 demonstrated the SVP is capable of measuring long-term voltage decay with <5% uncertainties up to the transit time of the material. Remarkable results were obtained given conductivity results of LDPE 1.45×10^{-18} Ω-cm and Kapton HNTM 5.0×10^{-20} Ω-cm that match both literature results and experimental results (Aragonas *et al.*, 2008; Brunson, 2010; Dennsion *et al.*, 2009). These tests showed that the new instrument can be used in a similar manner to the charge storage chamber (Swaminathan, 2004) if

an increased error of 5%, due to the positioning of the detector over the sample, is tolerable or can be minimized.

The radial measurements of surface voltage described in Section 4.3 showed the capability of the SVP to measure the radial surface charge profile of the sample with <3 mm resolution. Measurements of the surface voltage profile after irradiation of a 10 mm diameter 24 μm thick film samples with a ~ 5 mm full width at half maximum (FWHM) Gaussian beam profile found an initial surface charge distribution with a similar Gaussian shape and a ~ 6.7 mm FWHM, which was 30% larger than the measured beam width. Measurements for ~ 24 hr of dissipation showed the charge density profile remained constant to within the instrumental resolution and the overall magnitude of the charge decayed at a rate very similar to that measured in the charge dissipation experiments. This suggested the charge migrated through the thin film sample to the grounding plane. Charge did not disperse radially over measurable distances from the moment profile measurements commenced ~ 100 s after the beam was turned off. While the experiment did not directly observe radial diffusion of charge, it clearly demonstrated the capability of the new instrument to measure radial charge dispersion if it occurs at timescale faster than charge migration through the thin film sample. Such behavior may occur for particular beam current densities and energies where RIC in the irradiated surface layer is >100 times that of the conductivity in the unirradiated layer between the deposited charge layer and the grounded substrate.

These three types of validation experiments clearly show the new instrumentation facilitates measurements related to charge accumulation, charge transport and dissipation, charged storage conductivity tests, effects of charge on yield measurements, electron-induced electrostatic breakdown potentials, radiation-induced conductivity effects of nonpenetrating radiation, and the radial dispersion of surface charge. The range of possible information and the ability to cross check measurements from nearly all of USU MPG's existing electron emission,

transport, and discharge chambers makes the new SVP the most versatile instrument the group has. It also should greatly enhance the search for fundamental knowledge and facilitate construction of spacecraft better able to survive in the harsh environment of space.

5.2. Future Work

The previous chapters show the effort that went into making this probe and the validity of the data acquired with the instrument. This section focuses on the measurements and SVP upgrades that will improve the instrument and understanding of the material parameters.

5.2.1. Instrumentation Upgrades

While the internal components of the main body of the SVP cannot be readily upgraded or switched out, there are components on the air side of the probe, which should be investigated to achieve better precision and accuracy. The top priority for increasing precision is altering the size of the witness plate. The witness plates can be easily exchanged; reducing the size of the witness plate should significantly increase the SVP resolution. When adjusting the witness plates, care needs to be taken to properly account for edge effects between the EFP and the SVP, which can alter the linearity of the calibration factor. While reducing the witness plate area will not help the resolution for the large electrode (its resolution is controlled by the DAQ card), decreasing the size of the witness plate should significantly reduce the resolution and the low range of the small electrode.

The primary factors determining the voltage drift were identified to be: the capacitance of the transfer probe connector wires and the vacuum feedthrough, the resistance across the air gap between the EFP and the witness plates, the isolation resistance through the sapphire spheres, and the isolation resistance of the vacuum feedthrough. The connector wire, vacuum feedthrough and sapphire isolators have been largely optimized. However, it may be possible to significantly reduce the drift of the system by backfilling the witness plate enclosure box with dry nitrogen

gas. Replacing the air purge line with dry nitrogen will blow dry nitrogen across the witness plate and create a positive pressure in the witness plate enclosure box. Studies measuring the change of conductivity of air due to changes in the relative humidity have shown that a decrease in humidity of 35% can increase the electrical conductivity of air by an order of magnitude (Pawar *et al.*, 2009). By replacing the humid air with dry nitrogen and assuming a linear fit to the data in Pawar *et al.* (2009) holds, one could expect the instrument would see a decrease in conductivity of 2.5 times that of typically low-humidity Utah air. This large decrease in conductivity would result in a decrease in drift from the RC circuit analysis presented in Section 2.3.1.1 of ~30%. This reduction would result in lower resolutions for the small electrode, as well as increasing the time the SVP could be removed from ground to approximately 200 s. Further tests should be performed to confirm this proposed improvement.

Other details in the experimental setup, which can be optimized, are the effects the response time of the Monroe controller and the computer-controlled algorithms have on the results of the experiments (see Section 2.3.1.2 and 3.5). Thus far, tests have been done with the recommended settings of a 50 ms response time. The response time greatly affects drift and error of the system, as can be seen by the graph from the Monroe probe calibration (FIG.5.1). Changes in how the DAQ card acquires and processes the data can also be useful in reducing run time and reducing the error in the system. A standard 1000 Hz sample rate over 1 s of time was used for all experiments and calibration reported here. Altering these parameters could lead to smaller errors and reduced run time of the SVP.

Currently, the spatial resolution of each of the probes is set by the maximum value inside a range of possible resolutions: large probe (3.5 mm to 0.15 mm), small electrode (1.5 mm to 0.28 mm). The test outlined in Section 3.6 suggests the resolution is much lower than the maximum value in these ranges, but further testing is needed to confirm this. Such testing can

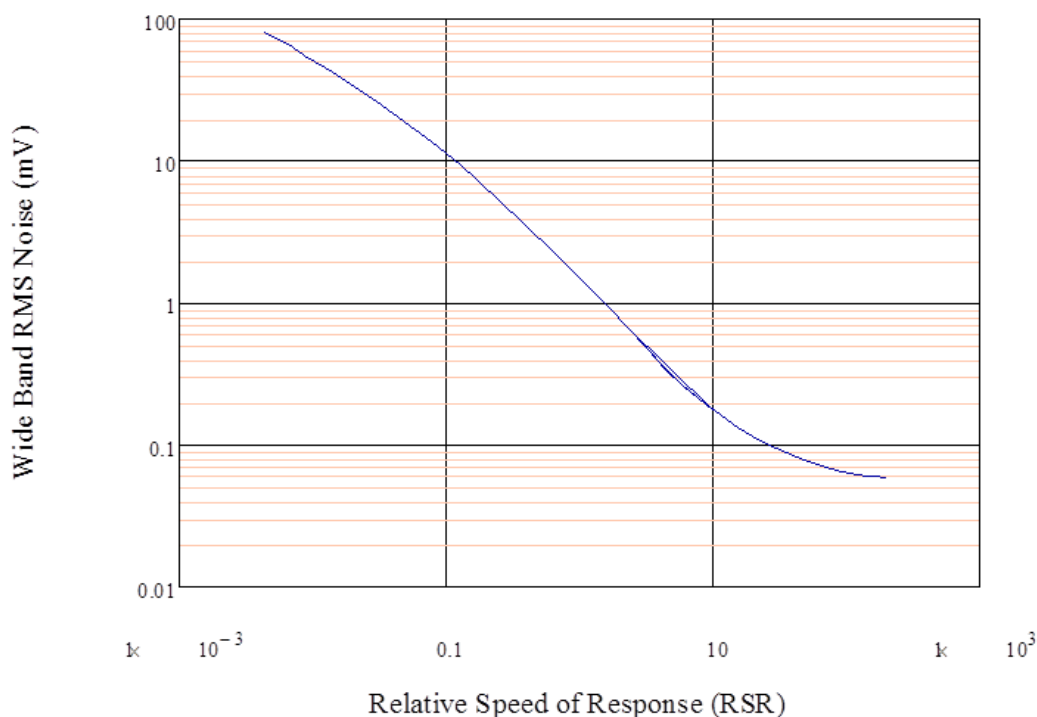


FIG. 5.1. Typical noise vs. speed of response for the Monroe mV probe (Monroe Inc., 1994). Data taken at a probe spacing of 0.762 mm.

include repeating calibration measurements with a small charged electrode and reducing the size of this electrode with grounded guard rings until a suitable radial resolution is found.

Problems with the positioning of the SVP over the system need to be explored to improve stability. The inability to return to exactly the same position on a sample, as demonstrated by the test described in Section 4.2, should be investigated and corrected. This may entail improvements to the positioning VI or to the feedback algorithm used to control the SVP position. Alternately, it may be a consequence of the stability of the electronics associated with the Attocube controller (see Section 4.3.2). Additionally, the positioning system of the HGRFA on the sample carousel should be explored. It was seen during measurements in Section 4.2 that movement of the HGRFA to and from a sample produced results 6% higher than expected. Subsequent testing showed this could easily be caused by a misalignment of the HGRFA.

Evaluation of features associated with the back of the SVP needs to be accomplished.

These include careful calibrations of the Faraday cup and Au SEE standard, and exploration of the effectiveness of blanking the sample. A simple, yet effective, test can be performed while the SVP Faraday cup or Au SEE standard is centered on the Faraday cup mounted on the sample carousel. With the beam running, monitoring the current from the blanked Faraday cup mounted on the carousel will give insight into how much charge the sample is exposed to while it is blanked. A more extensive test can be done with the Faraday cup or Au SEE standard centered over an insulating sample while bombarding the SVP with pulses from the electron beam and monitoring the surface voltage increase. Ideally, no change in surface voltage should be seen from pulse to pulse if the SVP is effectively blanking the sample.

The effectiveness of UV flooding to neutralize negative surface charge accumulation should be investigated by performing a series of charge dissipation experiments similar to those in Sections 4.2 and 4.3. UV flooding is used to induce the photoelectric effect and dissipate negative surface potential on a charged sample. This capability has been used in previous measurements, but time constraints made proper validation unfeasible. To ensure these methods of discharging the sample are useful, an insulating surface should be charged to various negative voltages with an incident electron beam. A series of alternating surface voltage measurements and pulsed UV exposures should be conducted to determine the effectiveness of the UV discharge. Information, such as time to discharge and surface voltage after discharging, will be useful to the experimenter. Studies using a range of incident electron energies to deposit a charge layer at different depths can explore the penetration of the UV light and resulting effectiveness of discharge. Various *ex situ* UV sources, (*e.g.*, deuterium discharge lamp, Xe flash lamp and solar simulator source) and the use of a UHV fiber optic feedthrough to channel light directly to a collimating lens mounted to the HGRFA can determine the most effective UV source to neutralize negative charging for various materials and circumstances.

An effective method of calibrating the HGRFA for measuring the absolute total electron yield for conducting samples has been to measure the balance of incident charge to exiting charge at the crossover energies when the total yield is unity. In practice, the incident beam current is set equal to the absolute yield times the sum of the grid, stage, and collector currents at an energy where the sample current goes to zero. This procedure does not work for insulating samples, as it does not account for the charge accumulating within the insulator and the subsequently reduced sample current. By monitoring the charge accumulation with periodic surface voltage measurements, in addition to the grid, stage, collector, and sample currents, a corresponding balance for insulating samples can be determined and absolute yield calibration performed for insulators.

5.2.2. Future Applications

The SVP instrumentation developed for this thesis has been shown to have many potential applications as a result of its enhanced sensitivity and range, and its incorporation in the existing USU MPG electron emission test chamber. There are many tests presently under consideration to investigate a variety of materials and physical processes with the SVP. These tests are intended to both push the limits of the SVP and to extend our knowledge of the physics of the materials. These proposed experiments will investigate phenomena seen in our previous experiments, as well as investigate new theoretical ideas. The abbreviated set of experiments described below is intended not to set a limit to the probe's capabilities, but rather to demonstrate the versatility of the SVP.

The proposed charge accumulation and dissipation experiments are presented in two groups. The first group uses the SVP by itself. The second group uses the SVP in concert with the HGRFA. For both groups of experiments, it will be of great interest to do many different tests.

A range of materials, including the prototypical materials LDPE, Kapton HN™, and Al₂O₃, which have been previously tested by the USU MPG, should be included in testing. A

critical aspect is to understand the effects of different distributions of the energy-dependant densities of available trap states below the conduction-band mobility edge (*e.g.*, single level, linear, and exponential DOS) as discussed by Sim (2012). Measurements for materials with a wide range of conductivities will also provide very useful information. Furthermore, many materials with important applications in spacecraft charging remain untested.

A range of incident electron beam energies, currents, and pulse sequence configurations are needed to characterize material behavior. To first order, the beam energy determines the depth of the deposited charge layer within the material, the beam current determines the extent of radiation-induced conductivity active in the material layer between the incident surfaces and the deposited charge layer, and the pulse sequence determines the time available for charge dissipation before the next pulse. Lower-energy experiments deposit charge very near the surface and can often be viewed as time-of-flight experiments. Intermediate-energy experiments deposit charge layers within the material, which can subsequently dissipate through conduction to both top and bottom surfaces (Roth *et al.*, 2009). Higher-energy experiments are penetrating experiments in which no appreciable charge is deposited within the insulator, but deposited energy can initiate radiation-induced conductivity.

Surface voltage studies conducted as functions of other environmental characteristics, such as temperature, applied electric field, electron flux density, electron fluence, and experiment duration, can be adjusted using the present capabilities of the electron emission test chamber. All these variables have been shown to affect the charge transport (Sim, 2012) and electron emission (Hoffmann, 2010) properties of materials and hence, charge accumulation and dissipation.

5.2.2.1. Proposed Experiments with the Surface Voltage Probe

Measurement of charge accumulation and dissipation, like those described in Chapter 4, can be conducted with the myriad of variations outlined in the section above.

Of particular interest are studies of somewhat higher-conductivity materials in the range of $10^{-14} \text{ } (\Omega\text{-cm})^{-1}$ to $10^{-17} \text{ } (\Omega\text{-cm})^{-1}$, which have dissipation time constants in the range of experimentally accessible times (10 s to a few days). These materials have been shown to be significantly affected by repeated dosing and radiation damage caused by higher-energy beams (Hoffmann, 2010). In such cases, both the charge accumulation and dissipation curves as functions of time will be modified by charge leaving the sample during charge deposition times. One such proposed study investigates the increased conductivity in polymeric materials that result from increased trap site density from moderate radiation exposure at the Idaho State University accelerator facility. The equilibrium voltage determined by charge accumulation measurement is a direct measure of the total density of available trap states. This equilibrium voltage varies with radiation fluence and concomitant trap site creation.

Another subject of interest is how repeated measurements affect the yield results. Hoffmann (2010) has shown repeated charging and discharging of a material has a large effect on the yield of the material, especially when residual charge accumulates in the sample. This is particularly evident in measuring yield decay curves of highly insulating materials such as Kapton HNTM and Al₂O₃. As a material is charged to higher positive values, more emitted electrons should be reattracted to the surface, this causes the yield to asymptotically approach unity, where incident charge currents are exactly balanced by the reduced emitted current (Chang *et al.*, 2000). Recent experiments have shown after several successive yield decay curves have been made, where a sample is charged to equilibrium and then discharged by electron and UV flooding, the yield no longer asymptotically approaches a value of one; rather, it has a value of $\sigma=1.08$ (FIG. 5.2). To explain this behavior, it has been suggested after a full day of measurements, there remains some accumulated deep space charge that cannot be adequately dissipated with the discharge methods currently employed. This imbedded charge acts to repel additional incident current, thereby increasing the equilibrium yield. Repeating these

measurements (Hoffmann, 2010) while simultaneously employing the SVP will help in determining exactly what this deep-space charge is and will give the experimenter insight into the nature and behavior of this offset.

Efforts can be made to expand the use of the SVP as a key element of the charge storage method for conductivity measurements. This will require improvement in response time for applications of higher conductivity materials. It will also require improved instrument stability to allow measurements of lower conductivity materials.

A particularly useful class of measurements to investigate conduction mechanisms is the time-of-flight experiments as presented by Sim (2012). The time of flight experiments are made by depositing electrons on the surface of an insulating material using low-incident energy beams. Monitoring the current and the decay of surface voltage will give detailed information of the transport processes of the material. This helps characterize surface potential as a function of time, electric field, temperature and charge flux in dispersive systems.

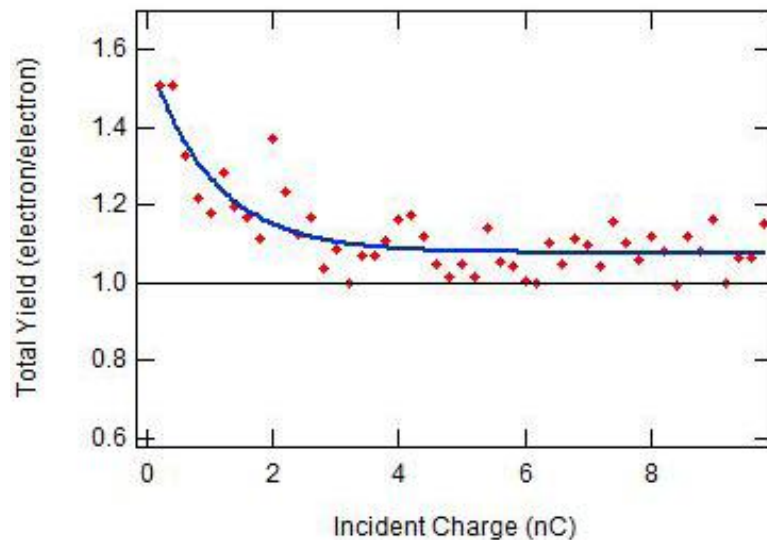


FIG. 5.2. Decay curve of Kapton HN™ shows the total yield does not approach unity. Repeating these measurements done by Hoffmann (2010) with simultaneous SVP measurements will give the experimenter insight into the nature of this offset.

One set of proposed time of flight experiments will investigate the transition from diffusive to dispersive transport over long timescales in highly disordered polymeric materials (Hart *et al.*, 2007). There have been several studies (Scher and Montroll, 1975; Hart *et al.*, 2007) on the relationship between the two distinct power laws in models of time evolution of conductivity (Zallen and Scher, 1971). Repeating studies on Hytrel done by Hart, for immediate comparison, will allow for a better understanding of follow-up measurements on Kapton HN, where it is believed dispersive transport occurs.

5.2.2.2. Proposed Experiments with the SVP and HGRFA

The capacity to simultaneously measure the surface voltage with the SVP and incident and emitted currents with the HGRFA makes it possible to do many new experiments. The indirect methods of inferring surface voltages employed in many prior studies can now be confirmed directly. A material's electron emission spectra and electron yield (defined as the ratio of electron flux out of a material to the electron flux into the material) determines how quickly net charge accumulates in a spacecraft component in response to incident electron, ion, and photon fluxes. The initial configuration of the spacecraft charging chamber did not allow for direct measurement of the adopted potential.

The first proposed experiments repeat measurements of the electron-induced total, secondary and backscattered yields of highly insulating materials made by the USU MPG (Hoffmann *et al.*, 2008; Hoffmann *et al.*, 2009a; Hoffmann, 2010). The main focus of graduate student works by Hoffmann and Thomson were on how charging influences the incident and emitted fluxes of a material (Thomson, 2004; Hoffmann, 2010). These measurements showed significant deviations in the yields as a function of incident energy that have been attributed to the effects of accumulated charge and accompanying surface voltage. These studies were forced to approximate the surface voltage through indirect means. Hoffmann and Dennison (Hoffmann and Dennison, 2010) have proposed a detailed set of explanations to explain these anomalies in six

different zones above and below the first and second crossover energies. In almost every case, the verisimilitude of the proposed explanations can be unequivocally confirmed by repeated direct measurement of the surface voltages acquired during measurements of these yield curves with the pulsed-beam system.

A related set of measurements, which is similarly affected by charge accumulation in insulators, are yield-decay curves. These curves are acquired by pulsing the sample with a short 5 μ s pulse without dissipation and, as the charge builds up in a material, the yield of the material changes. Thomson (Thomson *et al.*, 2003; Thomson, 2004) and Hoffmann (Hoffmann *et al.*, 2009b; Hoffmann, 2010) have proposed a model for the change in yields as a function of charge accumulation, which has been found to adequately describe the yield decay curves. An intermediate prediction of the model is the charge accumulation of surface voltage as a function of incident electron flux. Intermittent measurements of the surface voltage during yield decay curve measurements will be a stringent confirmation of this model by directly measuring the predicted surface voltages.

The yield decay model used to fit such yield measurements at a given incident energy can be extrapolated back to the intrinsic yield, the yield for a material with no accumulated charge from the incident pulsed beam. Figure 4.1 is formed from 21 yield-decay curves taken at different incident energies, where each point on the curve represents the extrapolated yield at zero incident charge using these models. A fit to these points (green curve in FIG. 4.1) provides an estimate of the intrinsic yield curve of an insulator, which is the yield as a function of incident energy for a material with no accumulated charge. Obviously, direct measurements of the surface voltage during acquisition of the component yield-decay curves will lend much credence to the idea of an intrinsic yield curve.

It may be possible to greatly reduce the laborious efforts currently required to determine such an intrinsic yield curve by judicious measurements of both full yield-decay curves and

surface voltages. Hoffmann (2010) proposes a significant portion of the data collection currently required could be eliminated if the surface potentials were known. It has been shown the shape of the yield-decay curve does not vary appreciably with incident energy, but that only the amplitude of the curve changes. Taking a few representative yield-decay curves will determine the generalized shape of the curve for a given material. Simply acquiring one or two surface voltage points with associated yields at many different incident energies will then provide information regarding the magnitude of the generalized yield-decay curves at each incident energy. This will eliminate the need to take full yield-decay curves at many incident energies, but will still allow determination of a detailed composite intrinsic yield curve. Refer to Hoffmann (2010) for an in-depth discussion of the measurements made to obtain a composite yield curve; this will provide the necessary background information to show how the SVP will help improve the yield measurements.

The above experiments are merely the tip of the iceberg of possible experiments that can be envisioned using the SVP apparatus. There is little doubt the information acquired from these results will lead to a greater understanding of electron emission, charge mobility processes, and spacecraft charging applications.

REFERENCES

- Aragoneses, A., M. Mudarra, J. Belana, and J. A. Diego, 2008, "Study of dispersive mobility in polyimide by surface voltage decay measurements," *Polymer* **49**, 2440.
- Arnfield, D., and J. R. Dennison, 2008, "Temperature dependence of Kapton HN breakdown voltages," in *Utah State University Student Showcase*, Logan, UT.
- Attocube Systems, 2008, *Anr50 User Manual*, Attocube Systems, München Germany.
- Bethe, H., and W. Heitler, 1934, "On the stopping of fast particles and on the creation of positive electrons," *Proceedings of the Royal Society of London. Series A, Containing Papers of a Mathematical and Physical Character* **146**, 83.
- Brunson, J., 2010, "Hopping conductivity and charge transport in low density polyethylene," Ph.D. dissertation (Utah State University).
- Cazaux, J., 1999, "Some considerations on the secondary electron emission, Δ from E irradiated insulators," *J. Appl. Phys.* **85**, 1137.
- Cazaux, J., 2003, "Scenario for time evolution of insulator charging under various focused electron irradiations," *J. Appl. Phys.* **95**, 731.
- Chang, W. Y., J. R. Dennison, N. Nickles, and R. E. Davies, 1998, "Utah State University ground-based test facility for study of electronic properties of spacecraft materials," in *6th Spacecraft Charging Technology Conference*, Air Force Research Laboratory Science Center, Hanscom Air Force Base, MA.
- Chang, W. Y., J. R. Dennison, J. Kite, and R. E. Davies, 2000, "Effects of evolving surface contamination on spacecraft charging," in *38th American Institute of Aeronautics and Astronautics Meeting on Aerospace Sciences*, Reno, NV.
- Coelho, R., L. Levy, and D. Sarraïl, 1989, "Charge decay measurements and injection in Insulators," *J. Phys. D*: **22**, 1406.
- Corbridge, J., J. Dennison, and A. Hunt., 2008, "Radiation induced conductivity measurements of insulating materials at low temperatures," in *CAARI 2008: 21st International Conference on the Application of Accelerators in Research and Industry*, Fort Worth, TX.
- Cornet, N., D. Goeuriot, C. Guerret-Piecourt, D. Juve, D. Treheux, M. Touzin, and H.J. Fitting, 2008, "Electron beam charging of insulators with surface layer and leakage currents," *J. Appl. Phys.* **103**, 13.
- Davies, R., 1996, "An instrument for experimental secondary and backscattered electron investigations with applications to space craft charging," M.S. thesis (Utah State University).

Dennison, J. R., 2004, "Electron emission from insulating materials," in *Instituto de Ciencia de Materiales de Madrid in the Departmento de Fisica e Ingenieria de Superficies at the University of Madrid*, University of Madrid, Madrid, Spain.

Dennison, J. R., 2007, "Charging and discharging of highly resistive spacecraft materials," in *Physics Colloquium*, Idaho State University, Pocatello, ID.

Dennison, J. R., and A. R. Fredrickson, 2002, "Proposal for measurements of charge storage decay time and resistivity of spacecraft insulators," in *NASA Space Environments and Effects Kickoff Meeting*, San Diego, CA.

Dennison, J. R., A. R. Fredrickson, and P. Swaminathan, 2003a, "Charge storage, conductivity and charge profiles of insulators as related to spacecraft charging," in *Proceedings of the 8th Spacecraft Charging Technology Conference*, NASA Marshall Space Flight Center, Huntsville, AL.

Dennison, J. R., R. Hoffmann, and J. Abbott, 2006, "Measurement of the electron yields of highly insulating materials," in *CAARI 2006: 19th International Conference on the Application of Accelerators in Research and Industry*, Fort Worth, TX.

Dennison, J. R., J. Kite, C. D. Thomson, J. Corbridge, R. Berry, and C. Ellsworth, edited by NASA (Published by NASA electronically at <http://see.msfc.nasa.gov/scck/>, 2003b), p. 250.

Dennison, J. R., A. Sim, J. Brunson, S. Hart, J. Gillespie, J. Dekany, C. Sim, and D. Arnfield, 2009, "Engineering tool for temperature, electric field and dose rate dependence of high resistivity spacecraft materials," in *Proceedings of the 47th American Institute of Aeronautics and Astronautics Meeting on Aerospace Sciences*, Orlando, FL.

Dennison J. R., P. Swaminathan, R. Jost, J. Brunson, N. Green, and A.R. Fredrickson, 2005, "Proposed modifications to engineering design guidelines related to resistivity measurements and spacecraft charging," in *Proceedings of the 9th Spacecraft Charging Technology Conference*, Epochal Tsukuba, Japan.

Dennison, J. R., C. Thomson, J. Kite, V. Zavyalov, and J. Corbridge, 2004, "Materials characterization at USU: facilities and knowledge base of electronic properties applicable to spacecraft materials," in *Proc. 8th Spacecraft Charging Tech. Conf.*, Huntsville, AL.

Dupont, 2010, "Technical data sheet," http://www2.dupont.com/Kapton/en_US/assets/downloads/pdf/HN_datasheet.pdf.

Fowler, J., 1956, "X-Ray induced conductivity in insulating materials," *Proceedings of the Royal Society of London. Series A, Mathematical and Physical Sciences* (1934-1990) **236**, 464.

Fredrickson, A. R., 1979, "Electric fields in irradiated dielectrics," *Spacecraft Charging Technology NASA CP-207*, 554.

Fredrickson, A. R., C. Benson, and J. Bockman, 2003, "Measurement of charge storage and leakage in polyimides," *Nucl. Instrum. Methods in Phys. Res., B* **208**, 454.

Fredrickson, A. R., A. Whittlesey, and H. Garrett, 2001, "Comparing CRRES internal discharge monitor results with ground tests and published guidelines," in *7th Spacecraft Charging Technology Conference*, Noordwijk, Netherlands.

Gillespie, J., 2012, "Measurements of the temperature dependence of radiation induced conductivity in polymeric dielectrics," (Utah State University), unpublished.

Goodfellow Cambridge Ltd., 2006, Goodfellow Cambridge Ltd., Devon.

Gross, B., J. Dow, and S. Nablo, 2003, "Charge buildup in electron-irradiated dielectrics," *J. Appl. Phys.* **44**, 2459.

Hart, S. R., J. Brunson, and J. R. Dennison, 2007, "Electric-field-induced hopping conductivity in polymers," in *American Physical Society March Meeting*, Denver, CO.

Hastings, D., and H. Garrett, 1996, *Spacecraft-environment interactions* (Cambridge Press, New York).

Hoffmann, R., 2010, "Electron-induced electron yields of uncharged insulating materials," M.S. thesis (Utah State University).

Hoffmann, R., and J. Dennison, 2010, "Measurement methods of electron emission over a full range of sample charging," in *11th Spacecraft Charging Technology Conference*, Albuquerque, NM.

Hoffmann, R., J. R. Dennison, and J. Albretsen, 2009a, "Flux and fluence dependence of electron emission for high-yield, high-resistivity materials: implications for spacecraft charging," in *Proceedings of the 47th American Institute of Aeronautics and Astronautics Meeting on Aerospace Sciences*.

Hoffmann, R., J. Dennison, C. Thomson, and J. Albretsen, 2008, "Low-fluence electron yields of highly insulating materials," *IEEE Trans. on Plasma Sci.* **36**, 2238.

Hoffmann, R., J. L. Hodges, J. Hayes, and J. Dennison, 2009b, "Measurement of Charging and Discharging of High Resistivity Materials Spacecraft Materials by Electron Beams," in *47th American Institute of Aeronautics and Astronautics Meeting on Aerospace Sciences*, Orlando, FL.

Kite, J., K. Ford, and J. R. Dennison, 2000, "A high resolution faraday cup charged particle spectrometer," in *American Physical Society Four Corner Sectional Meeting*, Fort Collins, CO.

Leach, R., and M. Alexander, 1995, "Failures and anomalies attributed to spacecraft charging," NASA STI/Recon Technical Report N **96**, 11547.

Lide, D., 1993, *CRC Handbook of Chemistry and Physics* (CRC Press, Boca Raton, FL).

Liufu, D., X. S. Wang, D. M. Tu, and K. C. Kao, 1998, "High-field induced electrical aging in polypropylene films," *J. Phys. D* **83**, 2209.

- Matskevich, T. L., 1959, "Secondary electron emission of some polymers," *Fizika tverdogo Tela* **1**, 276.
- Melchinger, A., and S. Hofmann, 1995, "Dynamic double layer model: description of time dependent charging phenomena in insulators under electron beam irradiation," *J. Appl. Phys.* **78**, 6224.
- Meyza, X., D. Goeuriot, C. Guerret-Piecourt, D. Treheux, and H. Fitting, 2003, "Secondary electron emission and self-consistent charge transport and storage in bulk insulators: application to alumina," *J. Appl. Phys.* **94**, 5384.
- Monroe, D., 1987, "Band-edge conduction in amorphous semiconductors," *Disordered Semiconductors*, 705.
- Monroe Inc., 1994, *Instruction manual isoprobe electrostatic millivoltmeter model 162 S/N detector/preamplifier probe model 1015* (Monroe Electronics Inc., New York).
- Montanari, G., G. Mazzanti, F. Palmieri, A. Motori, G. Perego, and S. Serra, 2001, "Space-charge trapping and conduction in LDPE, HDPE and XLPE," *J. Phys. D* **34**, 2902.
- Nickles, N., 2002, "The role of bandgap in the secondary electron emission of small bandgap semiconductors: studies of graphitic carbon," PhD dissertation (Utah State University).
- Nickles, N., W.-Y. Chang, and J. R. Dennison, 2001, "Hemispherical grid retarding field analyzer for absolute measurement of secondary and back-scattered electron yields," in *American Physical Society March Meeting 2001*, Seattle, WA.
- Pawar, S. D., P. Murugavel, and D. M. Lal, 2009, "Effect of relative humidity and sea level pressure on electrical conductivity of air over the Indian Ocean," *J. Geophys. Res.* **114**, 8.
- Peacock, A., 2000, *Handbook of Polyethylene: Structures, Properties, and Applications* CRC Press.
- Rose, A., 1951, "An outline of some photoconductive processes," *RCA Review* **12**, 362.
- Roth, J., 2009, "Electrostatic discharge in spacecraft materials," Undergraduate Honors thesis, (Utah State University).
- Roth, J. A., R. Hoffmann, and J. R. Dennison, 2009, "Effects of radiation induced conductivity on electrostatic discharge in insulating materials," in *1st AIAA Atmospheric and Space Environments Conference*, San Antonio, TX.
- Scher, H., and E. Montroll, 1975, "Anomalous transit-time dispersion in amorphous solids," *Phys. Rev. B* **12**, 2455.
- Sessler, G., M. Figueiredo, and G. Ferreira, 2004, "Models of charge transport in electron-beam irradiated insulators," *IEEE Trans. Dielectrics and Electrical Insulation* **11**, 192.

Sim, A., 2012, "A unified theory of charge dynamics in highly insulating materials," (Utah State University), unpublished.

Sim, A., and J. Dennison, 2010, "Parameterization of temperature, electric field, dose rate and time dependence of low conductivity spacecraft materials using a unified electron transport model," in *11th Spacecraft Charging Technology Conference*, Albuquerque New Mexico.

Sim, C., A. Sim, D. Ball, and J. R. Dennison, 2010, "Temperature and endurance time dependance of electrostatic field strengths of polymer spacecraft insulators," in *11th Spacecraft Charging Technology Conference*, Albuquerque, NM.

Song, Z., C. Ong, and H. Gong, 1997, "Secondary and backscattered electron yields of polymer surface under electron beam irradiation," *Appl. Surf. Sci.* **119**, 169.

Swaminathan, P., 2004, "Measurement of charge storage decay time and resistivity of spacecraft insulators," M.S. thesis (Utah State University).

Thomas, A., J. R. Dennison, S. Hart, and R. Hoffmann, 2006, "The effect of voltage ramp rate on dielectric breakdown of thin film polymers," in *American Physical Society Four Corner Section Meeting*, Utah State University, Logan, UT.

Thomson, C., 2001, "Experimental investigation of snapover: The sudden increase of plasma current drawn to a positive biased conductor when surrounded by a dielectric," M.S. thesis (Utah State University).

Thomson, C., 2004, "Measurements of the secondary electron emission properties of insulators," Ph.D. dissertation (Utah State University).

Thomson, C. D., V. Zavyalov, and J. R. Dennison, 2003, "Instrumentation for studies of electron emission and charging from insulators," in *Proceedings of the 8th Spacecraft Charging Technology Conference*, NASA Marshall Space Flight Center, Huntsville, AL.

Toomer, R., and T. J. Lewis, 1980, "Charge trapping in corona-charge polyethylene films," *J. Phys. D* **13**, 1343.

Trek Inc., 2000, "Operator's manual model 341a high-voltage electrostatic voltmeter."

Walden, R. H., 1972, "A method for the determination of high-field conduction laws in insulating films in the presence of charge trapping," *J. Appl. Phys.* **43**, 1178.

Weingart, R. C., R. H. Barlett, R. S. Lee, and W. Hofer, 1972, "X-ray-induced photoconductivity in dielectric films," *IEEE Trans. Nucl. Sci.* **19**, 15.

Willis, R., and D. Skinner, 1973, "Secondary electron emission yield behavior of polymers," *Solid State Commun.* **13**, 685.

Wilson, G., and J. Dennison, 2010, "Approximation of range in materials as a function of incident electron energy," in *11th Spacecraft Charging and Technology Conference*, Albuquerque, NM.

Wintle, H., 1977, "Photoelectric effects in insulating polymers and their relation to conduction processes," IEEE Trans. Electrical Insulation **12**, 97.

Wintle, H., 1983, *Conduction processes in polymers* Vol. IIA, (American Society for Testing and Materials, Baltimore, MD).

Wintle, H., 1999, "Analysis of the scanning electron microscope mirror method for studying space charge in insulators," J. Appl. Phys. **86**, 5961.

Yasuda, M., T. Nobuo, and H. Kawata, 2004, "A monte carlo calculation of secondary electron emission from organic compounds," Jpn. J. Appl. Phys. **43**, 4004.

Zallen, R., and H. Scher, 1971, "Percolation on a continuum and the localization-delocalization transition in amorphous semiconductors," Phys. Rev. B **4**, 4471.